THE UNIVERSITY OF CHICAGO

A SEARCH FOR MAGNETIC MONOPOLES USING SUPERCONDUCTING INDUCTION DETECTORS

A DISSERTATION SUBMITTED TO
THE FACULTY OF THE DIVISION OF THE PHYSICAL SCIENCES
IN CANDIDACY FOR THE DEGREE OF
DOCTOR OF PHILOSOPHY

DEPARTMENT OF PHYSICS

BY

JOSEPH R. INCANDELA

CHICAGO, ILLINOIS

AUGUST, 1986

ACKNOWLEDGEMENTS

The research that is reported in this thesis is the result of the combined efforts of many people who it is my pleasure to acknowledge. I thank my collaborators: M. Campbell, H. Frisch, M. Kuchnir, H.R. Gustafson, and S. Somalwar. I especially thank Henry Frisch, my thesis sponsor, for his guidance, support, generosity, and a vast number of valuable insights into the art of experimental physics. I also especially thank Sunil Somalwar for being ever willing to contribute his time and ideas and for many conversations which helped me to formulate many of my own ideas. I thank J. Matthews, P. McGoff, A. Green, and E. Weatherhead, who even as undergraduates were extremely dedicated and played an important role in our work. I also thank Lee Brekke for many insightful conversations about theoretical physics and mathematics. I thank the members of my thesis committee; H. Frisch, R. Geroch, Y. Nambu and R. Winston.

I thank R. Northrop, R. Gabriel, L. Fiscelli, and S. Lucero of the EFI engineering services group; the members of the EFI central shop; R. Smith, H. Jostlein, A. Guthke, C. Kendzione, J. Tague and the crew of lab 2, of Fermilab. I also thank Kathy Visak for patiently typing this thesis.

I dedicate this thesis to my family, (specialmente miei nipoti - Zac, Gabe, Alex, and Chloe), and to my friends, (especially Sara).

TABLE OF CONTENTS

ACKNOWLEDGEMENTS ii

LIST OF TABLES v

LIST OF FIGURES vi

ABSTRACT ix

FORWARD 1

Chapter

I. MAGNETIC MONOPOLES 3

Dirac's Theory
Monopoles Without Strings
Searches for the Dirac Monopole
Monopoles in Grand Unified Theories:
The 't Hooft-Polyakov Model
Monopoles in the Early Universe
Astrophysical Bounds on the Monopole
Flux in the Galaxy

II. THE EXPERIMENTAL TECHNIQUE 24

Introduction
The Evolution of the Induction Technique
Considerations for Large Area Detectors
Calculation of the Field in the Shield
After the Passage of a Monopole
Determination of the Response Function
Response Functions Calculated for CFM I
Calibrating the Detector

III. AN EXPERIMENT TO MEASURE THE MONOPOLE FLUX 74

An Overview of the Apparatus
Gradiometers and Superconducting Shields
Impedance Matching Transformers and SQUIDs
Pseudopoles
Cryogenic System
Fe Shield
Isolation from Vibration and Other Noise
Sources
Environmental Disturbance Monitors
The Performance of the Detector
Cryogenic Performance
Signal and Calibration
Response to Controlled Disturbances

IV. DATA, ANALYSIS, AND RESULTS 121

Run 1: August 29-October 4, 1983
Run 2: January 10-July 17, 1984
Results and Conclusions

V. A SECOND GENERATION DETECTOR 157

Detector Design
Shields
Gradiometers
Close-Packed Orthogonal Gradiometers
Series-Parallel and Distributed-Parallel Gradiometers

Description of the Apparatus
Overview
Gradiometers and Superconducting Shields
Pseudopoles
SQUIDs
Detector Cooling
Vibration Isolation and Environmental Disturbance Monitors
Reduction of Ambient Magnetic Fields
Data Acquisition

Test Runs and Detector Performance
Decoupling of Overlapped Gradiometers and Detector Signal Size
Sensitivity to Environmental Disturbances

Results and Conclusions

EPILOGUE 206

Appendix

A. DETERMINATION OF THE RESPONSE FUNCTIONS 210

B. OPERATION OF RF-BIASED SQUIDS AND STRAIN GAUGE SIGNAL PROCESSING 220

C. MUTUALLY ORTHOGONAL GRADIOMETERS 235

REFERENCES 258

LIST OF TABLES

1. Particle Spectrum and Particle Properties in the Georgi-Glashow Model 12

2. Measured Constants of the Superconducting Transformers . . . 87

3. Ambient Magnetic Fields During Cooldown of CFM I 99

4. Temperatures in Experiment CFM I 109

5. Comparison of Calculated and Measured Pseudopole Signals 111

6. Comparison of Sensitivity to the Ambient Magnetic Field Before and After Repair of Shield for Top Circuit . . . 134

7. Dead Time Study Results 142

8. Data Record for Event 39: A 12.7 mV Offset 143

9. Number of Events Correlating with Various Monitors 146

10. Four Events with a Single Weak Monitor Signal 151

11. Monopole Flux Limits from Induction Detectors 155

12. Comparison of Observed with Predicted Signals for Series and Series-Parallel Gradiometers 181

13. Classification of Four Orthogonal Patterns with Even/Odd (+/-), Character for All Transformations in C_{4v} 241

14. Subgroups of C_{4v}, Their Generators, and the Number of Patterns Associated with Each 249

15. Even/Odd, (+/-), Classification of 6 Mutually Orthogonal Patterns in C_{4v} Under Transformations in C_{4v} 252

16. Classification Scheme for Mutually Orthogonal Gradiometers with n-Fold Symmetric Shapes 255

LIST OF FIGURES

1. Prototype Detector Operated at Fermilab 32

2. D.C. Signal Offsets Observed in the Fermilab Prototype in 48 Days of Operation 36

3. Event Observed Labor Day, 1982 38

4. Fraction F of Signal for Various Loop and Shield Sizes . . . 42

5. Shield Geometry and Monopole Trajectory Used in the Calculation of the Trapped Field 46

6. Dipole Field Trapped in Shield After the Passage of a Monopole 48

7. Shape of Normal Region Used in the Calculation of the Field Trapped in the Shield 50

8. True and Simplified Geometries for Field Calculations . . . 60

9. Intended and Actual Gradiometer Patterns 62

10. The Response Function for the Gradiometer Used in CFM I . . 66

11. The Response Function for the Gradiometer Intended for CFM I 68

12. Pseudopole Penetrating Shield 70

13. Apparatus Used to Test the Calibration Technique and the Field Calculation 72

14. The CFM I Apparatus 76

15. Gradiometer and Support Plane 80

16. Inductance Versus Filament Length of Gradiometers with Twelve Square Cells Along a Diameter 84

17. Detector Circuit with Transformer Coupling 86

18. Resistance Versus Temperature for a Copper Thermometer . . . 94

19. Resistance of a Nominal 100Ω, 1/8 W Carbon Resistor Versus Temperature 96

20. Ground Configurations 104

21. Liquid Nitrogen Cooldown Plot for CFM I 106

22. Liquid Helium Cooldown Plot for CFM I 108

23. Vibration Sensitivity Test Data for CFM I 114

24. Data Sample from Run 2 of CFM I 116

25. Data from Test of Sensitivity to RF Radiation 118

26. Pseudopole Signals and Data Sample from Run 1 124

27. Magnetic Field Sensitivity Test Data for CFM I 126

28. D.C. Offsets from Runs 1 and 2 and Detector Response Function for CFM I 132

29. Timing Histogram for Magnetometer Signals Relative to Top Gradiometer Signal Offsets in CFM I 138

30. Timing Histogram for Bottom Gradiometer Signals Relative to Top Gradiometer Signal Offsets in CFM I 140

31. D.C. Offsets Prior to Monitor Signal Cuts in CFM I 148

32. D.C. Offsets After all Cuts in CFM I 150

33. Plot of Z Component of the Trapped Field 162

34. Cell Width Versus Radial Position for $\gtrsim$ 90% Decoupling From Shield 164

35. The 1.1 Meter Diameter Concentric Loop Gradiometer 166

36. The Response Function for CFM II 168

37. Overlapping of Simple Rectangular Grids 170

38. Series-Parallel Circuit 174

39. Equivalent Series-Parallel Circuit Diagram for the Calculation of the SQUID Current After Passage of a Monopole Through the jth Subsection 176

40. Plot of SQUID Current Versus Inductance of Optimized Series-Parallel Gradiometers 178

41. Effective Inductance of Optimized Series-Parallel Gradiometers 180

42. Standard Gradiometer Obtained from a Simple Loop by Twists 184

43. Distributed-Parallel Gradiometer Formation 186

44. CFM II Apparatus 188

45. Vibration Sensitivity Test Data for CFM II 196

46. Gradiometer Coupling Data for CFM II 200

47. D.C. Offsets in the Two Overlapped Gradiometers After All Cuts 204

48. Hypothetical Large Area Detector 208

49. Graphic Representation of Geometric Quantities Used in the Calculation of the Position of the Vortex Currents 216

50. Strain Gauge Signal Processing Circuit 234

51. Effect of a 180° Rotation on Two Rectangular Gradiometer Patterns 238

52. Reflection Axes for 4-Fold Symmetry 244

53. Rotation of Reflection Axes 248

54. Six Mutually Orthogonal Patterns with Symmetries of of the Group C_{4v} 254

ABSTRACT

The flux of cosmic ray magnetic monopoles at the earth's surface is measured using a superconducting induction detector. The detector employs gradiometer twisted loop configurations within completely closed superconducting shields to obtain a large sensitive area and stable operation in ~1-10 mGauss ambient magnetic fields. The detector is isolated from the environment to inhibit the production of spurious signals and the environment is monitored in order to veto such signals. The total sensitive area for a monopole passing through either or both of the gradiometers is 2100 cm^2. In two exposure periods, (19 days with only 1400 cm^2 sensitive area and 136 days with 2100 cm^2), there were no monopole candidates observed. A monopole flux limit of $f_m \lesssim 6.7 \times 10^{-12}$ cm^{-2} sr^{-1} sec^{-1} at 90% Confidence Level is therefore established.

The design and performance of a second generation detector with 1.1 meter diameter gradiometers is also presented. The detector demonstrates that gradiometers can be overlapped without inductive coupling to obtain high redundancy without increasing shield volume. The detector was operated in ambient magnetic fields of ~5-125 mGauss. The rate of occurrence of two-fold coincident monopole-sized d.c. offsets is measured to be less than 1 per 500 years. Implications for 100 m^2 to 1000 m^2 induction detectors are discussed.

FORWARD

Over a period of 55 years the monopole concept has proved itself to be extremely buoyant. Monopoles continue to be deeply related to such fundamental issues as the quantization of electric charge and the origin of the universe. There non-observation has thus played an important role in cosmology and -- together with the non-observation of proton decay -- has left open the question of grand unification. In many ways then, the discovery of magnetic monopoles would help begin to resolve some of the deepest concerns of physics. It is for such reasons that monopoles have been and will continue to be sought.

In 1981 we began to consider a monopole search using ionization-type detectors. After the announcement of the Stanford monopole candidate in the early part of 1982 however, we decided that the induction technique was superior. We then set out to accomplish two things. First we sought to measure the cosmic ray magnetic monopole flux with an induction detector having substantially larger area than the Stanford apparatus. Our second goal was to develop more robust and inexpensive induction detectors so that detectors with very large sensitive areas could be built in the future. A detector capable of a flux measurement at the Parker bound would require a surface area of 1000 m^2.

In chapter I of this thesis I present the theoretical motivation for expecting that monopoles exist. The puzzling extreme abundances, (too many or too few) predicted for various cosmological theories are discussed as well as astrophysical bounds on the monopole

flux such as that of Parker mentioned above. In chapter II the ways in which one looks for monopoles are briefly discussed with special attention being given to the induction technique. Our contribution to the improvement and simplification of the technique is discussed and calculations pertinent to our application of the technique are also presented. In chapters III and IV an experiment to measure the monopole flux, (our first goal mentioned above) is detailed. In chapter V a robust, improved, large area detector is described. This latter detector represents an important step toward realizing the construction of a very large area detector, (our second goal). The implications of our flux measurement and detector development are summarized in the epilogue which follows chapter V.

Appendix A describes the numerical calculation of the detector response functions. Appendix B discusses the principle of operation of the SQUIDs and the strain gauge signal processing electronics. Appendix C discusses the role of symmetry considerations in determining overlapped gradiometers and classifies orthogonal patterns for certain classes of gradiometer shapes.

CHAPTER I

MAGNETIC MONOPOLES

Dirac's Theory

In 1931 Dirac[1] carefully reconsidered the connection between the non-integrable derivatives of the phase of a wave function and the potentials of the electromagnetic fields. He found that the indeterminacy of phase up to an integral multiple of 2π leads to a new physical phenomenon: an isolated magnetic monopole.

Dirac began by reviewing the argument in which the non-integrable derivatives, k^{ν}, of the phase of the wave function of a particle are related to the potentials, A^{ν}, of the electromagnetic field as:

$$A^{\nu} = \frac{\hbar c}{e} \; k^{\nu}$$

He then proceeded to point out that this argument does not take into account one further fact -- namely that a phase is always undetermined up to an integral multiple of 2π. One must therefore reconsider the connection between the k's and the potentials. In particular, the change in phase around a closed curve may be different for different wave functions by arbitrary multiples of 2π. It is then not sufficiently definite to be interpreted directly in terms of the electromagnetic field.

To examine this question Dirac first considered a very small closed curve and observed that the wave equation requires the wave function to be continuous so that the change in phase around the curve must be small compared with 2π. The change in phase cannot be different by multiples of 2π for different wave functions in this case and must therefore have a definite value which may indeed be interpreted as the flux of magnetic field through the curve. There is however an exceptional case which has not been considered -- the case in which the wave function vanishes. In that case the phase has no meaning.

The wave function of a particle, (e.g. an electron) is complex and so will in general vanish along a line. Dirac called this line a "nodal line." For a wave function having a nodal line passing through the small closed curve we can no longer use considerations of continuity to require that the change in phase be small. We may only say that it will be close to $2\pi n$ where n is an integer. The integer will be characteristic of the nodal line and its sign will be associated with a direction in which the line is encircled or, equivalently, with a direction along the line.[2]

In order not to introduce ambiguities into the applications of quantum theory, the difference between the change in phase around the small closed curve and the nearest $2\pi n$ must be the same as the change in phase for the case of a wave function with no nodal line through the curve. Therefore, it is this difference that is associated with the magnetic flux through the closed curve. The change in phase is thus:

$$\Delta\phi = 2\pi n + (e/\hbar c) \int_{\Delta S} \vec{B} \cdot d\vec{S} \qquad (1.1)$$

where ΔS is the surface bounded by the curve. Large closed curves can be treated by dividing them into many small closed curves. The total change in phase is then:

$$\Delta\phi = 2\pi \Sigma n + (e/\hbar c) \int_{S} \vec{B} \cdot d\vec{S} \qquad (1.2)$$

where the integration is over the surface S bounded by the large curve and the sum is over all nodal lines that pass through it, (with care taken to assign proper signs to each term). The second term is the same for all wave functions while the first may be different for different wave functions.

Equation (1.2) applied to any surface is the change in phase around the boundary of that surface and therefore must vanish for a closed surface. In that case:

$$2\pi \Sigma n = - (e/\hbar c) \int \vec{B} \cdot d\vec{S}$$

where the integral is over the closed surface. If Σn does not vanish, then some nodal lines must have endpoints inside the surface. (Otherwise the nodal lines will each cross the surface twice, (or four times, etc.) and contribute equal and opposite amounts to Σn.) Since the second term in (1.2) is the same for all wave functions it can be seen that Σn must also be the same for all wave functions when $\Delta\phi = 0$. Thus Dirac concluded " . . . it follows that the end points of nodal lines must be the same for all wave functions. These end points are then points of singularity in the electromagnetic field."

One calculates the total flux of magnetic field crossing a small closed surface surrounding one of these points to be:

$$4\pi g = 2\pi n \hbar c/e \qquad (1.3)$$

Thus at the endpoint of a nodal line characterized by the integer n there is a magnetic pole of strength g where:[3]

$$g = n \frac{\hbar c}{2e} \qquad (1.4)$$

Dirac concluded, ". . . the present formalism of quantum mechanics, when developed naturally without the imposition of arbitrary restrictions, leads inevitably to wave equations whose only physical interpretation is the motion of an electron in the field of a single pole. This new development requires no change whatever in the formalism . . . Under these circumstances one would be surprised if Nature had made no use of it."[1]

Monopoles Without Strings

In contemporary terminology the nodal line of singularity ending on the magnetic pole is called the "Dirac string". The string appears in both the definition of the wave function and that of the vector potential $\vec{A}$ of the electromagnetic field, (although, as mentioned by Dirac,[1] the position of the line of singularity need not be chosen to be the same for both functions). Wu and Yang[4] noted that the wave function of an electrically charged particle in the presence of a monopole should have no singularities since the space around a monopole is spherically symmetric and is itself without intrinsic

singularities. They observed that the discontinuities arise because any choice of vector potential $\vec{A}$ around the monopole must have singularities in much the same way that the choice of a coordinate system on the surface of a sphere, (such as a longitude and latitude system) always leads to singularities[5] in spite of the fact that the sphere does not have intrinsic singularities. To avoid this problem a sphere can be divided into overlapping regions in which singularity-free coordinate systems are defined. Where the regions overlap, one can find singularity-free coordinate transformations between the different coordinate systems.

In an analogous manner, the space surrounding the monopole can be divided into two regions in which singularity-free vector potentials can be defined. Where the two regions overlap it is found that the potentials can be simply related by a gauge transformation if and only if the Dirac quantization condition holds. (If this condition is not met then the gauge transformation phase factor is not single-valued.)[5] Wu and Yang also showed that the generalized spherical harmonics developed by Tamm[6] to study the electron wave function in the vicinity of a monopole can be used to obtain singularity-free wave functions. To this end they again use two overlapping regions on which singularity-free "monopole harmonics" can be defined. The wave function is represented by an expansion of the harmonics in each region and the wave functions for the separate regions are related by a phase factor which is simply the gauge transformation phase factor relating the vector potentials of the two regions.

Searches for the Dirac Monopole

The Dirac theory predicts only the magnetic charge of the monopole. In order to search for monopoles, experimentalists had to make some assumption about the monopole mass. A common ad hoc assumption was that the monopole would have the same classical radius as the electron. This leads to a mass $M \sim 2.4\ GeV/c^2$, for a single Dirac charge. Such monopoles would be detectable by any number of methods.[7] In particular, such particles would be accelerated to relativistic velocities by galactic magnetic fields and so would lose energy in matter like relativistic nuclei with $z = 137/2$ units of charge. They could be strongly deflected by laboratory produced magnetic fields[8] and they would range out and become trapped in surface materials.[9] They would also be light enough to be pair-produced at accelerators.[10] There were many experiments performed which were based upon these considerations. None of them turned up any unambiguous evidence for monopoles.

In spite of the fact that none were discovered, monopoles retained a significant status in physics by virtue of the fact that they were as yet the only means by which the quantization of electric charge could be understood. By the early 1970's however, it appeared as though Grand Unified Theories (GUTs) would provide an alternative explanation for this phenomenon.

Monopoles in Grand Unified Theories:[11] The 't Hooft-Polyakov Model

Strong, weak, and electromagnetic interactions are all well described by gauge field theories. This fact offers the prospect that perhaps they are all merely different aspects of a single gauge theory. Theories of this kind are called "Grand Unified Theories," (GUTs). In these theories the separate gauge theories of the different interactions are all imbedded in a larger non-Abelian group structure. As a result, the gauge fields will have non-vanishing commutators so that only one coupling strength is possible.[12] The charge operators, including electric charge, will have eigenvalues determined by the group coupling constant and the eigenvalues associated with the group commutation relations. These relations require the electric charge operator Q to have eigenvalues which are integer multiplies of a fundamental unit. Charge quantization therefore comes about naturally in any GUT which does not have an Abelian U(1) factor.[13] Furthermore, this conclusion is true even if the symmetries generated by the charges that fail to commute with Q are spontaneously broken.[14] It would therefore appear that GUTs offer not only an elegantly simple description of the fundamental interactions, but also an explanation of charge quantization which does not require the existence of magnetic monopoles. This fact, together with the non-observation of monopoles discussed in the last section severely dampened any interest in magnetic monopoles that may have previously existed.

In 1974, however, interest in monopoles was revived with the discovery by 't Hooft[15] and, independently by Polyakov[16] that monopoles are required in spontaneously broken gauge field theories. Like Dirac,[1] they found once again that there exists a deep relationship between the quantization of electric charge and magnetic monopoles. Unlike Dirac's monopole however, the monopole that they found in grand unified theories is non-singular and has a calculable mass and core size and a complicated structure.

Their result is best illustrated by consideration of the simple example in which the SO(3) gauge group is spontaneously broken to a U(1) subgroup.[17] This is known as the Georgi-Glashow[18] model and consists of an SO(3) gauge field interacting with an isovector Higgs field $\vec{\phi}$. The Lagrangian is:

$$L = -\frac{1}{4} G_a^{\mu\nu} G_{a\mu\nu} + \frac{1}{2} D^\mu\vec{\phi} \cdot D_\mu\vec{\phi} - V(\vec{\phi}) \tag{1.5}$$

Where $G_a^{\mu\nu}$ is the gauge field strength tensor:

$$G_a^{\mu\nu} = [D^\mu, D^\nu] = \partial^\mu W_a^{\ \nu} - \partial^\nu W_a^{\ \mu} - q\,\epsilon_{abc}\, W_b^{\ \mu} W_c^{\ \nu} \tag{1.6}$$

and $W_a^{\ \mu}$, (a = 1,2,3), are the gauge potentials. The covariant derivative of $\vec{\phi}$ is given by:

$$(D^\mu\phi)_a = \partial^\mu\phi_a - q\,\epsilon_{abc}\, W_b^{\ \mu}\phi_c \tag{1.7}$$

The potential function $V(\vec{\phi})$ is:

$$V(\vec{\phi}) = \frac{1}{4}\lambda\,(\phi_1^2 + \phi_2^2 + \phi_3^2 - v^2)^2 \tag{1.8}$$

and so it is of the form required to give degenerate vacua as is necessary for spontaneous symmetry breaking to occur. The equations of motion are:

$$(D_\nu G^{\mu\nu})_a = -q\,\epsilon_{abc}\phi_b\,(D^\mu\phi)_c \qquad (1.9)$$

$$(D^\mu D_\mu \phi)_a = -\lambda\phi_a(|\vec{\phi}|^2 - v^2)^2$$

The energy density corresponding to the Lagrangian is:

$$\theta_{oo} = \frac{1}{2}\left\{e^i_a e_{ai} + b^i_a b_{ai} + (\pi_a)^2 + D^i\phi_a D_i\phi_a\right\} + V(\vec{\phi}) \qquad (1.10)$$

where $G_a^{oi} = -e^i_a$, $G^{ij}_a = -\epsilon_{ijk}\,b^k_a$, and $\pi_a = (D^o\phi)_a$. Thus θ_{oo} is positive or zero and vanishes if and only if:

$$G_a^{\mu\nu} = (D^\mu\phi)_a = V(\vec{\phi}) = 0 \qquad (1.11)$$

In the vacuum configuration, (1.11) is true everywhere. An example is given by:

$$\phi_a = v\,\delta_{a3},\ W_a^\mu = 0 \qquad (1.12)$$

Since $\theta_{oo} = 0$ is a gauge invariant, any gauge transformation of expressions (1.12) will also yield a viable vacuum configuration.

The Higgs vacuum is defined as the configuration in which $G_a^{\mu\nu}$ is not necessarily zero and where $D^\mu\vec{\phi}$ and $V(\vec{\phi})$ may be nonzero over some finite region of space. They must, however, vanish sufficiently rapidly at spatial infinity to assure that the total field energy is finite. Thus asymptotically $\vec{\phi}$ must be a member of the set A_o where

TABLE 1

PARTICLE SPECTRUM AND PARTICLE PROPERTIES
IN THE GEORGI-GLASHOW[18] MODEL

Particle	Symbol	Mass	Spin	Charge
Higgs	H	$\frac{1}{2}v\sqrt{2\lambda}$	0	0
Photon	γ	0	$\frac{1}{2}$	0
Massive Gauge Particles	$X^{\pm}$	$vq\frac{1}{2}$	$\frac{1}{2}$	$\pm q\frac{1}{2}$

$A_o = \{\vec{\phi}: V(\vec{\phi}) = 0\}$. A_o is essentially S^2, a two dimensional sphere of radius v in internal space. For a fixed $\vec{\phi}$ in A_o, H is the subgroup of G whose elements leave $\vec{\phi}$ invariant; (i.e. the group of rotations about the ϕ axis).[19] The choice of a fixed $\vec{\phi} \in A_o$ thus spontaneously breaks the original group of symmetries, G, to the smaller group H.

The particle spectrum is obtained by expanding the Lagrangian about the vacuum expectation value of the Higgs field. In the usual way the coefficients of quadratic terms will correspond to masses squared, divided by $2\hbar^2$. Because the vacuum expectation value of the Higgs field is non-zero, the Higgs mechanism,[20] or "screening current effect"[21] operates. As a result, the charged components of the Higgs field are absorbed into the charged components of the gauge field giving them a specified mass. There remains a single massless vector particle, (the photon), and also a massive scalar Higgs. The particle spectrum is listed in table 1.

To find the electric charge we compare the SO(3) covariant derivative;

$$D^\mu = \partial^\mu + iq\, W_a^{\ \mu}\, T_a$$

where $(T_a)_{ij} = i\,\epsilon_{aij}$, with the electromagnetic covariant derivative; $\partial^\mu + i\,Q\,A^\mu/\hbar$. We identify the component of the gauge field which remains massless, i.e. $\vec{\phi} \cdot \vec{W}^\mu/v = W_3^{\ \mu}$, with the electromagnetic gauge field A^μ of the photon. Thus;

$$Q = \frac{q\hbar}{v}\ \vec{\phi} \cdot \vec{T} \qquad (1.13)$$

Since then;

$$(Q/\not{h})\ A^{\mu} = (q/v\ \vec{\phi}\ \cdot\ \vec{T})(1/v\ \vec{\phi}\ \cdot\ \vec{W}^{\mu}) = (q/v)\ v\ T_3\ \frac{1}{v}\ W_3^{\mu}\ v = q\ T_3\ W_3^{\mu}$$

as required. Since the T_a have integer eigenvalues[22] we see immediately that the eigenvalues of Q are quantized.

We have now extracted the obvious features of the SO(3) gauge field theory. In order to uncover the 't Hooft-Polyakov monopole solution we have to do some digging. As discussed above, the requirement of finite energy forces the fields to be in the Higgs vacuum asymptotically so that at large distances only electromagnetic characteristics may survive. The "twist" to the monopole solution will be that the phase of the asymptotic vacuum expectation value of the Higgs field will be space dependent.

The approach taken by 't Hooft and Polyakov was to seek non-singular finite-energy classical solutions to the equations of motion for which the isovector Higgs field is not a constant. They reasoned that a solution of this sort with lowest non-zero energy should be highly symmetric. Symmetry considerations can therefore be used to simplify the search for a solution with the desired characteristics.

We seek a time-independent solution which means that a Lorentz frame has to be chosen in which the fields are at rest. As a result, the equations of motion in this frame have SO(3) spatial rotational symmetry, and a translational symmetry. There is also an internal SO(3) symmetry of gauge rotations of the Higgs field and two discrete symmetries which we label P and Z. P is the parity operation and Z inverts the Higgs isovector in internal space. Since the definition

of the electromagnetic field strength tensor follows from the definition of the potential, ($\vec{A}^{\mu} = \vec{\phi} \cdot \vec{W}^{\mu}/v$), as $F^{\mu\nu} = \vec{\phi} \cdot \vec{G}_{\mu\nu}/v$, the discrete symmetries acting on $F^{\mu\nu}$ are:

$$\begin{aligned} &P: \quad F^{ij}(\vec{r}) \to F^{ij}(-\vec{r}), \; F^{io}(\vec{r}) \to -F^{io}(-\vec{r}) \\ &Z: \quad F^{ij}(\vec{r}) \to -F^{ij}(\vec{r}), \; F^{io}(\vec{r}) \to -F^{io}(\vec{r}) \end{aligned} \tag{1.14}$$

Thus both P and Z reverse the sign of $\vec{\nabla} \cdot \vec{B}$ so that any solution for which either of them are good symmetries cannot have magnetic charge. The product PZ however, which generates Z_2, the cyclic group of order 2, does not reverse the sign of $\vec{\nabla} \cdot \vec{B}$.

We must disregard translational invariance in order that the solution be particle-like, (localized in space) so that of the continuous symmetries we are left with SO(3) $\times$ SO(3) which is the group of products of real and internal space rotations. Invariance for spatial rotations alone forces $\vec{\phi}$ to be constant and so yields nothing new. Isotopic rotational invariance forces $\vec{\phi}$ to vanish everywhere which does not satisfy the Higgs vacuum requirements. Let's consider solutions which are invariant for elements of the diagonal subgroup in SO(3) $\times$ SO(3) consisting of simultaneous and <u>equal</u> rotations in both spaces. Thus we will expect that, asymptotically, the internal space direction of the Higgs field will be correlated with the direction of the position vector $\vec{r}$ in real space.

The diagonal subgroup is isomorphic to SO(3) and has generators $-i\vec{r} \times \vec{\nabla} + \vec{T}$. The most general solution of equation (1.9) having the symmetries of this group must be of the form:

$$\phi_a(\vec{r}) = N(vqr)\ r_a/qr^2\ ,\ W_a{}^o(\vec{r}) = J(vqr)\ r_a/q\ r^2$$

$$W_a{}^i(\vec{r}) = -\epsilon_{aij}\frac{r^j}{qr^2}\ [1 - K(vqr)] + \frac{r^2\delta_{ai} - r^i r_a}{qr^3}\ B(vqr) + \frac{r^j r_a}{qr^3}\ C(vrq)$$

where N, J, K, B, and C are general functions of vqr. Invariance with respect to PZ forces B = C = 0. The final invariance group of the solution is thus $H_o \tilde{=} SO(3) \times Z_2$.

If we set J = 0 for the moment, then we have:

$$W_a{}^o = 0;\ \phi_a = \frac{r^a}{qr^2}\ N(vqr);\ W_a{}^i = -\epsilon_{aij}\frac{r^j}{qr^2}\ [1 - K(vqr)] \qquad (1.15)$$

The asymptotic condition on $\vec{\phi}$, namely $\vec{\phi} \in A_o$, can be satisfied for (1.15) by requiring that for large r we have N(vqr) = vqr. Then:

$$\lim_{r \to \infty}\ \vec{\phi}(\vec{r}) \equiv \vec{\phi}_\infty(\vec{r}) = v\hat{r}$$

so that $|\vec{\phi}_\infty| = v$ as required. For very large r we therefore find that $\vec{\phi}$ maps each point on the sphere S^2, corresponding to the possible directions in which $\vec{r}$ can approach infinity, to the corresponding point on A_o which is also S^2. Furthermore this field configuration cannot be continuously deformed into the constant map[23] so that the solution must be stable against decay into the vacuum. The corresponding energy of this solution is:

$$E = -\int L\ d^3x \qquad (1.16)$$

$$= \frac{4\pi v}{q}\int_o^\infty \frac{d\eta}{\eta}\left[\frac{\lambda}{4q^2}\ (N^2-\eta^2)^2 + K^2N^2 + \frac{1}{2}\ (K^2-1)^2 + \frac{1}{2}\ \left(\eta\frac{dN}{d\eta} - N\right)^2 + \eta^2\left(\frac{dK}{d\eta}\right)^2\right]$$

where $\eta \equiv vqr$. To find the minimum E, we require that E be stationary for variations of N and K. This yields the equations:

$$\eta^2 \frac{d^2K}{d\eta^2} = KN^2 + K(K^2 - 1)$$
$$\eta^2 \frac{d^2N}{d\eta^2} = 2K^2N + \frac{\lambda}{q^2} N(N^2 - \eta^2) \tag{1.17}$$

The boundary conditions for finite energy are:

$$K - 1 \leq 0(\eta), \quad N \leq 0(\eta) \qquad \text{for } \eta \to 0$$
$$K \to 0, \qquad N \sim \eta \qquad \text{for } \eta \to \infty \tag{1.18}$$

The total energy is interpreted as the classical mass and can be written:

$$M = E = \frac{4\pi v}{q} f(\lambda/q^2) \tag{1.19}$$

where $f \in [1.0, 1.787]$.[14] From the conditions (1.18) it follows that $G_a{}^{ij}$ has asymptotic form:

$$G_a{}^{ij} \sim \frac{1}{qr^4} \epsilon_{ijk} r_a r^k \sim \frac{1}{vqr^3} \epsilon_{ijk} r^k \phi_a$$

The electromagnetic field strength tensor is thus

$$F^{ij} = \vec{\phi} \cdot \vec{G}^{ij}/v = \frac{r^k}{vqr^3} \epsilon_{ijk} |\vec{\phi}|^2/v = \epsilon_{ijk} \frac{1}{q} \frac{r^k}{r^3}$$

We know however that $F^{ij} = -\epsilon_{ijk} B^k$ so that we have a magnetic field:

$$\vec{B} = -\frac{1}{q} \frac{\vec{r}}{r^3}$$

We have thus found a stable magnetic monopole solution with magnetic charge;[24] $g = \hbar c/2e$.

We have constructed a magnetically charged soliton for which the charge is topological, corresponding to a conserved topological current rather than a Noether current. The concept of topological charge is most easily visualized in the Sine-Gordon model in one spatial dimension. The field equations in this model can be thought of as representing a classical system composed of clothespins on a clothesline under the action of gravity and in the limit of zero spacing between pins.[25] The zero energy, (vacuum) configuration corresponds to all pins hanging down. The finite energy soliton solution, much like the monopole solution described above, has field values outside the vacuum over a finite interval, (i.e. the pegs point up over this interval) as a result of a twist. The twist must be an integer multiple of 2π in order that the pegs hang down at $x = \pm\infty$ as demanded by the finite energy requirement. The integer multiple, or winding number of the twist, is the topological charge of the soliton. For the SO(3) case the topological charge is the winding number corresponding to the number of times $\vec{\phi}$ covers S^2 in internal space as $\vec{r}$ covers S^2 at infinity in real space. For the asymptotic expression (1.15) this number is unity.

Although we have only considered SO(3), the existence of monopoles with topological charges is a general requirement of any gauge group G which is simple and which is spontaneously broken to a subgroup that contains a U(1) factor.[26]

Let us now consider the microscopic structure of GUT monopoles. At infinity $\vec{\phi} \in A_o$, where $A_o = \{\vec{\phi}: \quad V(\vec{\phi}) = 0\}$, but deep inside the

monopole[27] $\vec{\phi}$ may depart significantly from its vacuum expectation value. The size of the monopole core is determined by competing energetic effects - the energy of the magnetic field outside the core:

$$E_{mag} \sim 4\pi g^2 R_c^{-1} \sim \frac{4\pi}{e^2} R_c^{-1}$$

and the energy due to the twisted scalar field in the core:

$$E_{scalar} \sim 4\pi v^2 R_c \sim \frac{4\pi}{e^2} M_x^2 R_c$$

where R_c is the core size and M_x is the mass of the heavy vector bosons of the theory. Minimizing the sum of these two energies yields $R_c \sim M_x^{-1}$. From (1.19) and table 1 the monopole mass is thus:

$$M \sim \frac{4\pi v}{q} \sim \frac{M_x}{\alpha} \qquad (1.21)$$

where α is the fine structure constant. In general M_x is not known but if we assume there are no new interactions between 100 GeV and the unification scale, (Glashow's "desert hypothesis"), then $M_x \gtrsim 10^{14}$ GeV and so $R_c \lesssim 10^{-28}$ cm and $M \gtrsim 10^{16}$ GeV. The monopole will have layers of structure beyond its core. In particular, there will be a sea of W and Z bosons at $\sim 10^{-16}$ cm, a color magnetic field out to ~1 fm, and a cloud of e^-e^+ pairs to $\sim 10^{-11}$ cm. Beyond this the monopole will have only a radial magnetic field.

Monopoles in the Early Universe

Although the monopole solution has been found in spontaneously broken unified gauge field theories it doesn't necessarily follow that

monopoles exist. If monopoles are supermassive then they cannot be produced by any process in the universe at the present time. They could only have been produced in the very early universe when temperatures, and hence available energies, were much greater.

At sufficiently high energy that the full grand unified gauge symmetry is yet unbroken, monopoles cannot exist. We have seen in the last section that the breaking of this symmetry is a necessary step toward a monopole solution. Thus monopoles could only form when the universe cooled below a critical temperature at which the spontaneous symmetry breakdown could occur. At this time the scalar order parameter $\vec{\phi}$ obtains a fixed arbitrary direction in internal space and has a magnitude v so that $V(\vec{\phi})$ is zero and the standard vacuum configuration is obtained.[28] As a result of thermal fluctuations there will be different regions in which the fluctuating order parameter will point in different directions, (i.e. have different phases). These regions cannot be brought together without trapping a topological defect where they meet. This defect is precisely a magnetic monopole.

We therefore expect something on the order of one monopole per region throughout which the order parameter has a single direction. It is not certain how large these regions were but we can place a limit on their size by demanding that the order parameter not be correlated over distances larger than the distance that light could travel from the time of the initial singularity.[29,30] In the standard Big Bang model this leads to a monopole abundance comparable to the

abundance of baryons, which is absurd. This is the so-called "monopole problem."

An elegant way of suppressing the monopole abundance without discarding grand unification is the "inflationary universe" scenario.[31] In this scenario the universe went through a period of exponential expansion in which the scalar field during the inflation is the Higgs field. This field is appropriately uniform throughout the coherence region which has now been stretched to be much larger than the observed universe. The monopole abundance in the universe as a result of disorder in the Higgs field is then on the order of one per universe. Note however that in some models, the reheating of the universe which is expected to occur subsequent to the period of rapid inflation, could have produced a small but acceptable and perhaps detectable monopole abundance.

Astrophysical Bounds on the Monopole Flux in the Galaxy

The fact that monopoles have not been observed is of itself very significant since it tells us something about the evolution of the early universe and has fueled the development of such ideas as the inflationary universe scenario discussed above. Even more could be learned of course by the positive detection of a monopole flux. As it turns out there are astrophysical considerations which can be used to guide experimental searches for monopoles by placing bounds on the galactic monopole flux based upon astrophysical observations.

E.N. Parker et al.[32] argue that the flux of free magnetic monopoles in the galaxy must not be great enough to drain energy from the galactic magnetic fields faster than they can be regenerated by the galactic dynamo. The fields have a strength of ~3 μGauss and are coherent over distances of $\sim 10^{21}$ cm but are assumed by Parker to be completely uncorrelated from one to another domain. For monopoles having a mass of $\sim 10^{17}$ GeV/c^2 these fields will accelerate them to a velocity $v \sim 10^{-3}$ c. Above 10^{17} GeV/c^2, gravitation is the dominant interaction of monopoles with the galaxy. In this case they would again be expected to have velocities of $\sim 10^{-3}$ c corresponding to the typical galactic escape velocity. The Parker flux limit is:

$$f_{Parker} \lesssim \begin{cases} 10^{-15} \text{ cm}^{-2} \text{ sr}^{-1} \text{ sec}^{-1}, & M \leq 10^{17} \text{ GeV}/c^2 \\ 10^{-15} \, (Mc^2/10^{17} \text{ GeV}) \text{ cm}^{-2} \text{ sr}^{-1} \text{ sec}^{-1}, & M \geq 10^{17} \text{ GeV}/c^2 \end{cases} \tag{1.22}$$

For $v \sim 10^{-3}$ c another flux limit is obtained by demanding that the total mass of monopoles in the galaxy not exceed the galactic mass of about 10^{12} solar masses. This yields:

$$f_{galactic} \lesssim 10^{-10} \, (10^{17} \text{ GeV}/Mc^2) \text{ cm}^{-2} \text{ sr}^{-1} \text{ sec}^{-1} \tag{1.23}$$

The two limits (1.22) and (1.23) when combined, predict a flux below 10^{-15} cm^{-2} sr^{-1} sec^{-1} everywhere outside the mass range: $Mc^2 \in [10^{17}, 10^{22}]$ GeV. A maximum allowable flux, $f_{max} \sim 3.0 \times 10^{-13}$ cm^{-2} sr^{-1} sec^{-1}, occurs at a monopole mass of $\sim 3 \times 10^{19}$ GeV/c^2.[33]

Even more stringent flux limits are obtained by considering astrophysical consequences of monopole catalysis of nucleon decay.[34]

Monopoles may be captured by neutron stars, catalyzing nucleon decay at an intense rate thereby heating the star which then emits x-rays.[35] From x-ray luminosity measurements we then obtain limits on the product of monopole flux and catalysis cross-section. For a cross section of 10^{-28} cm^2, (i.e. almost a strong interaction cross section), the flux limit obtained is 6 orders of magnitude lower than the Parker bound. There are however many possible criticisms of this scenario including the possibility that monopoles do not catalyze nucleon decay.

CHAPTER II

THE EXPERIMENTAL TECHNIQUE

Introduction

The previously unexpected large mass of grand unification monopoles have made it necessary to develop new methods to detect them. Previous experiments, in which a mass of ~2.4 GeV/c^2 was assumed, would not have been sensitive to super-massive monopoles. In particular, such monopoles could not be produced in accelerator interactions,[36] may be too energetic to be stopped in surface materials[37] or to be deflected by laboratory magnetic fields,[38] and could be too slow to ionize heavily.[39] Consequently, monopoles are sought predominantly as cosmic ray particles although at least one experiment has looked for monopoles trapped in old iron ore samples.[40]

Among the cosmic ray searches, the most sensitive, an experiment by Price et al.[41] searched for tracks left by monopoles in ancient mica. This experiment however requires that an Al nucleus be bound to the monopole. Proton decay experiments[42] set bounds on the monopole flux by assuming that monopoles induce nucleon decay. Large ionization detectors, such as those of Webb et al.[43] in Texas, and that of Alexeyev et al.[44] in the Baksan mine of the USSR set limits in the 10^{-14} cm^{-2} sr^{-1} sec^{-1} range but depend upon monopole velocities. In particular, Ahlen et al.[45] and Ritson[46] have calculated that

monopoles with velocities above ~5 x 10^{-4}c will ionize certain scintillator materials sufficiently to produce a detectable signal. The monopole velocity[47] however is expected to be ~10^{-3}c which is extremely close to the calculated threshold of these detectors. Unfortunately, the signal depends upon the microscopic details of the interaction of the monopole with matter so that direct calibration is not possible.[48]

The above experiments, while displaying a broad range of creativity and ingenuity, cannot yield unqualified flux limits in the absence of a monopole signal. This is because each of these experiments makes assumptions about the properties of the monopole and its interactions with matter which are consistent with some but not all current monopole theories. In addition, none of the detectors used in these experiments can be directly calibrated and consequently we must ultimately accept their sensitivity to monopoles on faith.

The detection of monopoles by an induced current in a conducting loop is the only technique which does not suffer from these shortcomings. For this method, the only assumption that must be made about the monopole is that it carry a magnetic charge of at least $e/2\alpha$ = 68.5e which is consistent with all of the theories. The induction technique is also unique in that the signal is produced by a macroscopic change in the field at the loop and is therefore accessible to direct calibration. We conclude that this method of searching for monopoles is unrivaled in its comprehensiveness and in its inherent simplicity. In the past, however, induction detectors

have been limited to small sensitive areas by the requirement of operating in ultra-low magnetic fields and also because the detector loop had to be small compared to the dimensions of the superconducting shield in which it was enclosed in order to avoid a loss in signal due to inductive coupling. Our efforts have been directed toward overcoming these constraints in order to make it possible to construct inexpensive, large area induction detectors. In this thesis I will describe several experiments which have been largely successful in this task. First, however, I will summarize the work which has preceded ours in order to illuminate the problems that we faced when we began our experimental program less than four years ago.

The Evolution of the Induction Technique

The basic principle of the technique dates back to before 1831 when Faraday[49] showed that the passage of a magnetic pole, (in this case the end of a solenoid), through a closed conducting loop induces a current. The use of a superconducting loop to detect the passage of a magnetic monopole was first suggested by L.W. Alvarez[50] in 1963 and independently by L.J. Tassie[51] in 1965. The size of the monopole signal was also calculated by P.H. Eberhard[52] in 1964.

To take into account the possible existence of free magnetic charge, Faraday's law must be modified by the inclusion of a magnetic current term, so that:

$$\vec{\nabla} \times \vec{E} - \frac{1}{c} \frac{\partial \vec{B}}{\partial t} = \frac{-4\pi}{c} \vec{J}_m$$

Using this expression we can calculate the current induced in a superconducting loop when a monopole of charge g passes through it. Suppose the monopole passes through the loop at $t = t_o$. Then the magnetic current through the loop is;

$$I_m = \int_S \vec{J}_m \cdot \hat{n}\, dS = g\, \delta(t - t_o)$$

where the integral is over the loop surface. Integrating Faraday's law thus gives;

$$\int_S \vec{\nabla} \times \vec{E} \cdot \hat{n}\, dS - \frac{1}{c} \frac{\partial}{\partial t} \int_S \vec{B} \cdot \hat{n}\, dS = \frac{-4\pi}{c} g\, \delta(t - t_o)$$

Note however that by Stoke's theorem,

$$\int_S \vec{\nabla} \times \vec{E} \cdot \hat{n}\, dS = \int_C \vec{E} \cdot \vec{dl}$$

where C is a closed contour bounding the surface S. For a superconducting loop we can choose C to lie deep inside the ring where the electric field is zero. Then $\int_C \vec{E} \cdot d\vec{l} = 0$ and we have:

$$\frac{1}{c} \frac{\partial}{\partial t} \int_S \vec{B} \cdot \hat{n}\, dS = \frac{4\pi}{c} g\, \delta(t - t_o)$$

i.e.,

$$\frac{\partial \Phi}{\partial t} = 4\pi\, g\, \delta(t - t_o)$$

and so there is a net change of flux in the loop. The net current induced in the loop is thus; $i = 4\pi g/L$ where L is the loop self-inductance.

The first proposal for an induction detector was submitted by Alvarez, Eberhard, et al.[53] The detector was used to search 8.3 kg of

lunar material and 20.0 kg of other materials including 2.4 kg of ocean floor sediment.[9] It was also used to analyze an emulsion containing an unusual stopping track from a search by Kolm et al.[54] No monopole candidates were observed.

The use of a superconducting quantum interference device, (SQUID), to monitor the current in the loop was introduced by L.L. Vant-Hull[55] in 1968. (This experiment precedes that of Alvarez, Eberhard et al. but was proposed later. It is of course quicker to do experiments that do not require trips to the moon.) In the Vant-Hull experiment, samples were passed directly through the SQUID interferometer loop. The materials that were studied included 0.043 kg of Cu and 0.049 kg of W and Au. In addition, a beam of 7×10^{21} electrons was also passed through the loop. From this latter experiment a limit was placed on the magnetic charge of electrons of $g_e \leq 4 \times 10^{-24}$ Dirac-charges per electric charge. From the other samples the difference in magnetic charges of the proton and electron was limited to $g_p - g_e \leq 10^{-26}$ Dirac-charges.[56]

In 1982 the induction method became widely known as a result of the experiment of B. Cabrera[57] who applied the technique to search for cosmic-ray monopoles. This experiment operated a 5-cm-diameter, 4-turn coil of superconducting Nb wire in a carefully constructed volume where the background magnetic field had been reduced to 5×10^{-8} G. As in the experiment by Vant-Hull, discussed above, the current in the coil was monitored by means of a SQUID. A single Dirac-charge monopole candidate was observed in an exposure of 151

days. This event, if a true monopole, would then indicate a flux of 6.1×10^{-10} cm^{-2} sr^{-1} sec^{-1} which contradicts the Parker bound by more than four orders of magnitude. A second experiment by Cabrera et al.[58] used three separate loops of larger diameter. The loops were wound on a hollow 10.2-cm-diameter pyrex sphere and occupied mutually orthogonal planes. The mutual inductance of any pair of loops was thus zero while the probability that a monopole inducing a current in one loop would also induce a current in a second loop was very high. In 121.5 days of active operation there were no candidate monopole events and an upper limit on the monopole flux of $f_m \lesssim 3.7 \times 10^{-11}$ cm^{-2} sr^{-1} sec^{-1}, (90% C.L.), was set.

Considerations for Large Area Detectors

The total magnetic flux associated with a single Dirac-charge monopole[1] is $2\phi_o = 4\pi g_D = 4.14 \times 10^{-7}$ G-cm^2, (where $\phi_o = hc/2e$ is the magnetic flux quantum and g_D is the smallest Dirac charge). Over the surface of a 5-cm-diameter induction loop, a change in flux of this amount could be produced by a fluctuation of only $\sim 2 \times 10^{-8}$ G in a uniform ambient field. Fluctuations in the earth's magnetic field are typically many orders of magnitude greater than this value.

To avoid the problem of noise associated with changes in ambient fields, B. Cabrera[57,58] reduced the field in his apparatus to $\sim 5 \times 10^{-8}$ G. This was achieved with the aid of 20-cm-diameter Pb foil cylinders[59] which were accordioned flat during cooldown and then expanded like balloons. As the Pb is cooled below the superconducting

transition temperature a fraction of the ambient magnetic field is expelled as predicted by the Meissner effect. The remaining magnetic flux is trapped and rigidly fixed at pin-sites in the foil. The pin-sites correspond to impurities and local thickness minima which act as potential wells in which flux quanta can become bound.[60] When the cylinder is then inflated, the pin-sites get displaced to a larger mean separation from one another so that the field inside the cylinder is diluted. Cylinders can be expanded repeatedly, one inside of the previous one, to reduce the field on the interior to the level of only a few magnetic flux quanta. The Pb foil also shields the interior region from subsequent external field variations.

Unfortunately this technique is too delicate to be used to reduce magnetic fields throughout regions significantly larger than 20 cm in diameter. An alternative procedure would be to stabilize the ambient field to the extent that residual fluctuations can only result in flux changes smaller than $4\pi g_D$ over the surface of the detector loop. We hypothesized that flux-pinning in a hollow and closed superconducting surface would be sufficient for this purpose. Our hope was that a detector loop inside a region of this sort would experience no significant flux variation if its position relative to the surrounding superconductor, (and hence the stable magnetic field), did not alter.

In order to test our hypothesis we constructed a small prototype detector, (figure 1), that was operated in ~100mG magnetic fields in the summer of 1982 at the Fermilab village firestation. The

Figure 1. Prototype detector operated at Fermilab. This early prototype detector operated in 1982 at the Fermilab village firestation demonstrated that field-pinning in a completely closed superconducting shield could be sufficient to yield a low background of flux variations over the surface of a detector loop on the interior.

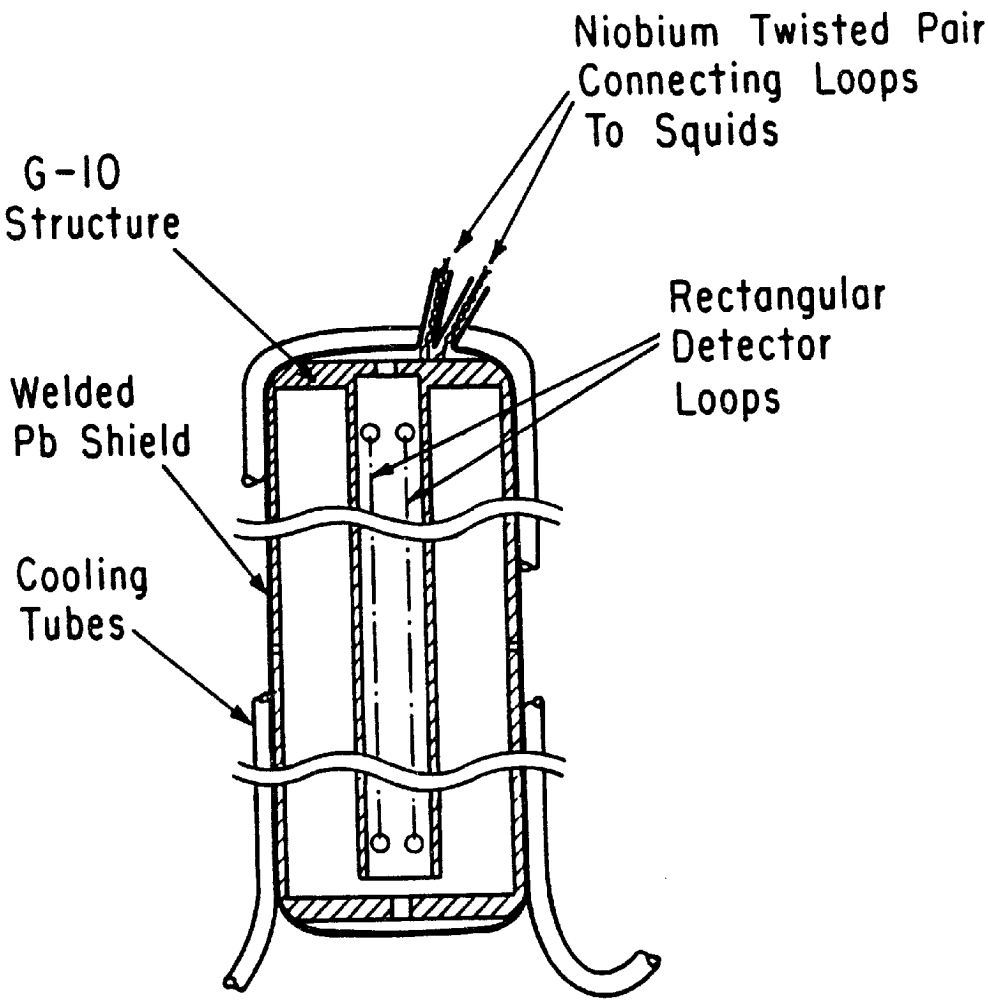

detector contained two 45 cm x 2.5 cm rectangular loops. These were wound about a G-10 form which was mechanically secured to the interior of a G-10 cylinder 8 cm in diameter and 50-cm-long. The superconducting shield was constructed by covering the G-10 cylinder and endcaps with 1 mm thick Pb sheets. The separate sheets were welded together with Pb where they joined in order to insure that the surface was completely closed. By connecting both the detector loops and the Pb foil to a common G-10 structure we were assured that their relative motion would be at a minimum.

Hollow Pb tubing was attached to the Pb shield and filled with LHe in order to cool the detector to a temperature below the superconducting transition temperatures of the shield and the loops. The loop currents were monitored by rf SQUIDs.[61] The SQUID produces a voltage output signal proportional to a current in a 2μH input inductor. (Typically the proportionality constant is $\sim 10^{10}$ V-A^{-1}.) SQUID signals were passed through a 1 Hz low-pass-filter and a continuous a.c. noise background of ~1 mV pp, (peak to peak) was observed. The signal expected for a single Dirac-charge monopole, on the other hand, was a d.c. offset of 23 ± 2 mV.

The detector was operated for 48 days. During this time the a.c. noise background remained stable at ~1.0 mV pp, (1 Hz), with a tendency to increase to 2-3 mV pp when the LHe level was low and boiling caused vibration of the detector. We also observed 32 d.c. offsets in the signal, (figure 2). We learned that such offsets could be generated by environmental disturbances such as vibrations, sudden

large variations in the ambient magnetic field, and even by a change of pressure in the LHe reservoir. One of the observed d.c. offsets was consistent with the signal expected for a single Dirac-charge monopole, (figure 3). This was not considered a candidate magnetic monopole event in view of the fact that the detector was unable to show unequivocally whether an environmental disturbance had occurred. In this respect the prototype had fallen short of complete success. It was apparent, however, that very few modifications would be necessary to construct a detector capable of detecting a monopole unambiguously. The Fermilab prototype design could easily be improved by incorporating some better means of isolating it from sources of spurious signals and by monitoring those sources. Improved isolation from sources of vibration could be obtained, for instance, by operating it in vacuum and suspending it with vibration damping devices. Environmental disturbances could easily be monitored with appropriate sensors. Finally, to safeguard against rare spurious signals due to disturbances that are not detected by the monitors, two detector loops could be operated in coincidence with one another. The two loops could be independently isolated from the environment, (and consequently from one another), to insure that the probability of simultaneous false monopole signals would be negligible. In chapter IV the results from a detector which successfully incorporates these considerations to operate in ambient magnetic fields of ~1-10 mG will be presented.

Figure 2. D.c. signal offsets observed in the Fermilab prototype in 48 days of operation.

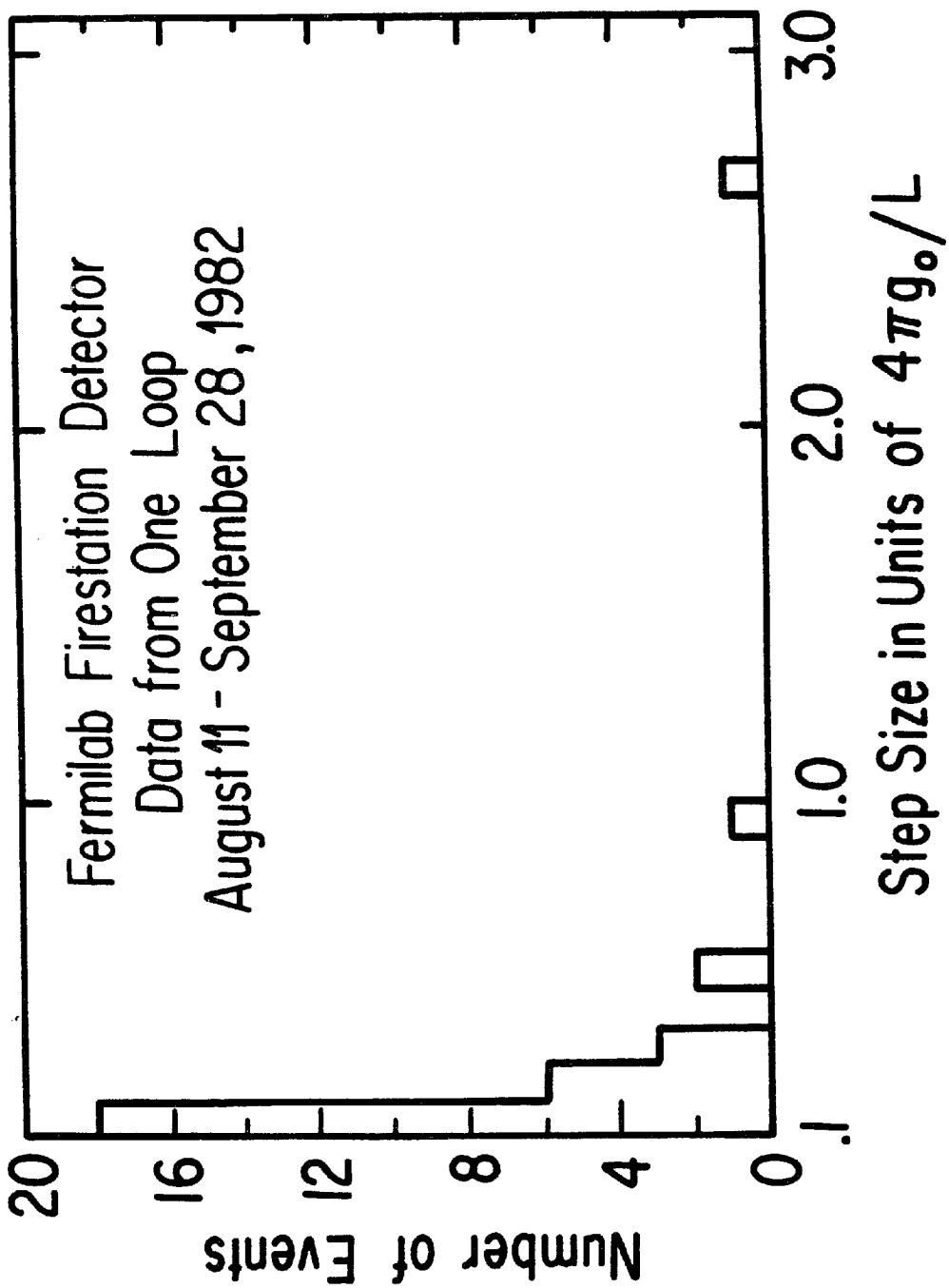

Figure 3. Event observed Labor Day, 1982. On Labor Day, 1982, the Fermilab prototype exhibited this offset of 21 mV which is consistent with the signal expected for a single Dirac-charge monopole. Tests indicated that offsets of this kind could be caused by environmental disturbances.

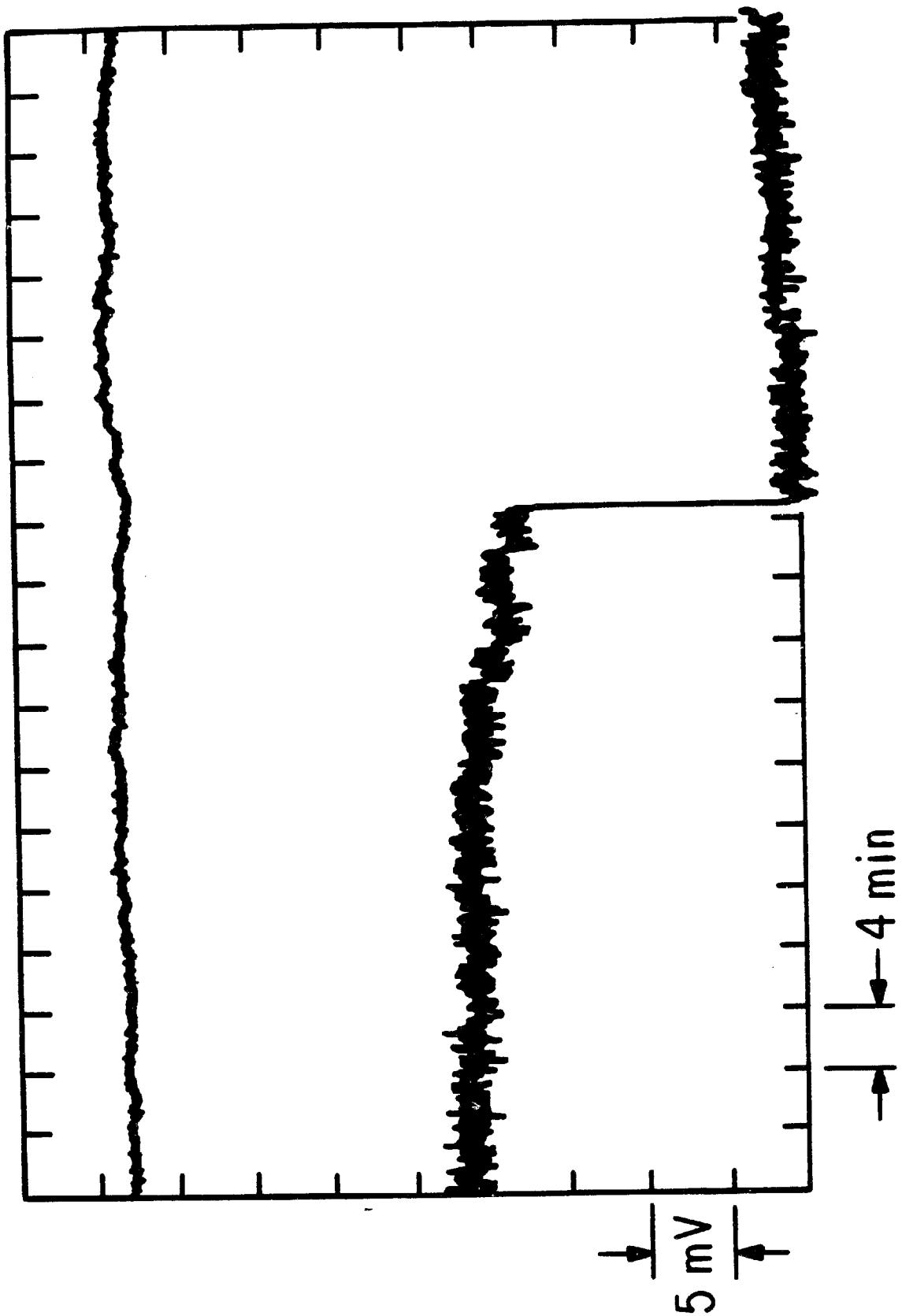

In addition to the constraint of ultra-low field operation, the first induction detectors[57,58] were limited to small areas by shield-loop inductive coupling. To understand this effect, consider what occurs when a monopole passes through a detector comprised of a circular loop completely enclosed by a cylindrical superconducting shield. The monopole induces currents in both the shield and the loop. The shield currents produce a magnetic flux which impinges upon the detector loop to induce a current in opposition to the current induced in the loop by the monopole. The net effect of the shield is therefore to reduce the current in the loop to some fraction of the maximum value that would occur in the absence of coupling. For a monopole traveling along the axis of a cylinder having radius B and half-height H, the fraction of signal is:[62]

$$F(z/B,R/B,H/B) = 1-\left[\left(\frac{R}{B}\right)^2+2\left(\frac{R}{B}\right)\sum_{n=1}^{\infty}\frac{\cosh(x_{1n}z/B))\ J_1(x_{1n}(R/B))}{x_{1n}\cosh(x_{1n}(H/B))\ [J_o(x_{1n})]^2}\right] \quad (2.1)$$

where z is the position of a loop of radius R inside the shield. Here $J_m(x)$ is the ordinary Bessel function of order m and x_{1n} is the nth root of $J_1(x)$. A plot of F for various values of the aspect ratios H/B and R/B at z = 0, (the loop midway between endcaps), is shown in figure 4. The signal diminishes as the loop diameter is increased relative to the shield diameter. As R/B approaches unity, F becomes negligible.

We solved this problem, as have other groups,[63,64] by twisting the detector loop into a gradiometer pattern of cells with alternating polarities. For such a loop the field generated by shield currents

will induce opposing currents in cells of opposite polarity. The monopole however will not induce opposing currents because it passes through a single cell and consequently its direct interaction with the gradiometer yields an induced current whose magnitude is the same for all monopole trajectories. The effect of the field generated by shield currents does, however, depend upon the monopole's specific trajectory since this determines the positions of the vortex currents in the shield. The trajectory dependence of the shield-loop coupling thus leads to a spreading out of the possible signal sizes expected for a monopole. The spread can be reduced by using gradiometers with finer cell grids but as the number of cells is increased the self inductance of the gradiometer increases and so the maximum signal size decreases.

Gradiometers are not new. Undoubtedly the first gradiometer was used by Ampere[65] in 1826 to cancel the effects of geomagnetic fields. His gradiometer consisted of equal area rectangular cells of opposite polarities and was called an "Astatic Pair."

The effectiveness of a gradiometer pattern depends upon how well-suited it is for a chosen shield geometry. We considered a cylindrical shield with H/B ~ 0.3 because we were interested in eventually constructing a large planar detector consisting of an array of gradiometers. The volume, and hence the cost, of such an array increases with increasing H/B. In figure 4 we see that for H/B ~ 0.3, a coupling loss of ~10%, (F = 0.9), corresponds to R/B ~ 0.1. From this fact we deduced that a gradiometer with many equal square

Figure 4. Fraction F of signal for various loop and shield sizes. The loop radius is R, and the cylindrical shield has half-height H and radius B.

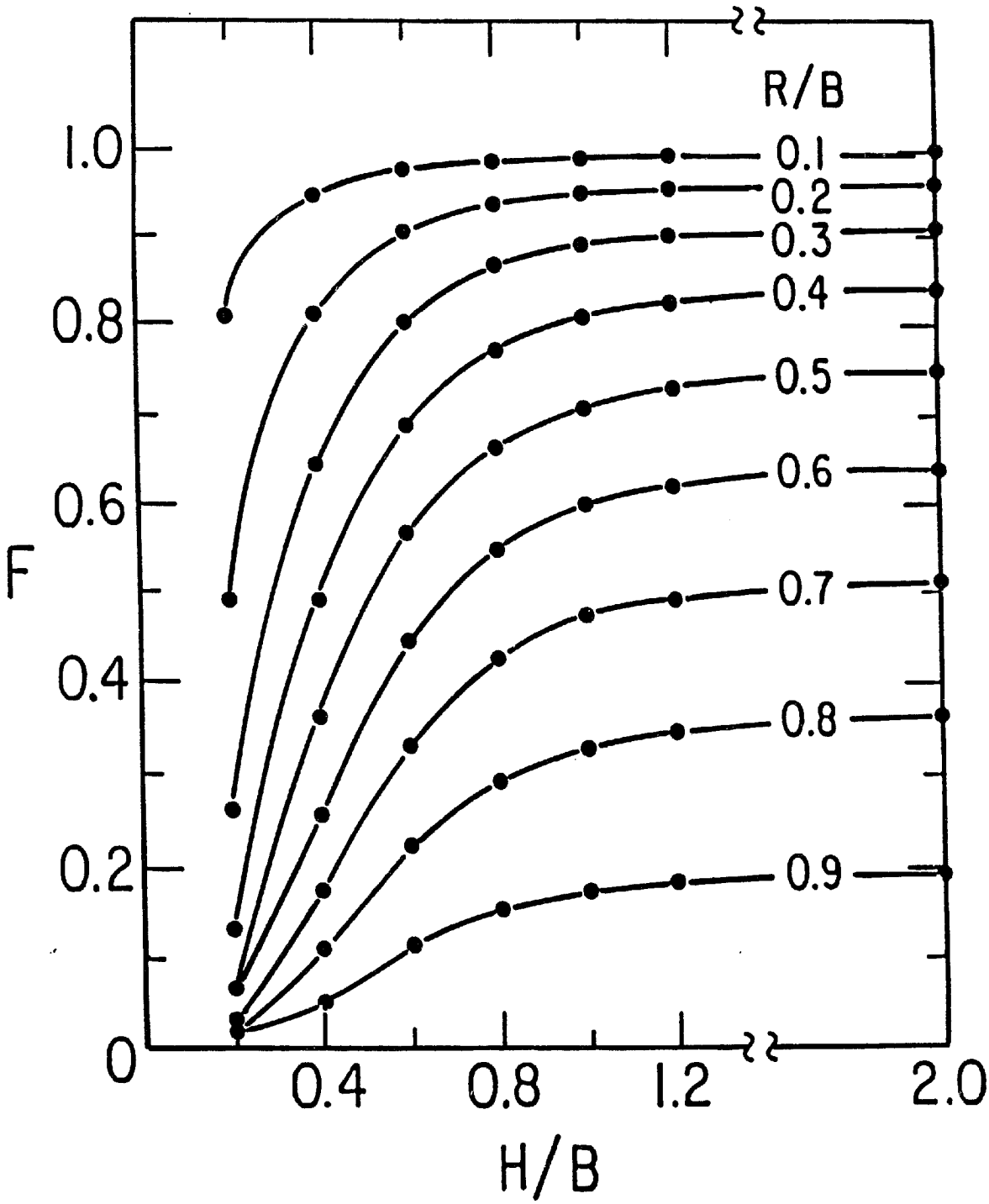

cells of dimension d ~ B/6 in a shield with H/B ~ 0.3 would have F $\gtrsim$ 0.9 for most possible monopole trajectories. This conclusion is based upon the fact that to first approximation, only the cell through which the monopole passes needs to be considered in a determination of shield-loop inductive coupling. The effects of the other cells cancel one another in this level of approximation. The problem therefore reduces to that of a simple loop for which F has already been calculated. A careful calculation of shield-loop coupling was later performed and indicated good agreement with the conclusions drawn from the simple intuitive model above.

Calculation of the Field in the Shield After the Passage of a Monopole

In order to determine the inductive coupling of the shield to the gradiometer it is necessary to determine the magnetic field produced by the vortex currents in the shield. If we assume, for the moment, that the region inside the superconducting shield is free of conducting materials, then, as will be shown below, the magnetic field can be derived from a scalar potential. The scalar potential, in turn, satisfies the Laplace equation with Neumann boundary conditions.[66]

Consider a monopole passing through the endcaps of the shield along an arbitrary trajectory as shown in figure 5. At the points P_1 and P_2 where the monopole trajectory intersects the shield, the strong local field of the monopole is sufficient to cause a phase transition to the normal metallic state in a mesoscopic region, which for Pb, is

about 3000 Å in diameter. All of the monopole's field lines are pulled through these regions and trapped there. The net flux change of $\Delta\Phi = 2\phi_o$, for a single Dirac-charge monopole, induces vortex supercurrents in the superconductor surrounding the normal regions. These maintain the flux through these areas as the monopole proceeds to infinity. In the shielded volume the trapped field becomes diluted as the lowest energy state is obtained. The field cannot penetrate through the shield; (except at the points P_1 and P_2), as a result of the perfect diamagnetism of the superconductor. Consequently, the net flux through any horizontal plane on the interior is $2\phi_o$. When the monopole has proceeded to infinity, the field lines outside the shield will have connected up between the points P_1 and P_2 to produce a dipole field as in figure 6.

The absence of a current density inside the shielded region means that the field in that region can be derived from a scalar potential, $V(\rho,\phi,z)$, satisfying the Laplace equation:

$$\nabla^2 V = 0$$

The normal component of the field derived from V must vanish at the shield surface as is appropriate for a superconductor. Thus:

$$\vec{\nabla} V \cdot \hat{n} = 0 \qquad (2.2)$$

everywhere on the boundary except in the vicinity of the points P_1 and P_2. In the normal regions surrounding these points there exists a nonzero normal field. This field may be assumed to be uniform. It is easy to show that in the limit where the dimensions of these regions

Figure 5. Shield geometry and monopole trajectory used in the calculation of the trapped field. The field is produced by vortex currents induced by the passing monopole where the trajectory intersects the shield.

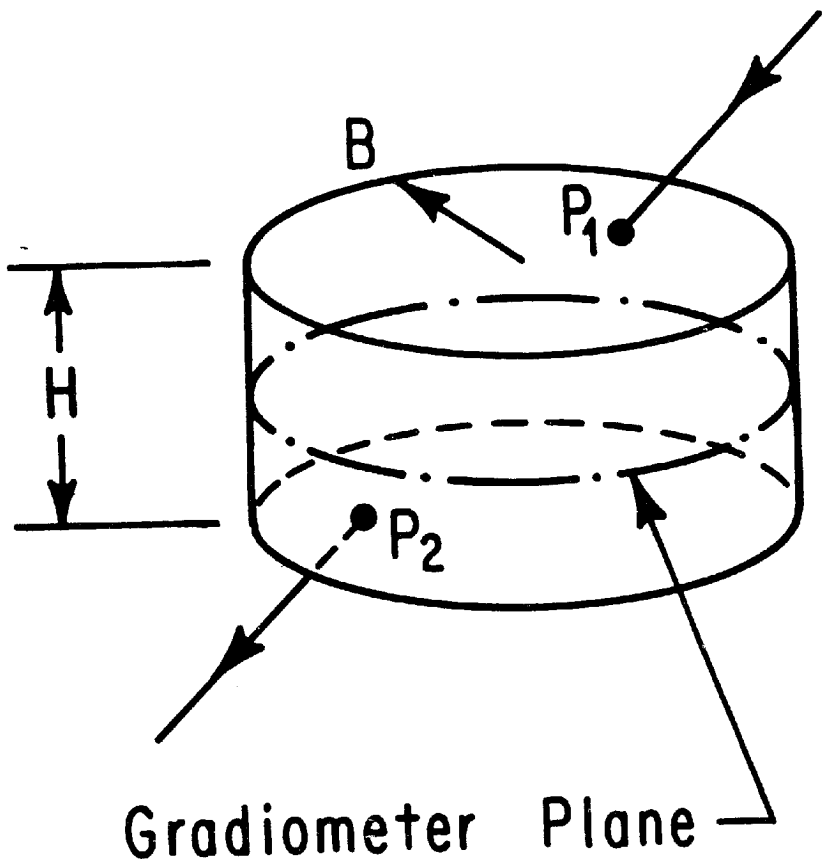

$$P_1 = (\rho_1, \phi_1, z_1)$$

$$P_2 = (\rho_2, \phi_2, z_2)$$

Figure 6. Dipole field trapped in shield after the passage of a monopole. The monopole travels along the dashed line trajectory shown.

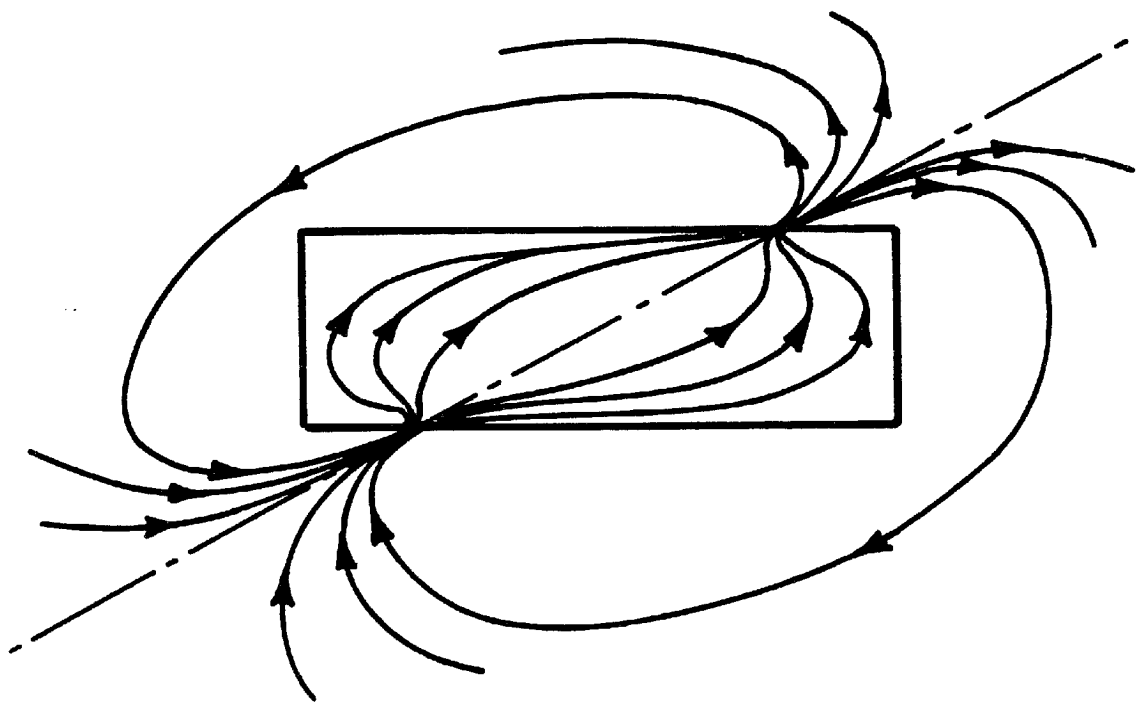

Figure 7. Shape of normal region used in the calculation of the field trapped in the shield. Eventually the limit $\epsilon \to 0$ is taken so that the shape of the region has no effect on the final result.

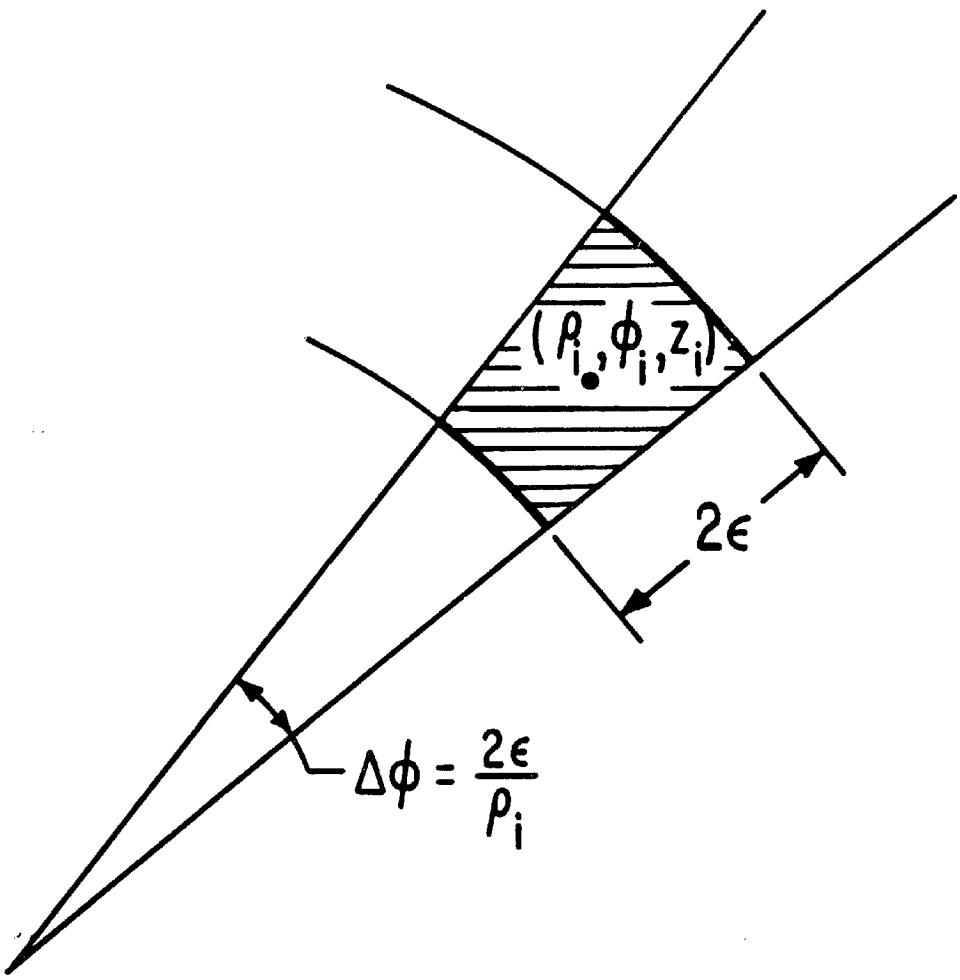

are vanishingly small compared to the dimensions of the shield, the shapes of these regions may be chosen arbitrarily. For simplicity, choose the curvilinear square shape seen in figure 7. For very small ϵ this region has an area of $4\epsilon^2$. If the uniform field has strength B_o then the flux is:

$$\Phi = 4\epsilon^2 B_o = 2\phi_o$$

So that:

$$B_o = \frac{\phi_o}{2\epsilon^2}$$

(Later we will take the limit as ϵ goes to zero, but for now we merely assume that $\epsilon/B << 1$.) The Boundary conditions for the endcaps of the shield have the following simple form:

$$-\frac{\partial V}{\partial z}(\rho, \phi, z = z_i) = \frac{\phi_o}{2\epsilon^2}\left[1 - \theta(|\rho - \rho_i| - \epsilon)\,\theta(\rho_i|\phi - \phi_i| - \epsilon)\right] \quad (2.3)$$

for i = 1,2; where $\theta(x)$ is the Heavyside function. The boundary condition for the cylinder walls is simply:

$$-\frac{\partial V}{\partial \rho}(\rho = B, \phi, z) = 0 \quad (2.4)$$

The most general solution of the Laplace equation which does not overtly contradict these boundary conditions may be written:

$$V(\rho, \phi, z) = -\frac{2\phi_o}{\pi B^2}\{ z + \quad (2.5)$$

$$\sum_{m=0}^{\infty}\sum_{n=1}^{\infty}\left[A_{mn}\cosh(k_{mn}z)+B_{mn}\sinh(k_{mn}z)\right]\left[E_{mn}\cos(m\phi)+F_{mn}\sin(m\phi)\right]J_m(k_{mn}\rho)\}$$

where the constant multiplying the expression in parentheses was chosen so that the total integrated flux through the shield is $2\phi_o$. In order to satisfy the radial boundary condition we must merely require that:

$$k_{mn} = \frac{\xi_{mn}}{B}$$

where:

$$\left[\frac{dJ_m(x)}{dx}\right]_{x = \xi_{mn}} = 0 \qquad (2.6)$$

From the endcap boundary conditions:

$$\left[-\frac{\partial V}{\partial z}\right]_{z=z_i} = \frac{2\phi_o}{\pi B^2}\left\{1+\left[\sum_{m=0}^{\infty}\sum_{n=1}^{\infty} k_{mn}\left[A_{mn}\sinh(k_{mn}z_i) + B_{mn}\cosh(k_{mn}z_i)\right]\right] \times \right.$$

$$\left. \left[E_{mn}\cos(m\phi) + F_{mn}\sin(m\phi)\right] J_m(k_{mn}\rho)\right\} \qquad (2.7)$$

$$= \frac{\phi_o}{2\epsilon^2}\left[1 - \theta(|\rho - \rho_i| - \epsilon)\,\theta(\rho_i|\phi - \phi_i| - \epsilon)\right]$$

To extract expressions for the coefficients; (A_{mn}, B_{mn}, ...), we exploit the orthogonality relations and the normalizations of the trigonometric and Bessel functions. Thus we multiply each side of expression (2.7) by:

$$\rho d\rho d\phi \sin(m'\phi)\, J_{m'}(k_{m'n}\rho)$$

and integrate over all ϕ and for ρ from 0 to B. To do this, the following integrals are used:

$$\int_0^{2\pi} d\phi \sin(m\phi)\sin(m'\phi) = \pi\delta_{mm'} \qquad (2.8)$$

$$\int_0^{2\pi} d\phi \, \sin m\phi \int_0^B d\rho\rho \, [\, 1 - \theta(|\rho - \rho_i| - \epsilon) \, \theta \, (\rho_i|\phi - \phi_i| - \epsilon)] \, J_m(k_{mn}\rho)$$

(2.9)

$$= 2\epsilon^2 \, J_m(k_{mn}\rho_i) \, \sin(m\phi_i)$$

(where in the last expression only the lowest order term in ϵ is retained), and the Bessel normalization:

$$\int_0^B d\rho\rho \, J_m \left(\frac{\xi_{mn}\rho}{B}\right) J_{m'} \left(\frac{\xi_{m'n}\rho}{B}\right) = \frac{B^2}{2} \left[\left(1 - \frac{m^2}{\xi_{mn}^2}\right) \left[J_m(\xi_{mn})\right]^2 \right] \delta_{mm'} \tag{2.10}$$

Finally one finds the expressions, (i = 1, 2):

$$\frac{2\phi_o}{\pi B^2} \left[A_{mn}\sinh(k_{mn}z_i) + B_{mn}\cosh(k_{mn}z_i)\right] F_{mn} \tag{2.11}$$

$$= \frac{2\phi_o}{\pi B^2} \, \frac{J_m(k_{mn}\rho_i) \, \sin(m\phi_i)}{k_{mn}\left(1 - \frac{m^2}{\xi_{mn}^2}\right) \left[J_m(\xi_{mn})\right]^2}$$

A similar calculation can be done in which the orthogonality of the $\cos(m\phi)$ functions is exploited. This results in the expressions, (i = 1, 2):

$$\frac{2\phi_o}{\pi B^2} \left(A_{mn} \sinh(k_{mn}z_i) + B_{mn}\cosh(k_{mn}z_i)\right) E_{mn} \tag{2.12}$$

$$= \frac{2\phi_o}{\pi B^2} \, \frac{J_m(k_{mn}\rho_i) \, \cos(m\phi_i)}{k_{mn}\left(1 - \frac{m^2}{\xi_{mn}^2}\right) \left[J_m(\xi_{mn})\right]^2}$$

We thus have four expressions which determine the coefficients uniquely. After some slightly tedious algebraic manipulations, the following products of coefficients can be found:

$$A_{mn}F_{mn} = \frac{\sigma_1 s_1 ch_2 - \sigma_2 s_2 ch_1}{sh_{12}}$$

$$A_{mn}E_{mn} = \frac{\sigma_1 c_1 ch_2 - \sigma_2 c_2 ch_1}{sh_{12}} \qquad (2.13)$$

$$B_{mn}F_{mn} = \frac{\sigma_2 s_2 sh_1 - \sigma_1 s_1 sh_2}{sh_{12}}$$

$$B_{mn}E_{mn} = \frac{\sigma_2 c_2 sh_1 - \sigma_1 c_1 sh_2}{sh_{12}}$$

where the following abbreviations have been used:

$$sh_i = \sinh(k_{mn}z_i),\ ch_i = \cosh(k_{mn}z_i),\ c_i = \cos m\phi_i,$$

$$s_i = \sin(m\phi_i),\ sh_{12} = \sinh[k_{mn}(z_1 - z_2)],\ \text{and}$$

$$\sigma_i = \frac{J_m(k_{mn}\rho_i)}{k_{mn}\left[1 - \frac{m^2}{\xi_{mn}^2}\right]\left[J_m(\xi_{mn})\right]^2} \qquad (2.14)$$

Substituting expressions (2.13) for the coefficients into expression (2.5) for the scalar potential and reducing to the most symmetric form we obtain:

$$V(\rho,\phi,z) = \frac{-2\phi_o}{\pi B^2}\left\{ z + \sum_{m=0}^{\infty}\sum_{n=1}^{\infty} (1 - \delta_{m0}\delta_{n1})\, J_m(k_{mn}\rho) \times \right. \tag{2.15}$$

$$\left. \frac{\left[J_m(k_{mn}\rho_1)\cos[m(\phi-\phi_1)]\cosh[k_{mn}(z-z_2)] - J_m(k_{mn}\rho_2)\cos[m(\phi-\phi_2)]\cosh[k_{mn}(z-z_1)]\right]}{k_{mn}\left(1 - \frac{m^2}{\xi_{mn}^2}\right)\left[J_m(\xi_{mn})\right]^2 \sinh[k_{mn}(z_1 - z_2)]} \right\}$$

Having calculated the scalar potential we can now determine the magnetic field components inside the shielded volume by differentiation. We are interested in how this field couples to a gradiometer conducting loop lying inside the shield in some plane z = constant. In general, the coupling is not simple and the current loop on the interior can produce image currents in the shield which will distort the field from that given by expression (2.15). However, if we assume that the gradiometer is well-suited to the shield geometry for arbitrary magnetic monopole trajectories, then we know that the shield-loop coupling will be small. In this case, the effect of the image currents will be too small to contribute appreciably to the field. Under the assumption that a proposed gradiometer pattern is suitable, we can thus proceed to calculate shield-loop couplings using equation (2.15). If these turn out to be large then we know that equation (2.15) is not a correct representation of the field and must either be replaced or a different gradiometer pattern must be used.

Determination of the Response Function

In order to calculate the signal size for a particular monopole trajectory we first integrate the normal component of the magnetic

field produced by shield currents over the plane of the gradiometer with care taken to multiply the integrand by the local polarity, (±1), of the gradiometer cell. This gives the net flux Φ' impinging on the gradiometer. Thus for a gradiometer in a plane parallel to the xy plane at $z = x_3^o$ and with cell polarities as a function of position in the plane given by $p(\rho,\phi)$, we calculate:

$$\Phi' = - \int \rho d\rho d\phi \; p(\rho,\phi) \left[\frac{\partial V}{\partial z} \right]_{z = x_3^o} \tag{2.16}$$

where the integration extends over the surface of the gradiometer. The signal for this trajectory is proportional to the absolute value of the monopole flux less the absolute value of Φ':

$$|\text{signal}| \sim 2\phi_o - |\Phi'| \tag{2.17}$$

The maximum signal corresponds to no coupling, ($\Phi' = 0$), and so (2.17) corresponds to a fraction of the maximum signal given by:

$$F(P_1, P_2) = \frac{2\phi_o - |\Phi'|}{2\phi_o} = 1 - \frac{|\Phi'|}{2\phi_o} \tag{2.18}$$

where we write $F = F(P_1, P_2)$ in order to indicate the dependence upon the trajectory of the monopole and the positions, P_1 and P_2, of the vortex currents.

For a given gradiometer loop inside of a particular superconducting shield, it is important to know the distribution of possible signal sizes and their associated probabilities. This information is contained in the response function of the detector which gives the probability for a monopole event to have a particular signal size.

To calculate the overall response function of a particular shield-loop system, many different monopole events are generated by a numerical simulation, (Monte Carlo) under the assumption of a uniform, isotropic flux. For each simulated event, $F(P_1, P_2)$ is calculated as a real number between 0 and 1. The response function is then a histogram of the number of events versus F. The histogram is normalized to unity by dividing the number of events in each bin by the total number of events generated. In this way the histogram can be interpreted as a probability distribution.

Response Functions Calculated for CFM I

Our first large area detector, (CFM I: Chicago-Fermilab-Michigan I); uses cylindrical shields with spherically-domed endcaps. The formula for the field, equation (2.15), inside a cylindrical shield with flat endcaps is used to approximate the field in the true shield geometry by choosing P_1 and P_2 to correspond to the positions at which the trajectory would intersect the domed endcaps. The position of the gradiometer remains fixed at $z = 0$. In figure 8 the approximate and true geometries for several trajectories are compared schematically.

The shields have an inside diameter of 60.5 cm and an interior height which varies from 9.5 cm at the edge to 19.0 cm along the cylinder axis. We use a gradiometer which is 60.0 cm in diameter in order to fill up essentially all of the available area. Based upon our earlier gradiometer design considerations, we decided to use a

square-cell gradiometer pattern with cell size d = 5 cm. The cells were intended to alternate in polarity along both x and y coordinate directions as in figure 9a. However, a mistake was made in the layout of the pattern with the result that the polarities alternated along only the y-direction, as in figure 9b.

To determine the response functions for each of these patterns we generated 3000 random monopole trajectories under the assumption of a uniform and isotropic flux. The numerical calculation of the signal fraction and the method of trajectory generation are discussed in appendix A. For each trajectory the integral in equation (2.16) was evaluated as a sum over 1000 points in the plane of the gradiometer. Calculation of the field, (using equation (2.15), i.e., $-\partial V/\partial z$), included 43 terms in the sums over m and n and we found that there was essentially no contribution to the error from this part of the calculation (see appendix A). In order to achieve this accuracy for so many field points without requiring too much computational time, many timesaving methods were employed (see appendix A). Even so, the calculation of F for each trajectory required about 1.5 minutes on a Harris 100, (approximately a VAX 780 equivalent) and the calculation of the response functions required a little more than three days of CPU time. The response functions for the two gradiometer patterns were calculated simultaneously by using the same trajectories and calculated field values but different polarity functions, $p(\rho, \phi)$, in equation (2.16). An integration over a simple loop, ($p(\rho, \phi) = 1$ for all ρ and ϕ), was also done to check that the total flux was near to

Figure 8. True and simplified geometries for field calculations. For trajectories through the shields, as shown on the left-hand side, the calculation of the signal was performed using cylinders with flat endcaps as shown on the right-hand side. The dashed line represents the position of the gradiometer plane. Note that the vertical positions of the endcaps on the right-hand side correspond to the vertical positions where the monopole intersects the shield in the true geometry. Both trajectories through (a) the sides and (b) the endcaps are approximated by this method.

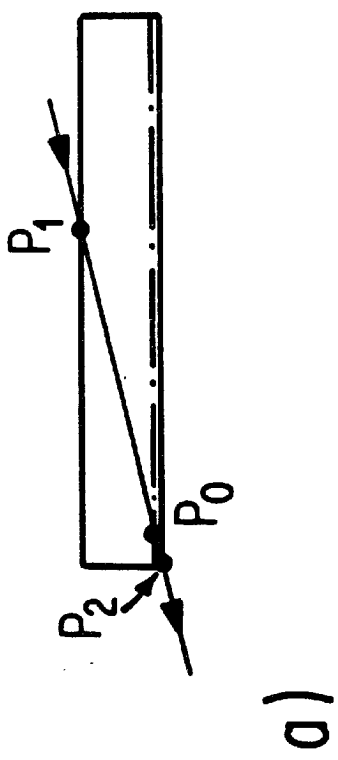

(a)

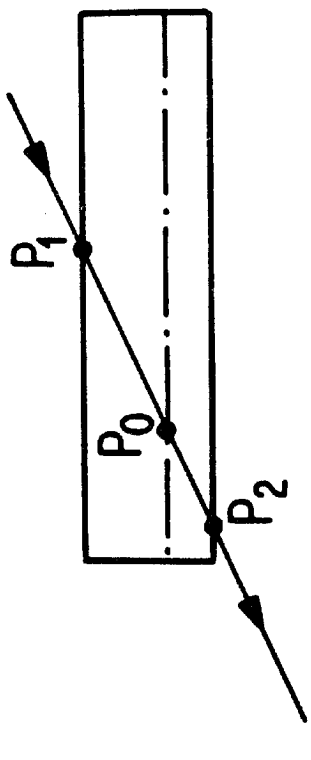

(b)

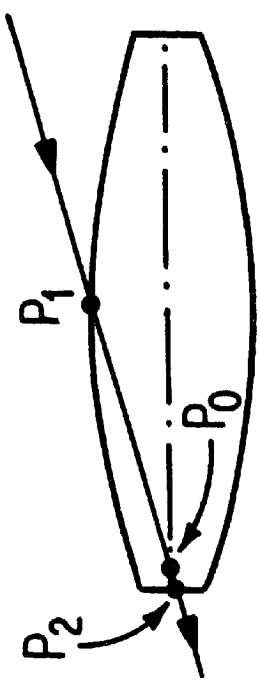

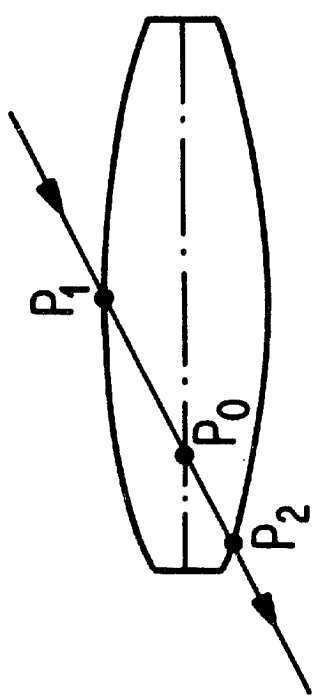

Figure 9. Intended and actual gradiometer patterns. (a) The intended square-cell gradiometer and (b) the strip-cell gradiometer pattern actually used in the experiment. Black and white regions have opposite polarity.

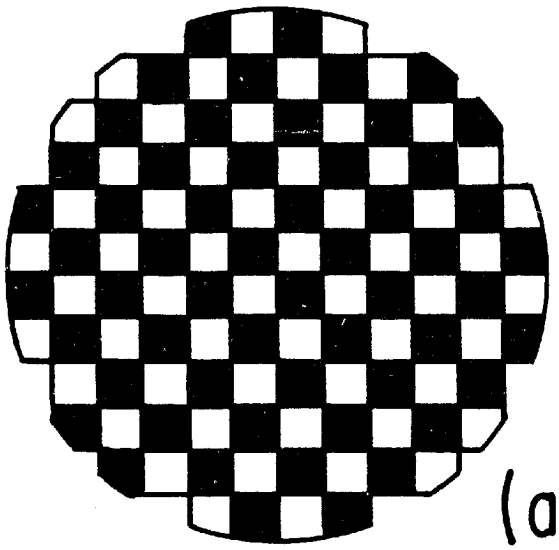

(a)

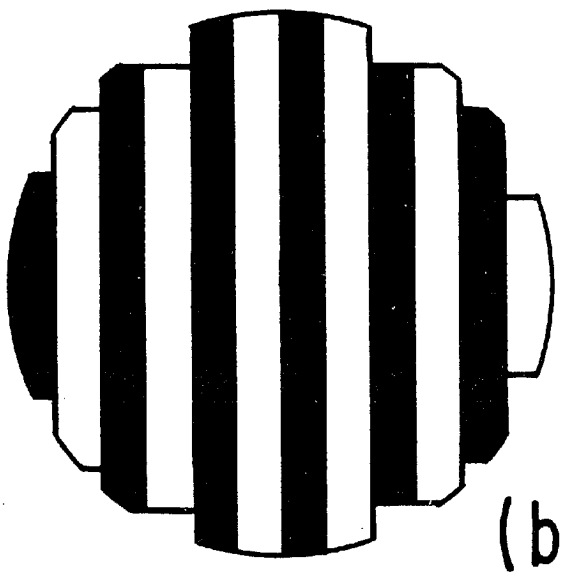

(b)

the total flux $2\phi_o$ as expected. (Because the loop diameters are 60 cm while the shield diameter is 60.5 cm some flux will not impinge upon the loop and so the total flux will be less than the maximum of $2\phi_o$.)

The response functions for the two patterns are shown in figures 10 and 11. Except for a long tail extending into the region of small signal size, we find, (to our relief) that the strip-cell gradiometer is comparable to the square-cell gradiometer.

Calibrating the Detector

The calculation of the response function as described above is straightforward yet very complicated. Consequently we would like to have some way of testing it. In particular we would like to be able to simulate monopole events in our detector and determine to what degree the induced signal depends both upon the flux of the monopole and the coupling of the shield to the gradiometer. The current induced in the loop will also depend upon the loop inductance. The maximum current, (corresponding to no shield-loop coupling), can in fact be completely determined when the self-inductance of the gradiometer is known. We discovered, however, that it is possible to simulate a monopole event in its entirety, (including vortex currents induced in the shields), by means of a long slender solenoid to which we have given the name of "pseudopole." Thus we do not rely solely upon loop self-inductance measurements as a means of calibration.

The success of a pseudopole relies upon the fact that it allows one to change magnetic flux in a region with very small cross-

sectional area. In our detectors the pseudopoles pass not only through a cell of the gradiometer but also through both endcaps of the shield, (see figure 12). When a d.c. current is stimulated in the windings of the pseudopole there is induced a corresponding core flux. The superconductor must react to this core flux with the production of a surface current density in order to produce a flux that will exactly cancel it. This argument applies to both the gradiometer and the shield. The currents induced on the inside surface of the shield are vortex currents surrounding a non-superconducting hole. This is very similar to the state of affairs in the case of a real monopole event except for the fact that the normal region now has a diameter of 3 mm rather than 3000Å. Nevertheless, because this diameter is still very small compared to the dimensions of the detector, the vortex currents will produce a field at the gradiometer loop which is indistinguishable from that due to monopole-induced vortex currents. We conclude therefore that except for the magnetic flux in the pseudopole, the currents and fields everywhere inside the shielded volume are identical to those that would be produced by a magnetic monopole passing through the system along the line occupied by the solenoid axis.

We tested our pseudopole idea on a small prototype detector at Fermilab by placing a pseudopole along the axis of a closed cylindrical shield with flat endcaps as shown in figure 13. Inside the shield we placed a simple circular detector loop which lay in a plane midway between the endcaps, ($z = 0$). From the plots in figure 4

Figure 10. The response function for the gradiometer used in CFM I.

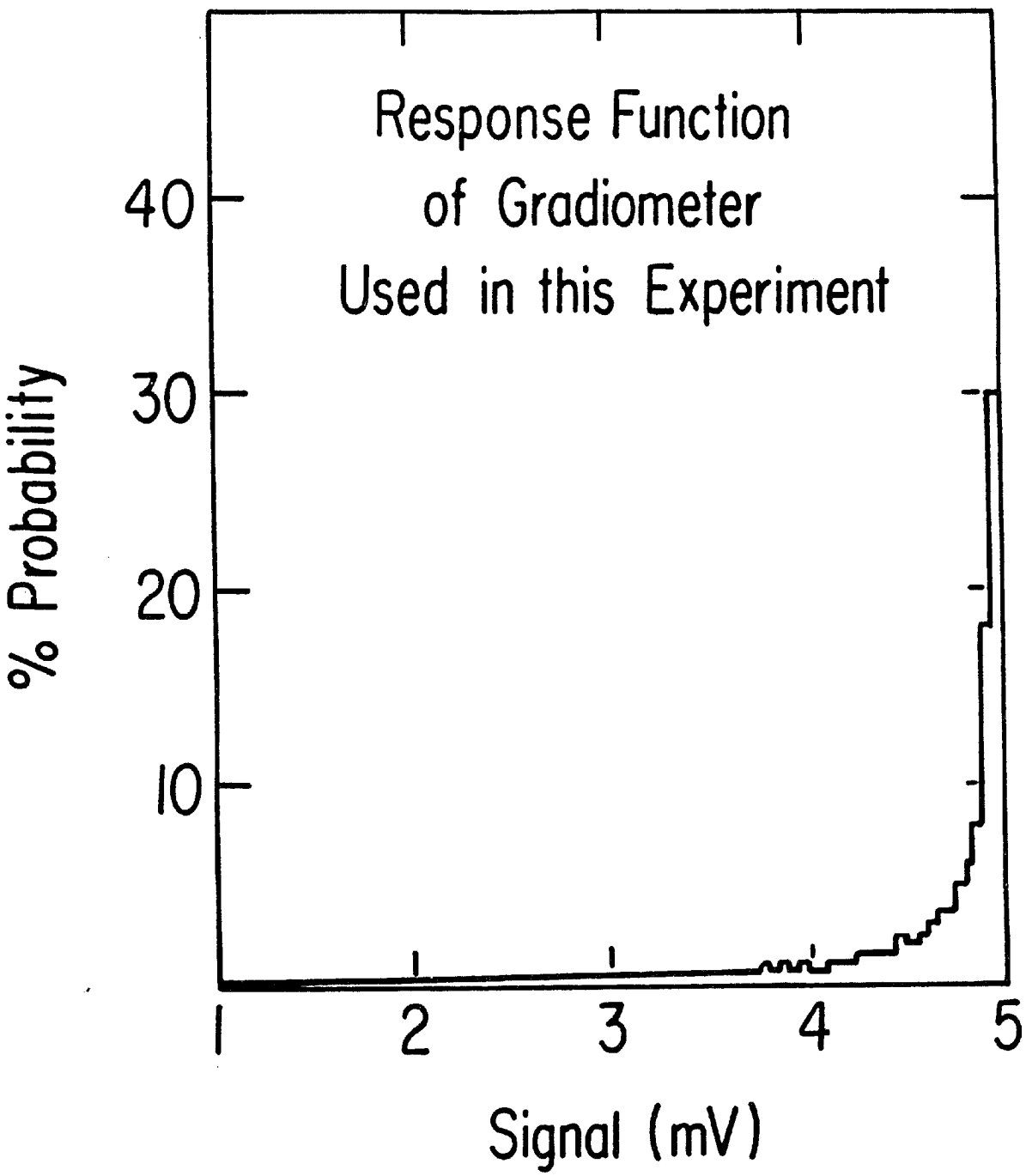

Figure 11. The response function for the gradiometer intended for CFM I.

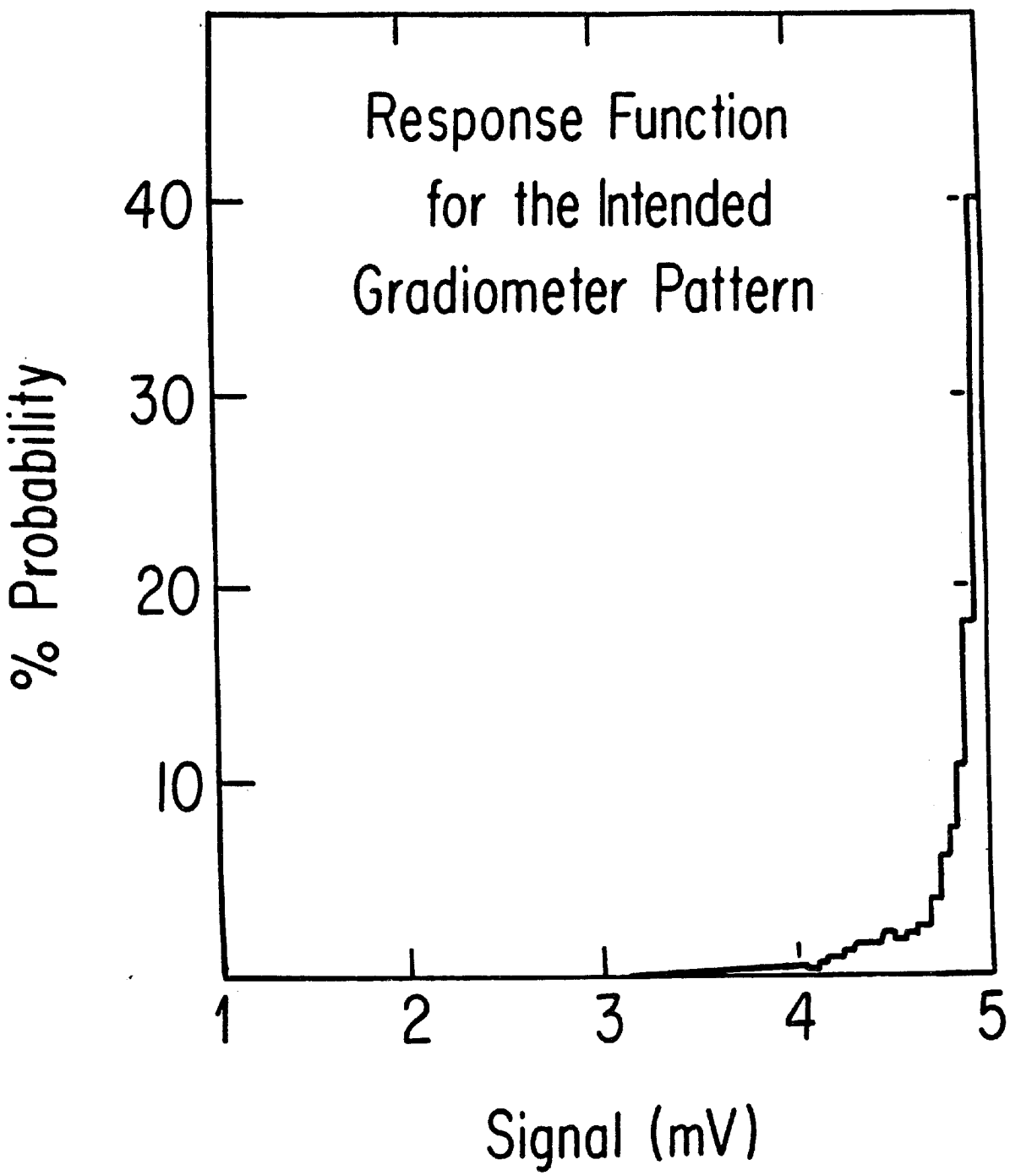

Figure 12. Pseudopole penetrating shield. This cut-away view shows the manner in which the pseudopole penetrates the shield.

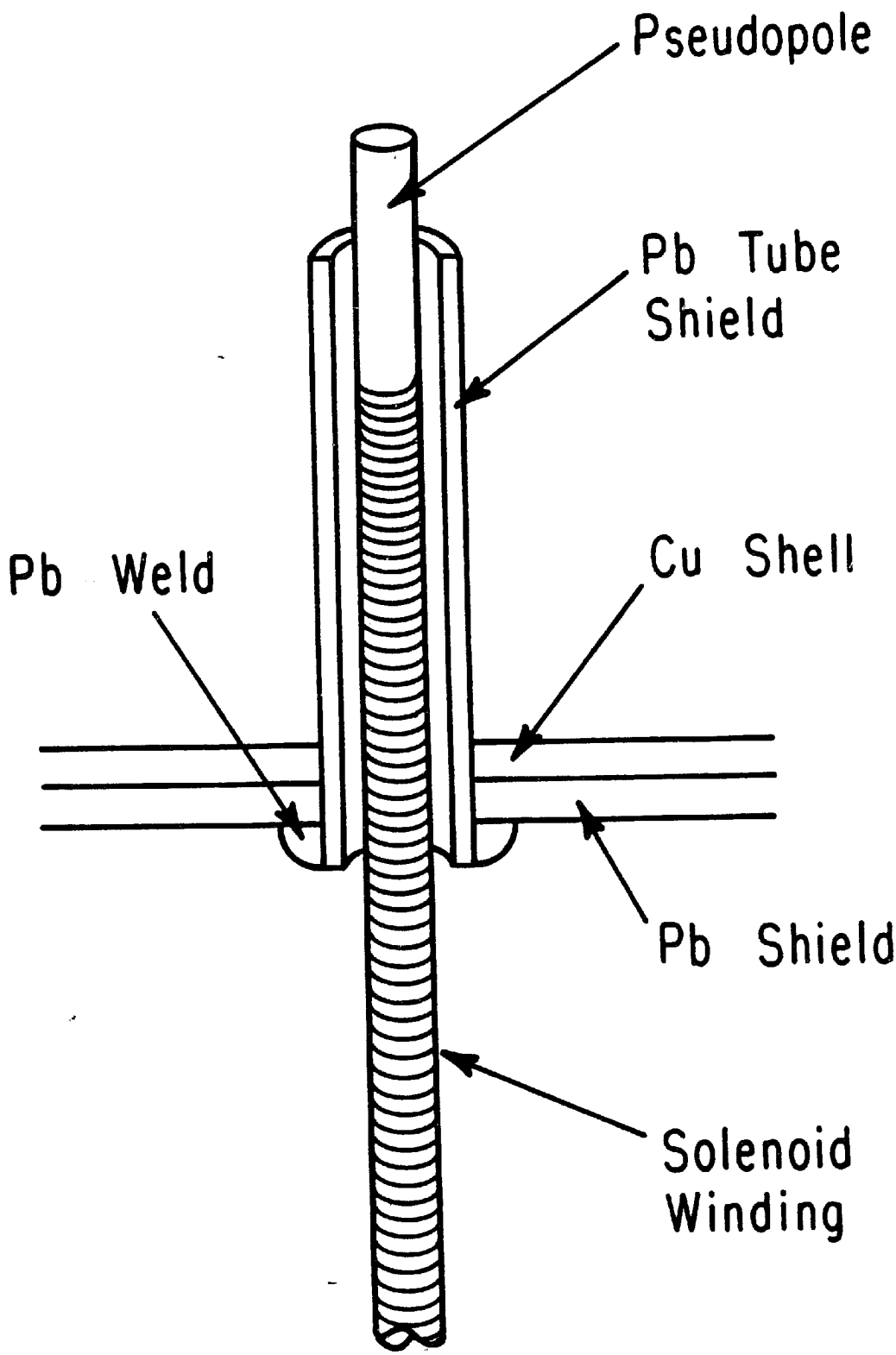

Figure 13. Apparatus used to test the calibration technique and the field calculation.

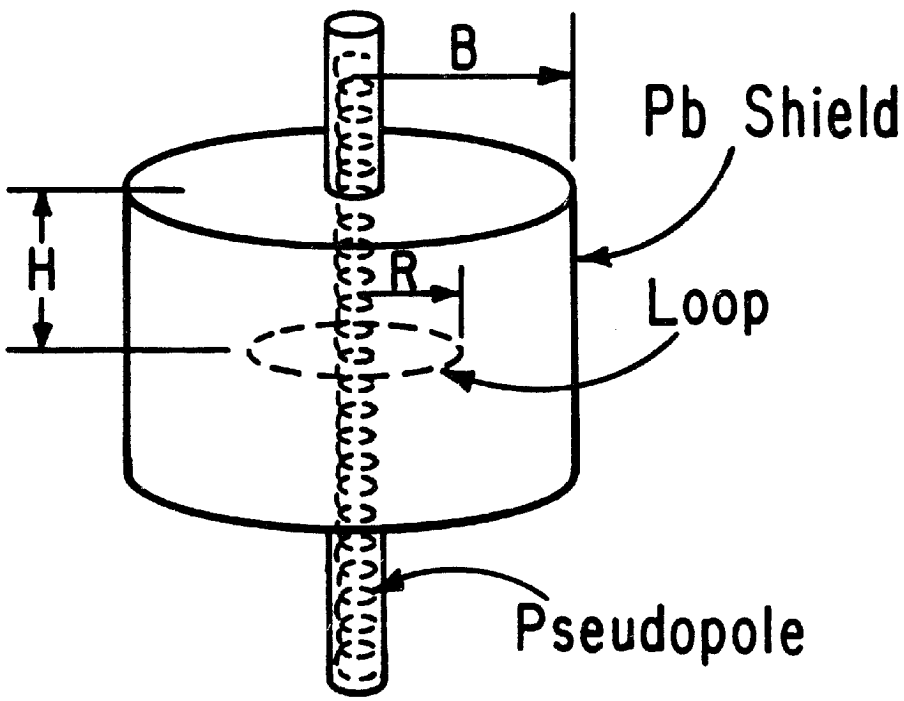

R, B, and H

and equation (2.1) with H/B = R/B = 1/3 we expect to measure a signal which is a fraction F = .875 of maximum, (where maximum signal is determined by the self-inductance of the loop). In our test, the stimulation of the pseudopole produced a signal which was a fraction F=.87 of maximum, in very good agreement with our expectations.

CHAPTER III

AN EXPERIMENT TO MEASURE THE MONOPOLE FLUX

In autumn of 1982 we began the design and construction of a detector which takes into account the considerations presented in the last chapter. Most notably this detector incorporates gradiometer detection loops which are isolated from the environment and from one another. In this chapter I describe the apparatus and discuss its performance. Although there were design flaws, (as would be expected for a new kind of detector), these were not serious enough to disallow a measurement of the monopole flux, (chapter IV). A second generation detector in which many of these flaws are corrected will be discussed in chapter V.

An Overview of the Apparatus

The apparatus, (see figure 14) consists of two independently isolated and shielded gradiometers suspended in vacuum and cooled by conduction. The superconducting shields are cylindrical with a diameter of 60.5 cm and have spherically-domed endcaps. They are positioned as near to one another as possible in order to obtain the greatest coincident acceptance of the two gradiometer detection loops. The latter are 60-cm in diameter and thus occupy essentially all of the available area inside the shield. The separation between the gradiometers is 21.0 cm.

Figure 14. The CFM I Apparatus. 1) Gradiometer plane, 2) Cu-covered superconducting Pb shield, 3) 4°K radiation and magnetic field shield, 4) 78°K radiation shield, 5) LHe reservoir, 6) SQUID tube and signal leads, 7) 78°K heat pick-off shroud, 8) top segment of two-part LN reservoir, 9) LHe transfer tube, 10) vent for LN reservoir, 11) SQUID rf head, 12) LN fill line, 13) ion gauge to measure vacuum pressure, 14) accelerometer, 15) vibration damping mount, 16) bottom segment of LN reservoir, 17) Aluminum vacuum vessel, 18) Cu braids for conduction cooling, 19) G-10 support rods, 20) Carbon thermometers, 21) pseudopole, 22) vacuum feedthru for bringing signal current to SQUIDs, 23) superinsulation, 24) Cu braid, 25) transformer inside shielded volume.

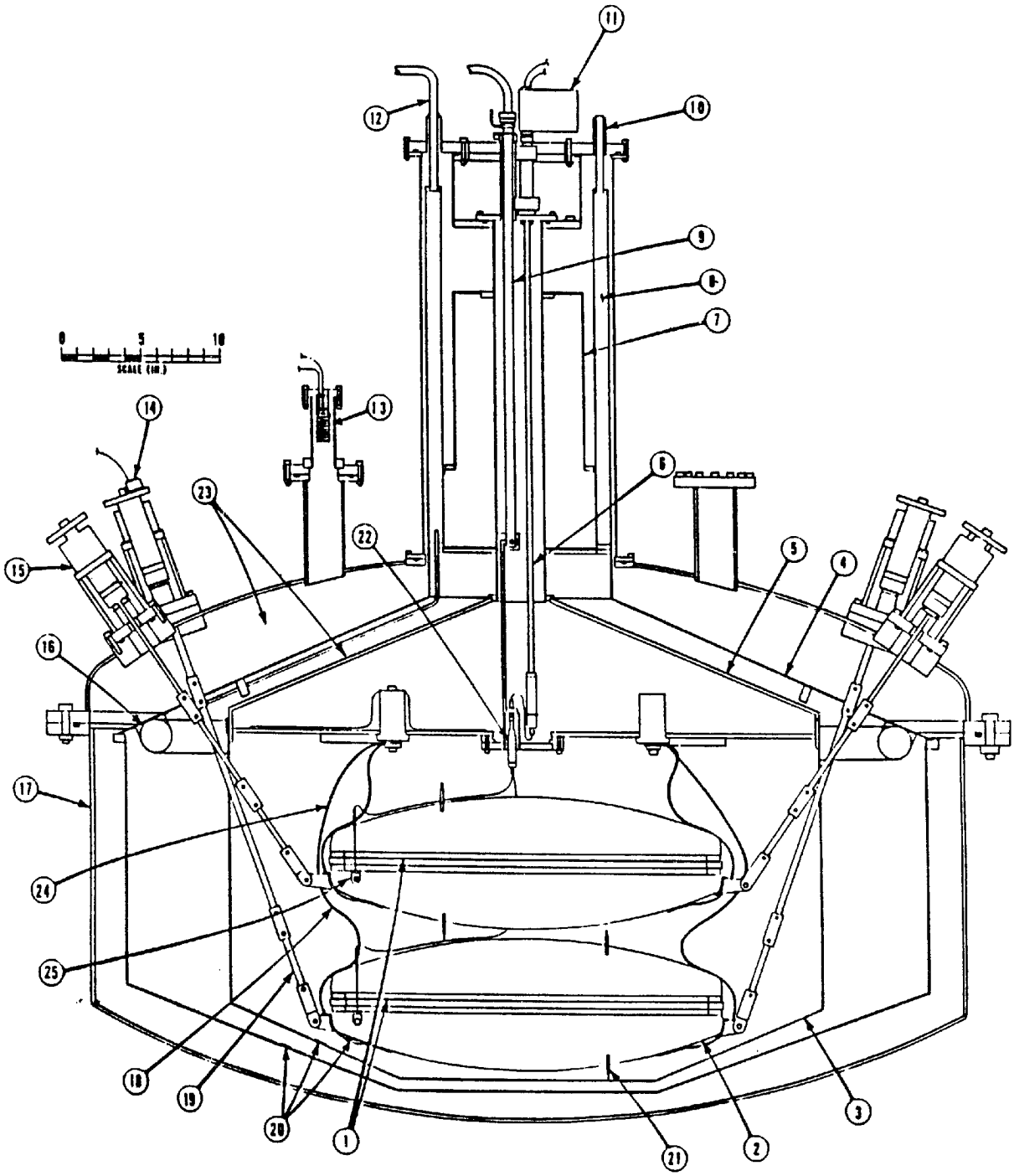

The detector loops and their superconducting shields are surrounded by thermal radiation and magnetic field shields. The radiation shields are cylindrical with diameters of 94 cm and 123 cm and are maintained at nominal temperatures of 4.2° K and 78° K respectively. The vacuum vessel is also cylindrical with a diameter of 138 cm and a volume of ~900 l. A 70 l liquid helium, (LHe), reservoir and a 30 l two-part liquid nitrogen, (LN), reservoir are also contained inside the volume. The vessel is surrounded by a 183-cm-diameter steel pipe which crudely shields the detector from the earth's magnetic field.

Gradiometers and Superconducting Shields

The gradiometers are fabricated as conventional solder-plated circuit boards in which standard 60-40 solder is used as the superconducting filament. We chose this simple technique in the interest of prototyping for a large detector array. It has the advantage of eliminating some of the vibrational motion that can be encountered with wire. To further inhibit vibration, each gradiometer is strapped and greased, (with low vapor pressure grease) to a 1.0-cm-thick G-10 disk. Additional stiffness is obtained by clamping the gradiometer and support disk between G-10 loops at the perimeter. The gradiometer and support plane have holes cut in them, (figure 15), to reduce their mass and thus to permit a more economical cooldown. The G-10 infrastructure of the detector is tightly fit into Pb shields. The shields were formed by pouring molten Pb into Cu dishes which, in turn, were formed by a cold-spinning process.[69] A plaster mold was

used to assure that a fairly uniform Pb thickness could be achieved. In actuality the thickness varies between 3 and 6 mm. To complete the construction of the shielded loops, a gradiometer and G-10 support structure is fitted into one Pb-lined Cu dish and covered by a second. The Pb linings overlap along the circle of intersection of the two halves. A welding joint is then made with Pb to obtain a single, contiguous superconducting shield. The integrated coefficients of thermal contraction for Pb and G-10 from 300° to 4.2° K are .0073 cm-per-cm and .0014 cm-per-cm, respectively. Consequently when the detector is cooled the Pb shrinks tightly around the G-10. This inhibits motion of the gradiometer relative to the shield.

The dome-shape of the endcaps is chosen to provide mechanical stability while the Cu shell makes it possible to cool the Pb and G-10 interior rapidly and uniformly. Due to the endcap geometry, the internal height of the shield varies from 19.0 cm along the central axis to 9.5 cm at the side wall. The average height is thus ~15 cm. In reference to the discussion of chapter II and figure 4, we have H/B=0.25 and therefore need a square-cell gradiometer to have cell size d = 5 cm, (d/B ~ .08), to achieve less than 10% coupling to the shield for the majority of possible monopole trajectories. We estimated that the gradiometer could have a self-inductance of up to ~50 μH before the signal-to-noise ratio would become intolerably low, (this will be discussed in more detail below). To roughly determine the self-inductances of various gradiometer patterns we hand-wound the patterns with Cu-wire and measured their impedances vs. frequency above ~100 kHz. At these frequencies resistive and capacitive

Figure 15. Gradiometer and support plane. This perspective view of the gradiometer circuit board and 1-cm thick G-10 support plane shows how the pattern occupies both sides of the circuit board. Holes are cut to reduce mass.

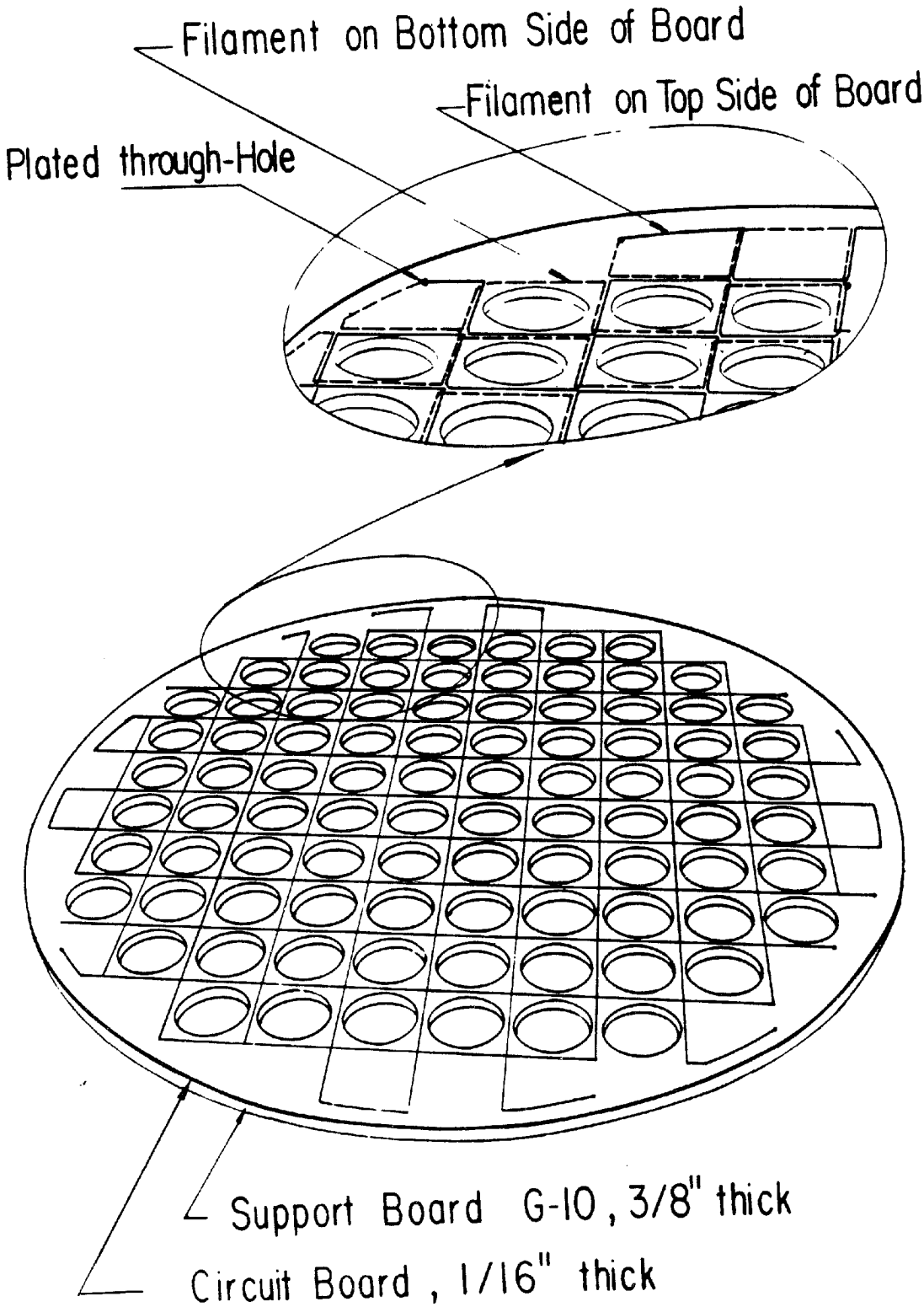

effects can be neglected and inductances can be measured fairly accurately (5-10%). A 60-cm-diameter gradiometer with 5-cm-square-cells and a filament diameter of ~1 mm was found to have an inductance of ~42 μH and was thus acceptable for use in the detector. We proceeded to lay out the pattern for manufacture as a solder-plated circuit board. The boards that were produced however were found to have self-inductances of ~21 μH. The unexpectedly low self-inductance was eventually understood to arise from a mistake in the board layout. As a consequence of this mistake the cells alternate in polarity along only one cartesian coordinate direction. This reduces the effective filament length by a factor of 2. (The self-inductance of gradiometers is approximately proportional to filament length, see figure 16.)

Impedance Matching Transformers and SQUIDs

Niobium wire-wound superconducting transformers are used to maximize the signals from the detector loops. These serve to impedance match the 21 μH detector loops to the 2 μH input inductance coils of the SQUIDs, (see figure 17). It can easily be shown that the passage of a monopole of charge g through a detector loop, coupled to a SQUID input coil by means of a transformer, will induce a current in the SQUID input coil given by:

$$i_{SQUID} = \frac{4\pi g\, K\sqrt{L_1 L_2}}{(L_2 + L_S)(L + L_1) - K^2\, L_1 L_2} \qquad (3.1)$$

where L is the inductance of the detector loop, L_s is the inductance of the SQUID coil, L_1 and L_2 are the primary and secondary inductances of the transformer, which has geometric coupling factor K. The maximum signal is obtained for the ideal case, (K=1), for $L_1 \rightarrow \infty$, $L_2 \rightarrow \infty$ and $L_1/L_2 \rightarrow L/L_S$. The current is then,

$$i_{SQUID} \rightarrow 2\pi g/\sqrt{LL_S} \qquad (3.2)$$

In the absence of a transformer, (i.e. direct coupling of the detector loop to the SQUID), the current is:

$$i^0_{SQUID} = \frac{4\pi g}{(L + L_S)} \qquad (3.3)$$

The signal thus falls more slowly with increasing L for an impedance matched circuit. (We later found that impedance matching can be achieved without a transformer[70] - see chapter V). The various parameter values for the transformers that were used in this experiment are listed in table 2. These values were measured while the transformers were superconducting.

The transformers are mounted directly to the gradiometers via G-10 platforms which elevate them 2 cm above the plane of the loops. Twisted-pair Nb leads from the transformers are shielded by 0.5-cm-diameter Pb tubes. The tubing connects to a shielded vacuum feed-through in a flange at the base of the LHe reservoir. The leads pass through the feed-through to the SQUIDs which are mounted inside the reservoir and immersed in LHe. Cu wire leads carry the signal from the SQUIDs and the 19 MHz rf biasing signals from the SQUID rf electronics mounted outside the cryostat. These leads are encased in

Figure 16. Inductance versus filament length of gradiometers with twelve square cells along the diameter. The inductance is linear in large filament lengths. For shorter filament lengths, nonlinear terms in the inductance are expected and so the curve is not expected to intersect the origin. The curve fits a functional form $L = \alpha\ell(\ell n(\ell/\beta)-\gamma)$ where α, β, and γ are constants and ℓ is the filament length. (This is precisely the form of the inductance of a circular loop.) The inductance goes to zero at $\ell \tilde{=} 2.0$ m which for the wire diameter used in these gradiometers, corresponds to the length of wire at which the cell spacing is zero.

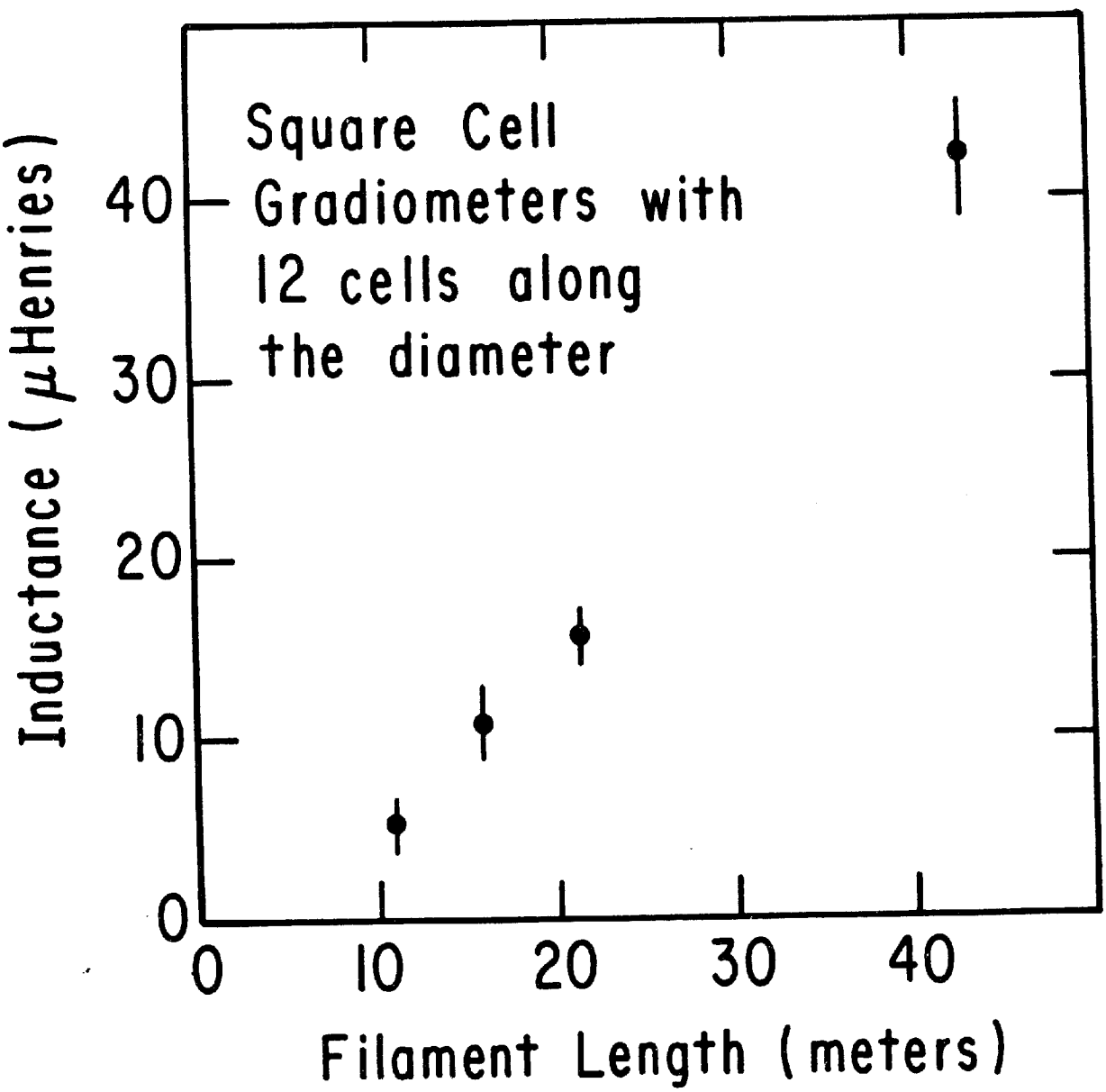

Figure 17. Detector circuit with transformer coupling. L_s is the input inductance of the SQUID and L is the inductance of the gradiometer.

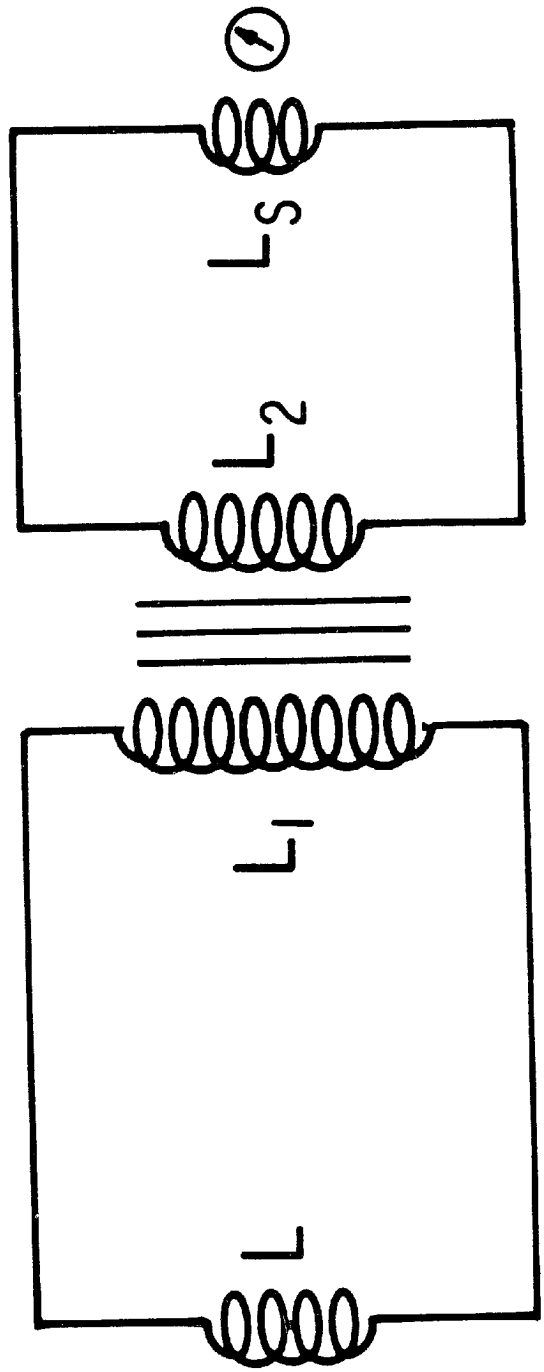

TABLE 2

MEASURED CONSTANTS OF THE SUPERCONDUCTING TRANSFORMERS

Transformer Constants	Symbol	Transformer 1	Transformer 2
Primary Inductance	L_1	52.1 μH	53.2 μH
Secondary Inductance	L_2	3.88 μH	3.59 μH
Mutual Inductance	M	13.07 μH	12.60 μH
Geometric Coupling Factor	K	.92	.91
Inductance Ratio	L_1/L_2	13.43	14.82

1.7-cm-diameter rigid stainless steel tubes having a wall thickness of 2 mm. The SQUID, rf electronics, read-out electronics, and signal lead tube just described are all part of the system purchased from BTI Corporation.[61] The tubes are cooled by cold helium vapor in the 67-cm-long, 7.5-cm-diameter stainless steel column of the LHe reservoir. They pass through the top of the column to the exterior of the apparatus by means of vapor-tight o-ring seals. Unfortunately the compression-type fittings used to capture the o-rings also serve to mechanically couple the SQUID tubes to the exterior shell of the vacuum vessel. This exposes the SQUIDs to mechanical disturbances and is in fact a source of spurious signals as will be discussed in more detail in chapter IV.

Pseudopoles

In each shielded volume, pseudopoles pierce the shield and gradiometer along paths parallel to the axis of the cylinder. The solenoids have 0.76-mm-diameter Cu cores and are wrapped in two layers of #39 magnet wire which has a diameter, (including insulation), of 0.12 mm. It follows that a current I will produce a core flux of

$$\Phi = \frac{\pi}{4}\,\mu_o I\,\left(\frac{1}{\delta}\right)\,\left[d^2 + (d + 2\delta)^2\right] \qquad \text{(MKS)} \quad (3.4)$$

where δ is the diameter of the wire, d is the diameter of the core and $\mu_o = 4\pi \times 10^{7}$ is the permeability of free space. The current sources for the pseudopoles were designed to allow two possible settings; $I_1 = 4.6 \times 10^{-7}$ A and $I_2 = 46.0 \times 10^{-7}$ A. From equation (3.4), these result in core fluxes of 6.0×10^{-15} Wb, ($\simeq 3\phi_o$ where $\phi_o = 2.07 \times 10^{-15}$ Wb is the quantum of flux) and 60.0×10^{-15} Wb, ($\sim 30\phi_o$).

The pseudopoles penetrate the superconducting Pb shields by means of long open-ended superconducting tubes, (figure 12). External magnetic fields can be shown to diminish in strength as ~exp(-1.8 z/a) with penetration into the tube,[59] (where z is depth measured from the end of the tube and a is the tube radius). For this experiment we chose the tube to have length $L \gtrsim 10a$ so that fields penetrating the tubes to the interior volume of the shields are reduced by at least 8 orders of magnitude.

All of the pseudopoles are aligned parallel to the axis of the cylindrical shields. The radial and azimuthal positions of the pseudopoles were chosen to give some indication of the response of the detector for arbitrary monopole trajectories. During the steady-state operation of the detector, the pseudopoles are stimulated remotely by computer for one minute intervals at the beginning and end of two-hour data files. In this way sensitivity and signal-size are regularly monitored.

Cryogenic System

The detector is operated in vacuum and cooled by conduction of heat to the LHe reservoir via flexible Cu braids. The braids are made up of ~1000 woven Cu wires to obtain a cross-sectional area of ~3.2 cm^2. (As a result of their flexible multi-wire construction, the conduction braids do not transmit very much vibration from the LHe reservoir to the detector.) To maintain the detector at ~4.2° K it must be shielded from 300° K thermal radiation. To this end it is completely surrounded by conducting surfaces maintained at 4.2° K and

78° K. The 78° K shield is made of Al and is cooled by means of contact with both segments of the two-part LN reservoir. The 4° K shield is made of Cu and is cooled by contact with the LHe reservoir. Each of the shields is also wrapped in many layers of ~.01-mm-thick wrinkled aluminized mylar sheet, ("superinsulation"). Adjacent layers of superinsulation are thermally insulated from one another by a layer of nylon mesh, ("bridal veil" - this is the real stuff worn by many a bride). For N layers of superinsulation between two planes fixed at temperatures T_1 and T_2 where $T_2 >> T_1$ it is easy to show that even when the aluminized mylar is treated like a black body, the radiation impinging upon the cold surface from the hot surface is reduced by a factor of (N + 1). When the reflectivity of the aluminum is considered this factor becomes much larger, (as much as several orders of magnitude depending upon how clean one maintains the reflecting surfaces). In this experiment the 78° K shield and 4.2° K shield have 35 and 6 layers of superinsulation respectively.

The vacuum must be maintained at low pressure to minimize heat transport by gases between surfaces at 300° K and those at 78° K or 4.2° K. Prior to filling the reservoirs with cryogenic fluids the vacuum is brought down as low as possible by means of a turbomolecular pumping system. The turbomolecular pump and its roughing pump are attached to the vacuum vessel by means of a 15 cm diameter transfer pipe. The transfer pipe connects to a 15 cm to 8 cm-diameter reducing fitting and 8 cm-diameter gate valve at the entrance port to the vacuum vessel. When the vacuum pressure has stopped decreasing, a molecular sieve is used to bring the room temperature pressure down further. The

sieve consists of thin Cu sheets, (~10 cm x 10 cm x 0.1 cm), which are covered in a layer of Zeolite chemical. The Zeolite, which is bonded to the Cu with glue, is a material with very high effective surface-area-to-volume ratio. Consequently it is very efficient at trapping gases -- particularly when maintained at low temperature. Eight zeolite encrusted Cu sheets are sandwiched together and bolted to the base of the LHe reservoir. Several 5 Watt manganin resistors are attached to the base of the stack for heating in order to accelerate outgassing of the Zeolite. Heating takes place while the turbomolecular pump is operated so that released gases are not recaptured by the molecular sieve. Once the majority of trapped gases have been exhausted by the Zeolite and removed by the turbomolecular pump the heaters are turned off. The pressure is then observed to fall rapidly to a new minimum as the Zeolite cools to room temperature. At this point the interior of the detector is cooled to 78° K and then 4.2° K with the introduction of LN and LHe respectively. Cryogenic pumping, (adsorption of gases by cold surfaces), will then dominate over the turbomolecular pump in pumping rate. Consequently the gate valve is closed to separate the vacuum volume from the pump which can then be turned off.

Vacuum pressure above ~1.0 millitorr is measured with a thermocouple gauge at the position of an auxiliary port. Below 1 millitorr a hot filament ion gauge is used with sensitivity to pressures as low as 10^{-11} torr, (which is substantially lower than the pressures -typically 10^{-7} torr- obtained for this experiment).

Temperatures in the 50-300° K range were measured with Cu wire-wound thermometers. The ten Cu thermometers used in this experiment were made by hand. Each consisted of ~100 m of #39 Cu wire to obtain a room temperature resistance of ~200 Ω. The wire was coiled and compressed into a single layer rectangular strip ~2.0 cm × 100 cm. The strips were bonded to metal surfaces in the apparatus with GE 7032 adhesive varnish. (This is a thermally conductive but electrically insulating material that maintains its adhesive grip at 4.2° K.) Temperatures in the 4.0-50° K range were measured by eight carbon resistors, each with nominal room temperature resistance of ~100Ω.

For both types of thermometer, accurate thermal measurements are obtained by exploiting the change of resistance of the material with temperature. Figures 18 and 19 show typical calibration curves for the two types of thermometer. Below ~50° K the temperature coefficient of electrical resistivity for Cu approaches unity so that the curve levels off and accurate temperature readings cannot be obtained. The temperature coefficient of electrical resistivity for C on the other hand is negative and grows rapidly below ~50° K. Note in figure 19 that near 4.2° K a change of 1° K in temperature corresponds to a change in resistivity of ~300Ω. If a resistivity measurement can be made with accuracy of ±0.3Ω, then the temperature can be measured with a precision of $\pm 10^{-3}$° K. The C thermometers were obtained from FNAL where they were calibrated to obtain a sensitivity of $\pm 10^{-3}$° K when immersed in LHe. When bonded to metallic surfaces, it is possible that limited thermal contact and the presence of a heat source such as radiation may combine to warm the thermometers. We estimate that this

Figure 18. Resistance versus temperature for a Copper thermometer. The thermometer is made from #39 Cu wire and has a room temperature resistance of 200 Ω. (Data obtained from Moyses Kuchnir of Fermilab.)

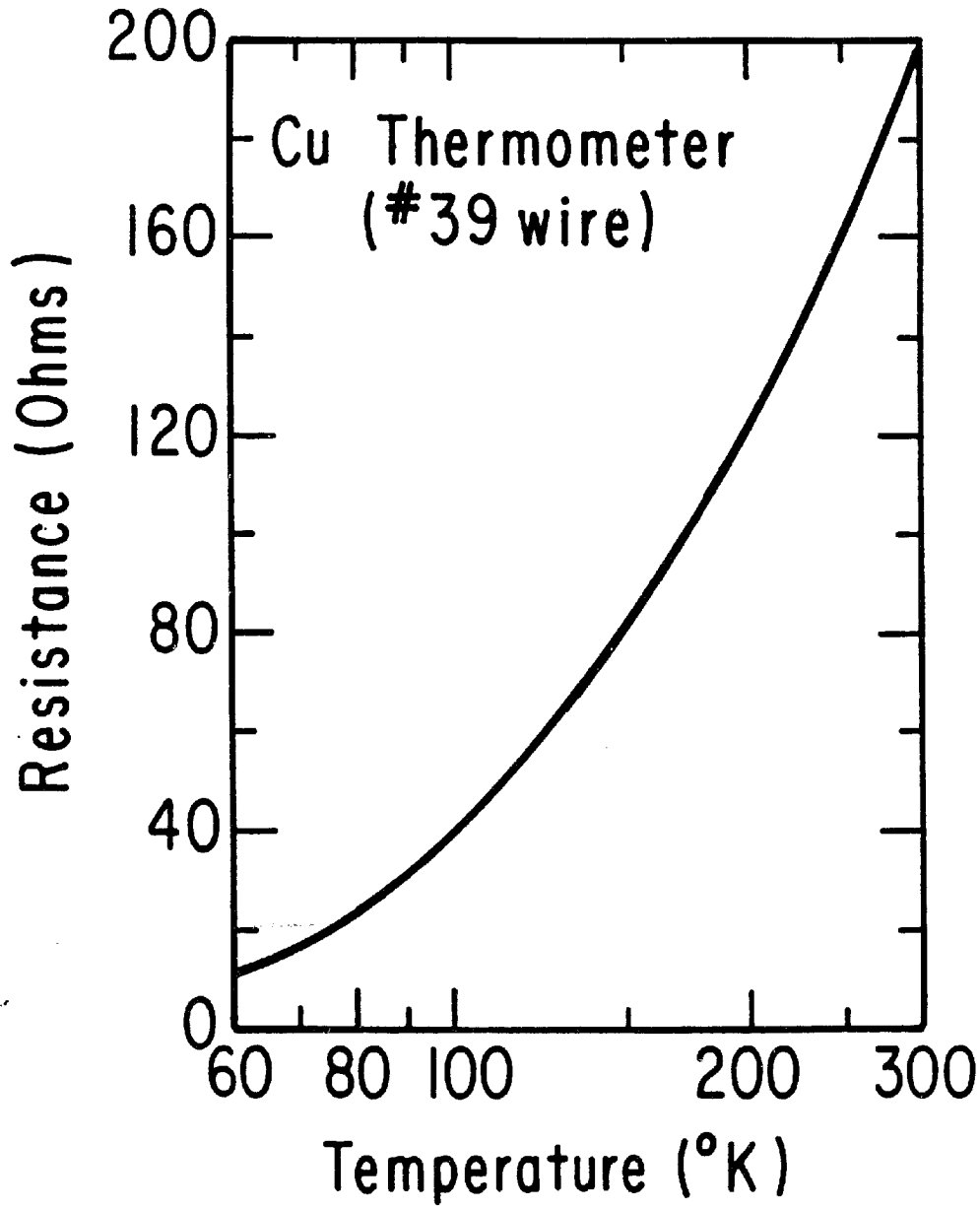

Figure 19. Resistance of a nominal 100Ω, 1/8 W Carbon resistor versus temperature. (Data from Moyses Kuchnir, Fermilab.)

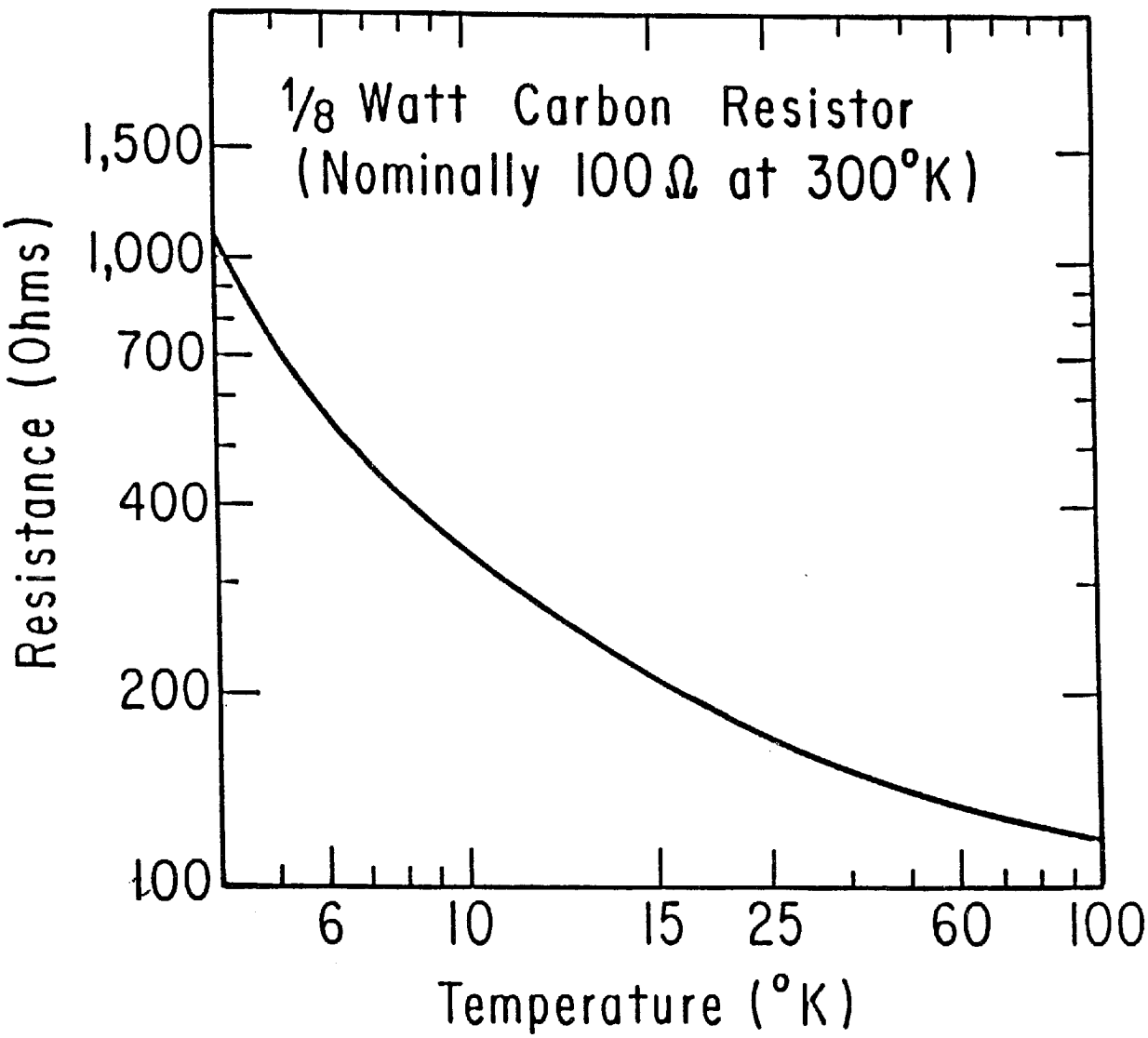

degrades the accuracy of the thermometers to ~0.5° K which is still adequate for our purposes.

To actually measure the resistance of the thermometers we used a "4-lead technique." In this method current is circulated through the thermometer through one pair of leads while a second pair is used to measure voltage. To cancel out any steady-state thermal emf in the thermometers, the current from the current source is reversed and a second voltage reading is taken. One-half the difference of the two readings gives the voltage produced by the current from the current source only. Any thermal emf would not change sign when the current direction is reversed and therefore would cancel when the difference in readings is calculated. From the known current, the resistance is then obtained. A system designed by Moyses Kuchnir of Fermilab was used to measure resistances of 8 thermometers at a preset time interval of anywhere from 1 to 60 minutes. The system, which was controlled by an I.B.M. ("Itty Bitty Microprocessor" - built by Moyses Kuchnir), would read out the time and measured resistances and these would be printed to hard copy.

During steady-state operation LN is filled automatically. The automatic fill system is activated when the LN level in the reservoir drops below the level of a thermal probe. In response to the subsequent change in temperature detected by the probe, the fill system control box switches open a solenoid valve which allows nitrogen gas to pressurize the LN storage dewar. LN is transferred until the liquid level rises above a second probe at which time the solenoid valve is closed and pressure is released from the storage dewar. LHe is transferred manually.

Fe Shield

The vacuum vessel is surrounded by a 183-cm-diameter steel pipe. The pipe is 200-cm-tall and has a wall thickness of 1.3 cm. It rests on a 1.3 cm thick steel plate but is open on the top for access to the apparatus. As a result of the permeability of the steel the field is reduced to ~50 mGauss on the interior. An additional order of magnitude reduction is obtained by circulating currents in wire coils wrapped vertically and horizontally around the pipe. By properly adjusting the currents in these coils we were able to obtain measured field components of 1.0-4.0 mGauss in the region of the detector. table 3 lists field strengths at important positions in the detector for optimum current settings.

Isolation from Vibration and Other Noise Sources

The two gradiometers used in this detector are each braced by G-10 support structures and individually shielded with Pb. To isolate the shielded gradiometers from each other and from vibration sources external to the detector they are each suspended by three hollow G-10 tubes that attach to flanges on the external shell of the cryostat. The flanges, in turn, are vibrationally isolated from the vacuum vessel by means of flexible bellows and critically damped inflatable cushions.[71]

Isolation from environmental pressure and temperature variation is obtained by operating in vacuum. Furthermore, the completely closed aluminum vacuum vessel helps to shield the detector from electromagnetic radiation. Unfortunately the SQUIDs are mounted inside

TABLE 3

AMBIENT MAGNETIC FIELDS DURING COOLDOWN OF CFM I

Position in Apparatus	Average Field Strengths [mGauss] B_x	B_y	B_z
1 Foot Above SQUIDs	11.7	12.5	46.0
SQUIDs	3.3	1.2	1.5
Top Gradiometer	2.2	0.4	0.1
Bottom Gradiometer	1.3	0.5	3.9
Bottom of 4°K Radiation Shield	4.2	13.0	1.0

the LHe reservoir which is open to the atmosphere so that they are susceptible to interference from ambient rf radiation. The operation of the SQUIDs was also found to be affected by the electrical ground configuration of the detector components and cable shields. The final configuration which was free of ground loops is shown schematically in figure 20.

Despite the isolation discussed above, disturbances still make their way to the detector. These can alter the detector signal and even mimic a monopole.[72] We discriminate against these signals by monitoring the environment of the detector for disturbances.

Environmental Disturbance Monitors

From our own experience with spurious signals, (see chapter II), we concluded that a small occurrence rate of spurious monopole-like signals caused by environmental disturbances should be expected. For this reason we designed our experiment to include coincident detection area and we also installed a variety of environmental monitors. Not all of the monitors were used throughout the run of the experiment. The rf voltmeter and the power-line voltage monitor were not installed until the detector had already been operated for ~3 months.

The Performance of the Detector

The successful operation of the detector depends critically upon several factors. First of all, the gradiometers, shields and SQUIDs must be maintained in the superconducting state without excessive expenditure of LHe. Secondly, the shielding, and the isolation of the

superconducting circuits in general, must be sufficient to allow stable signals with typical noise below the expected signal size for a single Dirac-charge monopole. It is then absolutely necessary to demonstrate that environmental disturbances that may induce monopole-like signals also produce clear signals in one or more of the environmental monitors. Only then can we be assured that monopoles can be detected unambiguously.

Cryogenic Performance

Temperature graphs from cooling to nominal temperatures of 78° K and 4.2° K are shown in figures 21 and 22. The large thermal time constants assure that sudden changes in temperature - leading to magnetic fields associated with thermal currents - cannot occur. During steady-state operation the gradiometers and shields are maintained at ~4.5° K. The LHe-cooled radiation shield is actually held at temperatures in the range of ~5.0-5.5° K while the LN-cooled radiation shield varied between ~80 and 84° K. The SQUIDs are immersed in LHe and consequently they maintain a temperature of ~4.2° K. Temperatures at various locations are shown in table 4.

Vacuum in the apparatus is attained in several steps. Initially the system is pumped down to ~7 x 10^{-2} mm-Hg by a roughing pump. At this point the pressure is sufficiently low to allow the turbo molecular pump to be started. The action of this pump reduces the pressure to ~4 x 10^{-4} mm-Hg. The molecular sieve is then heated to clear away trapped gases which are then removed from the system by the turbomolecular pump. When the heaters are turned off the sieve again traps gases and a vacuum

pressure of ~1 x 10^{-4} mm-Hg is achieved. Finally, during LN and LHe cooldowns the pressure drops rapidly to ~5 x 10^{-6} mm-Hg and ~1 x 10^{-7} mm-Hg respectively. Cryo-pumping is dominated by the action of the molecular sieve. The gate valve is closed at this time and the turbomolecular pump is turned off. The pressure remains stable at ~1 x 10^{-7} mm-Hg. (The pressure gauge is located near the outer shell of the vacuum vessel where the temperature is 300° K. It is thus likely that the pressure at the ~4° K detectors is lower than that indicated by the gauge.)

The detector requires ~250 l of LHe to be cooled to stable minimum temperatures at which time the consumption of LHe remains steady at ~10.0 l/d indicating a total heat leak of ~0.26 W. LN consumption at this time is ~15-20 l/d indicating a heat load on the "78° K" radiation shield of ~2.0 W.

Signal and Calibration

The sensitivity of the detector is determined directly by the pseudopoles for several possible monopole trajectories. The overall response of the detector for arbitrary monopole trajectories is determined by the calculation presented in chapter II. It is also possible to use the calculational procedure of that chapter to predict the pseudopole signals. A comparison of the actual and the calculated signals then establishes the validity of the calculation of the overall response of the detector. (Even if no algebraic or computational errors exist in the signal calculation, it is still necessary to verify that the geometrical approximation of a right-circular cylinder shield is reasonable.)

Figure 20. Ground configurations. (a) Configuration of device grounds to avoid ground loops. (b) Configuration of shield grounds for signal leads. The grounding of the thermometer lead shields at the detector was crucial to low noise operation of the SQUIDs.

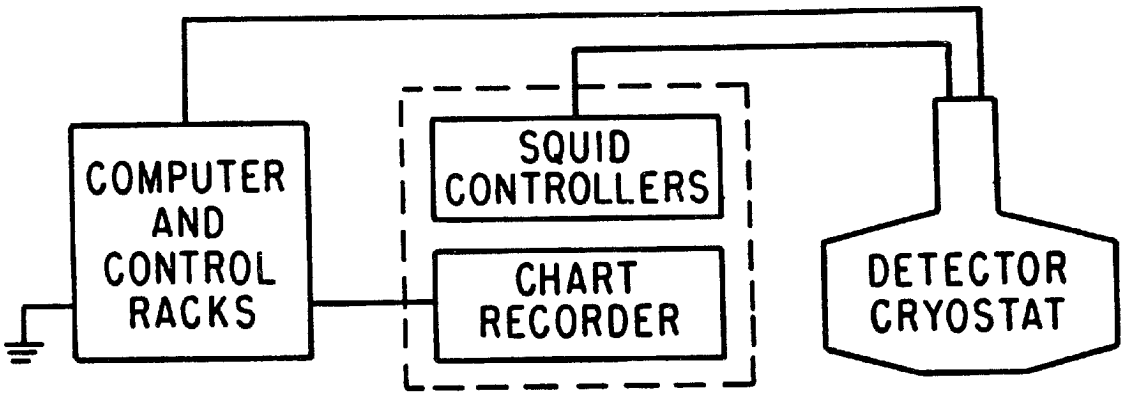

(a)

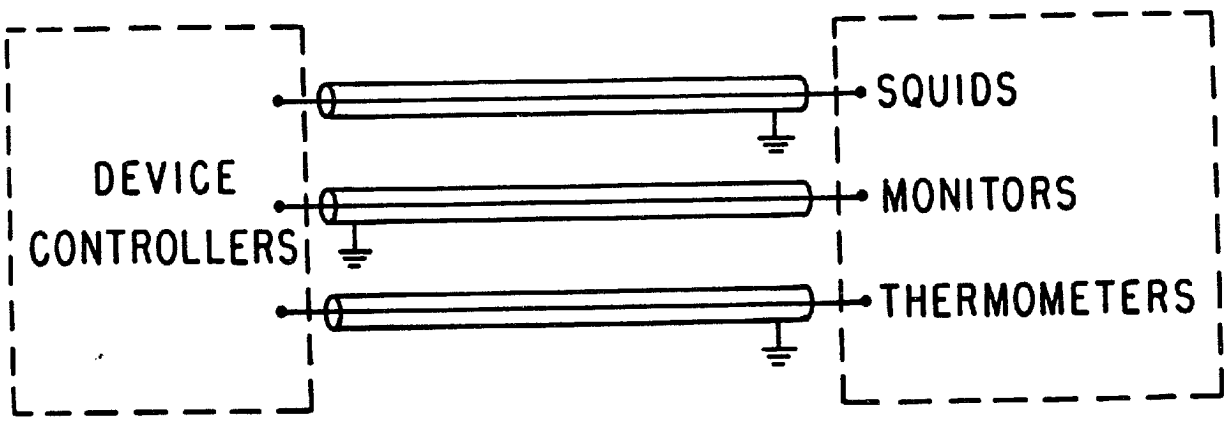

(b)

Figure 21. Liquid nitrogen cooldown plot for CFM I. Shown is the temperature versus time for the detector and the radiation shield.

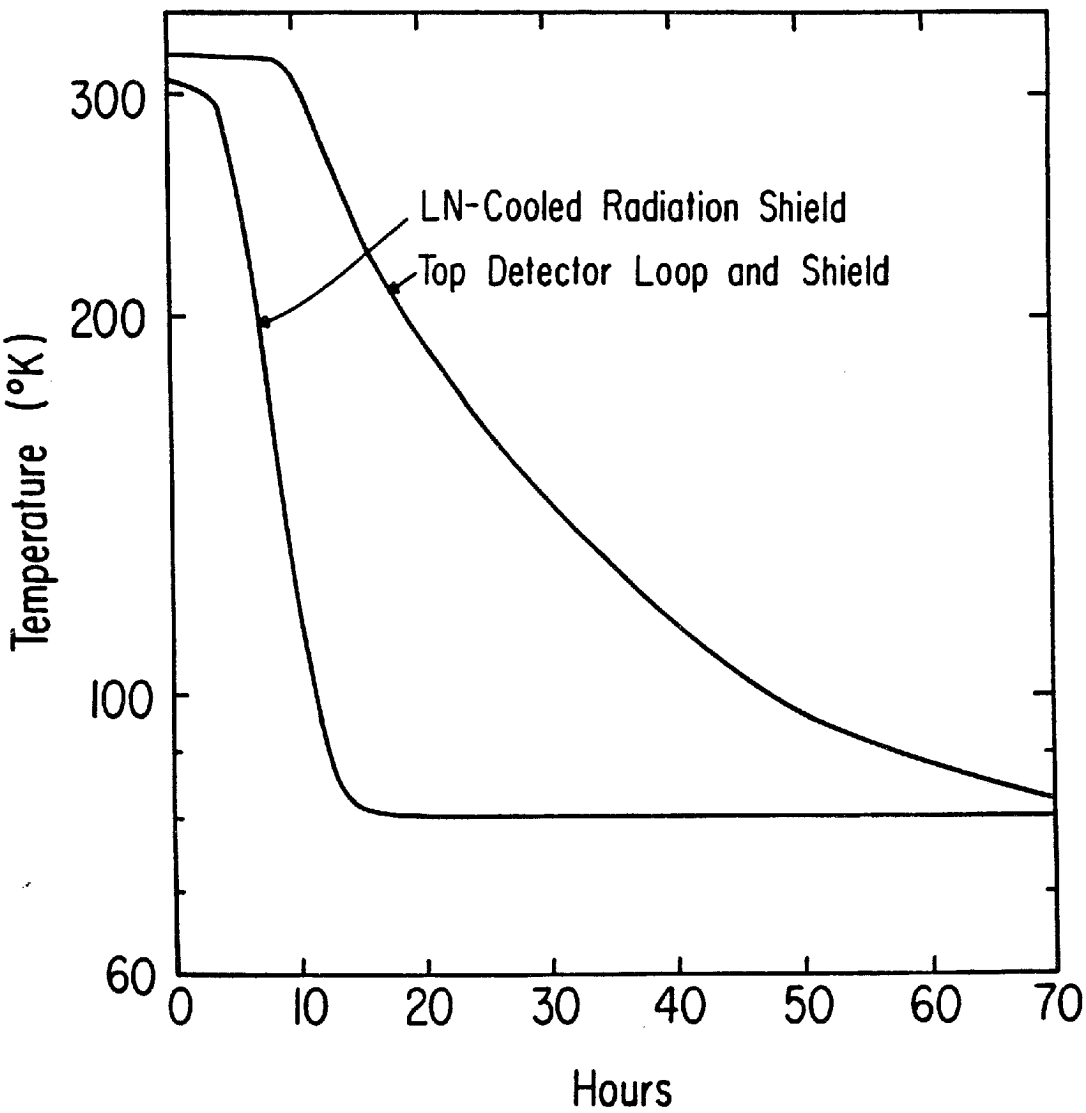

Figure 22. Liquid helium cooldown plot for CFM I. The detector and radiation shield temperatures versus time are shown.

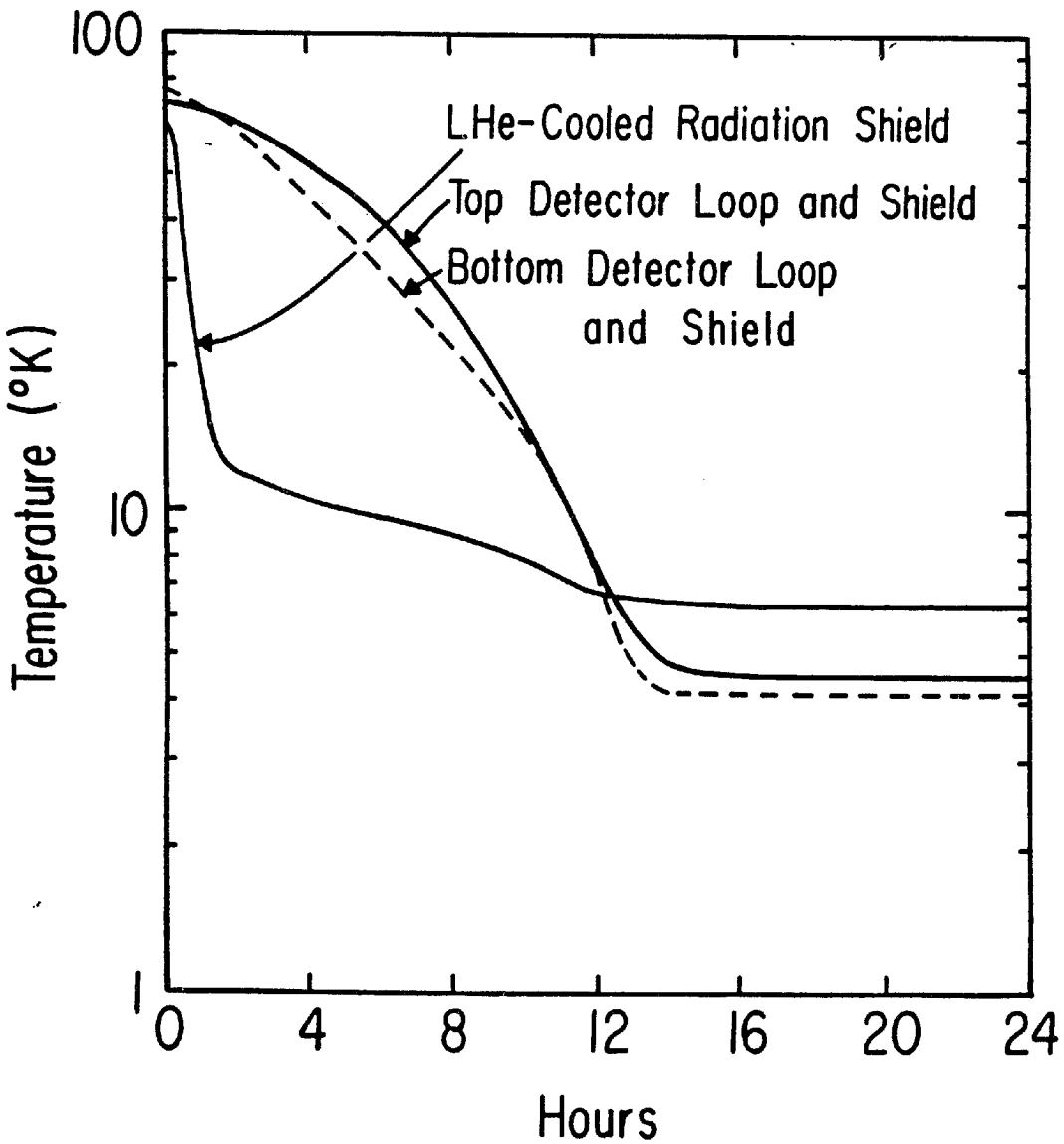

TABLE 4

TEMPERATURES IN EXPERIMENT CFM-I

Position in Apparatus	Temperature [°K]
LHe	4.1±0.3
Exterior Base of LHe Reservoir	4.5
LHe Cooled Radiation Shield - Top	5.8
LHe Cooled Radiation Shield - Base	5.9
Top Gradiometer and Shield	4.5
Bottom Gradiometer and Shield	4.5
LN-Cooled Radiation Shield - Top	80.0
LN-Cooled Radiation Shield - Middle	81.5
LN-Cooled Radiation Shield - Base	84.0

The calculated and actual pseudopole signals are compared in table 5. They are consistent to ±5%. The error in the calculated signals result from an uncertainty of ~3 mm in the positions where the pseudopoles penetrate the shields and also from an uncertainty of ~3% in the flux carried by the pseudopoles. The error in the measured pseudopole signals is due to the noise level in the SQUID signals.

The signals from the superconducting detection circuits exhibited high d.c. stability with drifts of less than 10 $mV\text{-}d^{-1}$. An a.c., (1 Hz), peak-to-peak (pp) noise component of 0.4-1.0 mV was typical for each circuit. The SQUID sensitivities were the same to within 2% and the pseudopole signals indicated a maximum signal of ~5 mV for the passage of a single Dirac-charge monopole through either of the detector loops. The voltage signal-to-noise ratio at 0.1 Hz was determined to be greater than 20.

Response to Controlled Disturbances

To be certain that the detector is capable of unequivocally detecting magnetic monopoles it is necessary to demonstrate as thoroughly as possible that spurious monopole-like signals can be recognized as false events. To this end we disturb the detector in a variety of ways and observe the resulting SQUID and monitor signals. With some amount of care taken in the placement and adjustment of the monitors we established a configuration in which we are confident that all disturbances large enough to produce d.c. offsets in the signal of the size expected for monopoles will also produce easily observed signals in one or more of the monitors.

TABLE 5

COMPARISON OF CALCULATED AND MEASURED PSEUDOPOLE SIGNALS

Pseudopole Position		Calculated SQUID Signal	Top Circuit SQUID Signal	Bottom Circuit SQUID Signal
ρ(cm)	θ(rad)	(mV)	(mV)	(mV)
17.7	5.5	7.1±0.4	7.2±0.2	7.5±0.2
7.9	5.0	6.9±0.4	----	7.5±0.2
14.6	2.6	7.0±0.4	7.2±0.2	7.3±0.2
25.8	2.1	6.5±0.4	----	6.5±0.2
29.0	1.8	5.5±0.4	5.5±0.2	5.5±0.2
28.0	1.6	4.8±0.4	4.9±0.2	5.0±0.2

The most common disturbances to produce d.c. offsets in the SQUID signals correspond to vibration and ambient magnetic field fluctuations. To study the effect of vibration we impart mechanical impulses to the apparatus by tapping the detector at various positions. The impulses are produced by dropping a known mass through a fixed distance and can therefore be reproduced easily. Vibration is monitored by a piezoelectric accelerometer[73] with a sensitivity of 10^{-6} m - sec^{-2}. Vibrations can be imparted directly to the shields and loops by tapping the external flanges to which the suspension rods are attached. Initially we had planned to mount the accelerometer to one of these flanges to monitor vibration in the shielded gradiometers. Our study of the effects of vibration however indicates that vibration of the SQUID systems is the more likely source of a false signal.[72] As a result, the accelerometer is mounted to the SQUID rf heads which mechanically couple to the SQUIDs and also to the external environment through contact with the cryostat. By tapping the flanges from which the shielded detector loops are suspended, the detector signals can be offset by as much as 20 mV. The offsets are typically accompanied by large spikes in the signal, (figure 23). The signal for a monopole, as demonstrated by the pseudopoles, (figure 24), is characterized by a shift from one d.c. level to another without additional structure or observable rise time. We were pleased to see that sending impulses to one shielded gradiometer affected the signal from that gradiometer only, (figure 23). Impulses imparted to the exterior shell of the cryostat have typically no effect on the signals. Tapping near the SQUID tubes and rf heads does however have a strong effect. In the final operating configuration, all of the

Figure 23. Vibration sensitivity test data for CFM I. The response of the superconducting detector circuits when a support flange for one of the shielded gradiometers is vibrated via impact of a weight dropped at regular time intervals is shown. The top two channels are SQUID signals. The bottom channel shows the accelerometer signal. The two circuits are seen to be mechanically uncoupled.

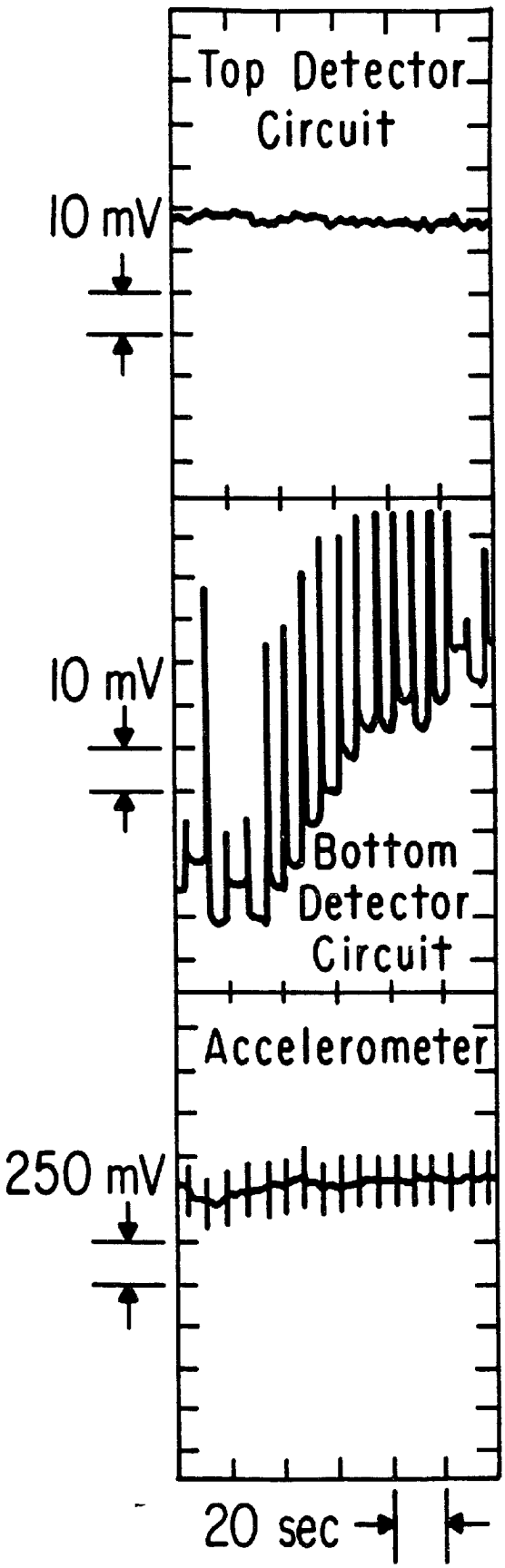

Figure 24. Data sample from run 2 of CFM I. The different a.c. noise levels of the two signals are due to the different intrinsic noise of the SQUIDs. Pseudopoles are turned on remotely by computer for one minute at the end and beginning of two-hour data files as seen in the center of the figure.

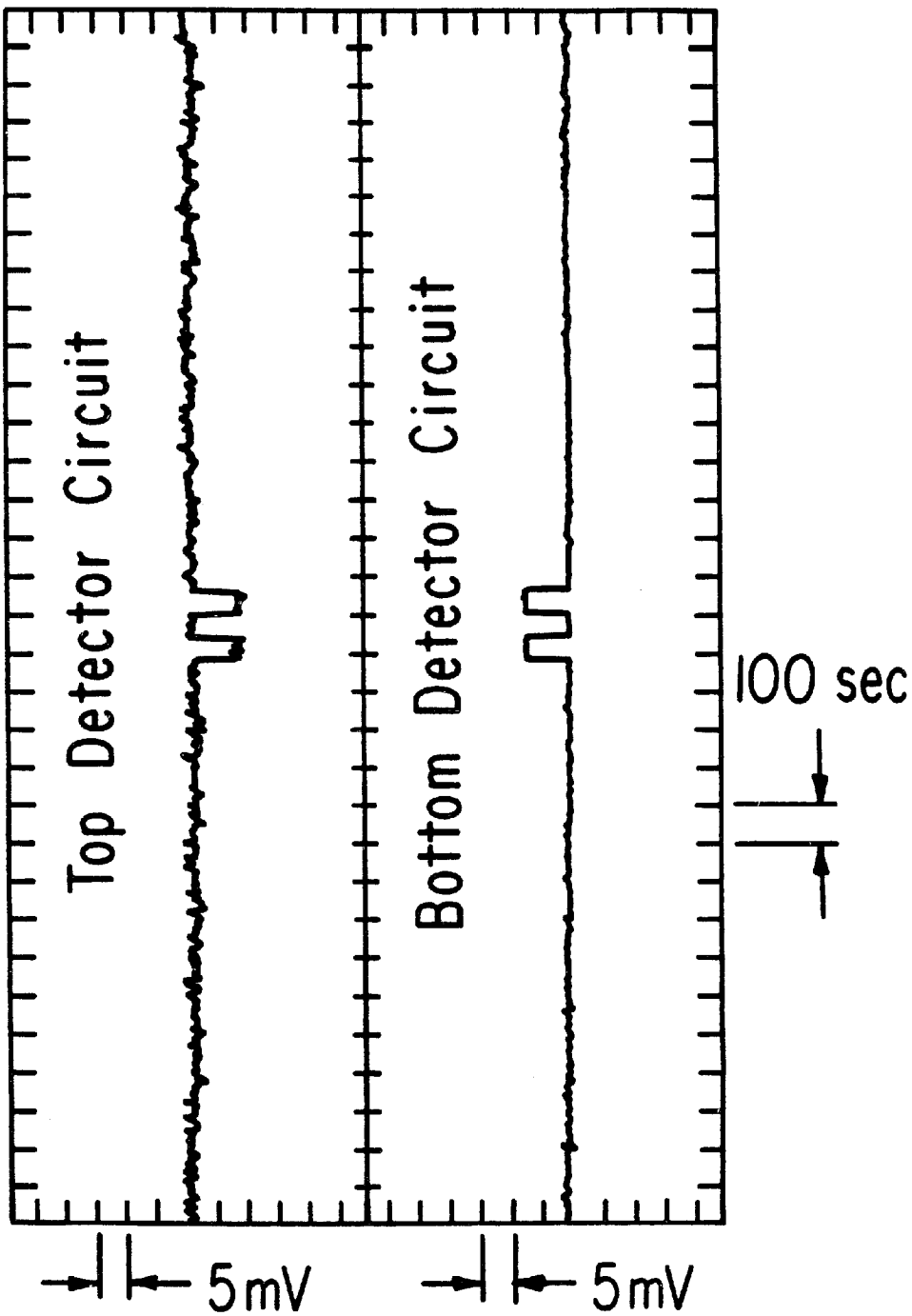

Figure 25. Data from test of sensitivity to rf radiation. The top channel is the rf voltmeter signal used to monitor radiation in the range 2-20 MHz.

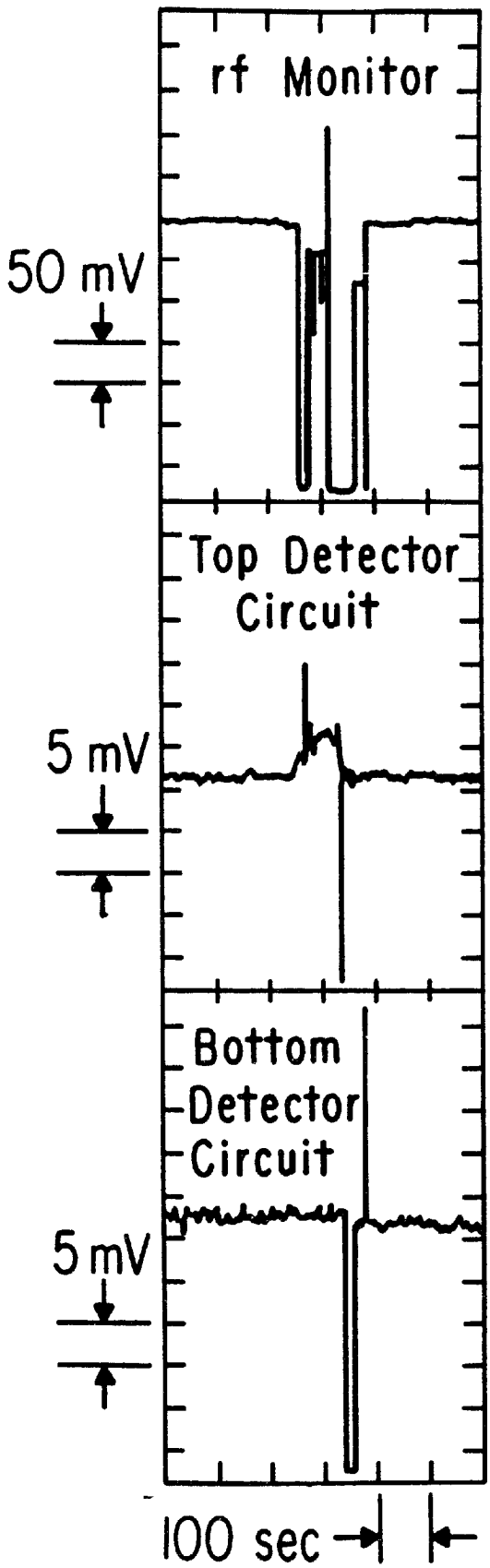

impulses to the SQUID systems that produced monopole-like d.c. offsets in the detector signals also produced clear signals in the accelerometer. We conclude that the shields and loops are sufficiently isolated from the environment to be unaffected by vibration from external sources. There remains the possibility of internal vibrational mechanisms such as sudden stress release etc. These could conceivably produce a very rare d.c. offset. However, the two detection coils are seen to be very well isolated from one another and consequently the simultaneous occurrence of such signals from both gradiometers is expected to have negligible probability. As will be discussed in chapter IV, a residual background of offsets, probably from internal sources, is indeed observed.

We test the effect of external magnetic field variations by stimulating currents in coils of copper wire wound on the steel pipe surrounding the cryostat. A 20 mA pp square wave current with a frequency of ~0.3 Hz produces field variations on the order of several mG at the detector. Three sets of coils with orthogonal orientations are used to produce fields along three cartesian coordinate directions. The fluctuating fields result in SQUID signal offsets of fixed, reproducible amplitudes for specific field components. A fluxgate magnetometer placed below the center of the cryostat to monitor external magnetic fields can easily distinguish these fluctuations and can in fact distinguish field variations which are far too small to affect the detector signals.

Other sources of less frequent environmental disturbances are rf radiation, temperature and pressure variations and power-line voltage

fluctuations. Except in the extreme case of power failure, power-line variations do not appear to affect the detector. Nevertheless a line voltage monitor[74] is installed to signal low or high voltage, sudden spikes or drops in voltage, high frequency noise, and power failure. Similarly the pressure of the vacuum system and the temperatures of various internal surfaces are monitored continuously for fluctuations although there is no evidence of an effect on the signals from these sources. Changes of atmospheric pressure are also monitored. We find that a change in pressure can affect the boiling temperature of the LHe and thus lead to a drift in SQUID signals. Typical pressure changes are too gradual, however, to produce the sudden change in d.c. level expected for a monopole. Finally, large amplitude variations of rf radiation affect the rf resonance circuit of the SQUIDs and can produce sharp sudden offsets of arbitrary size. An rf voltmeter with an attached antenna is used to discriminate offsets produced in this manner. Tests of rf sensitivity in which we produce rf radiation in the 2-20 MHz range in the laboratory indicate that the SQUIDs are sensitive to 5, 9, 11 and 19 MHz radiation with no offset observed at other frequencies, (figure 25). As for the other monitors, the final configuration of the rf voltmeter is such that it can detect any rf radiation that could produce spurious signal offsets.

CHAPTER IV

DATA, ANALYSIS, AND RESULTS

The apparatus described in the last chapter was constructed and operated in the high bay of the High Energy Physics building of the Enrico Fermi Institute at the University of Chicago. Monopole flux data was obtained from two separate running periods. The first run was from August 29 until October 4, 1983 and the second was from January 10 until July 15, 1984. The two runs are distinguished by differences in the configuration and performance of the apparatus as will be presented below. The data for both runs consist of 8 channel strip-chart recordings and magnetic tapes. The magnetic tape data have slightly better time resolution and include information from several monitors whose signals are not recorded on the strip-charts. The strip-chart data can however be analyzed more rapidly. The analysis was therefore performed primarily with the strip-charts while the magnetic tapes were used for better time resolution and for additional monitor information in the careful examination of individual d.c. offsets in the SQUID signals.

Run 1: August 29 - October 4, 1983

In late August of 1983, the bottom superconducting circuit was determined to be adequately shielded and isolated to be used to detect monopoles. The top circuit, though capable of producing an observable

response to a monopole was also significantly affected by magnetic field variations. The response of both circuits to the stimulation of pseudopoles is shown in figure 26 where the slightly impaired functioning of the top circuit is apparent. The response of the circuits to external magnetic fields is shown in figure 27. As a result of its sensitivity to external magnetic fields, we anticipated that the top circuit would be significantly more likely to produce spurious signals than the well-shielded circuit. Accordingly we decided that the data from the two circuits would not be considered on an equal footing. For the analysis of the data from this run, the signal of the bottom circuit was considered to be the primary source of information while the signal from the top circuit was only considered when a d.c. offset had been observed in the primary circuit. By interpreting the data in this way the coincident character of the detector is retained although the total sensitive area is reduced by ~700 cm^2 averaged over all angles which is the area of the top circuit that is not in coincidence with the bottom circuit. The loss of non-coincident sensitive area is only significant in the instance that there are no single, (non-coincident), signals consistent with the expected monopole signal in either of the circuits, in which case a flux limit could be set which is based upon the total sensitive area rather than the smaller coincident area.

The data were processed in several stages. A first scan of the chart recordings was carried out as they were produced in the run. In this scan extended dead time intervals were designated and their

Figure 26. Pseudopole signals and data sample from Run 1. The instability and enhanced noise in one circuit is the result of a break in the superconducting shield of the signal leads for that circuit.

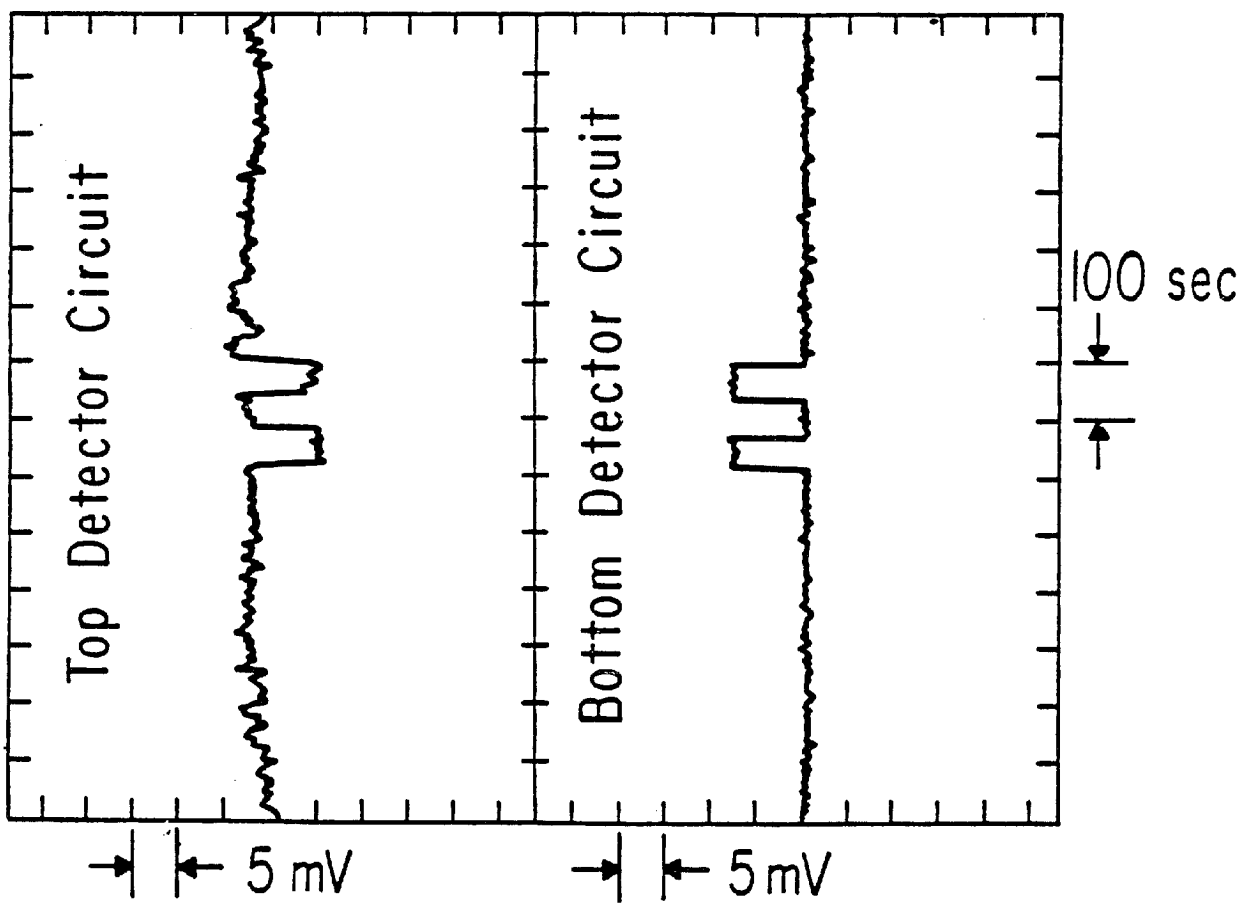

Figure 27. Magnetic field sensitivity test data for CFM I. Sensitivity to external magnetic field is tested by circulating a square wave 20 mA current in three separate current coils located on the iron pipe surrounding the apparatus. The test data in this figure are from Run 1 in which the superconducting shielding of the signal leads from the top gradiometer to the SQUID had a small break.

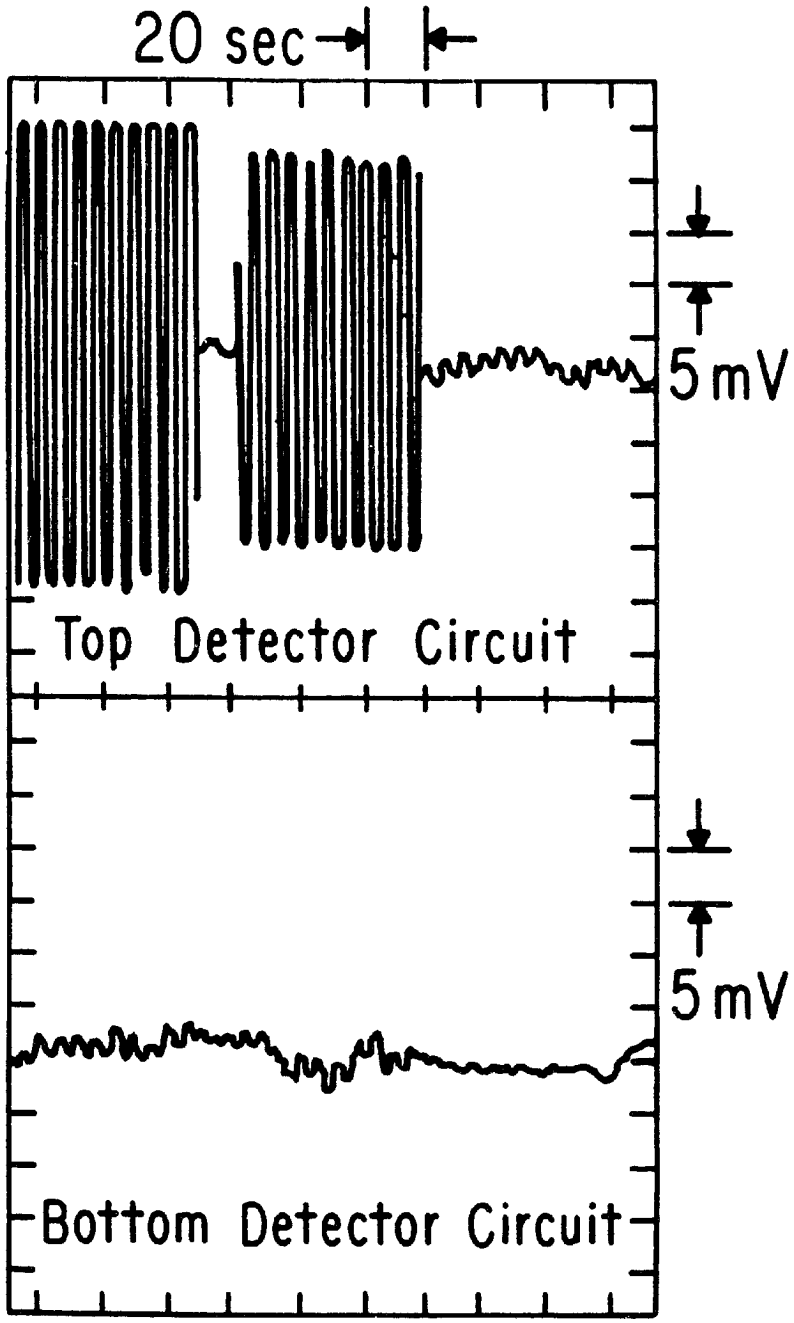

durations were recorded. In addition, offsets in the SQUID signals and concurrent monitor signals, (within a two minute interval centered upon the SQUID signals), were entered into a catalog. A second scan was dedicated solely to a careful search for offsets in the signal of the bottom circuit. Once again these were catalogued along with any coincident, (±1 min), signals from the monitors.

The extended dead time intervals that were designated in the first scan correspond to periods when work was done on the apparatus or when information from a SQUID or monitor was not being accumulated. The system was considered to be off the air in the former case because work on the apparatus often constituted a large source of noise in the SQUID and monitor signals. Furthermore we feel that under such disruptive circumstances the detector should not, in general, be trusted to discriminate between real and false events. The discriminating capabilities of the detector are also seriously degraded when the signal of a SQUID is not recorded since coincidence is lost. Similarly when a monitor signal is absent any candidate monopole signals could possibly have been produced by disturbances which would otherwise have been detected by the missing monitor. Loss of monitor data usually occurred when the signal drifted off-scale of the measuring device or of the chart recorder. This could lead to substantial loss of exposure time if it occurred in the middle of the night and was not remedied until the following morning. The work that was done on the apparatus generally served to upgrade the sensitivity and stability of the monitors or to maintain the cryogenic operation of the system. Usually when work was done on the apparatus the people

who were involved in the work would mark their starting and finishing times on the chart recorder so that dead time could be clearly established in the later analysis of the data. When this was not done, and monitors indicated continued extreme disturbance of the apparatus typical of work in progress, the dead time interval would be determined by setting the endpoints of the period at ten minutes before the beginning and ten minutes beyond the end of the disruptive period indicated by the monitors. In this way dead time intervals which were not marked could be established consistently and without bias.

Of the operating time that remains after the crude dead time cut of the first scan there is an additional 15% reduction that results from dead time associated with environmental disturbances as detected by the monitors. These disturbances are typically of very short duration and come from a variety of natural sources such as large trucks in the alley alongside the building in which the experiment is performed or even thunder and lightning in a spring thunderstorm. Most of these disturbances however arise from activity of people in the building. The amount by which the data are reduced is determined by a study of run 2 data discussed below. We concluded that since there were fewer monitors used in run 1, the percentage of dead time determined for run 2 would be a reasonable upper limit for that of run 1. (In any case, the majority of the dead time, (~13%), can be ascribed to data from the sound-level monitor which was used in the same way in both runs.)

The SQUID signals were processed by a 1 Hz low pass filter. The a.c. noise of the well-shielded circuit was 0.8 ± 0.4 mV pp. The drift in d.c. offset level was 2.0 - 10.0 mV-d^{-1}. Thus sudden offsets as small as 0.2 mV can be easily resolved. For such small offsets, the rise time cannot be resolved if it is less than ~15 sec. For offsets greater than ~0.5 mV the rise time can be resolved to ~5 sec and is limited only by the chart-recorder pen-width which is ~0.25 mm. For this reason, and because there exists only negligible probability for a monopole to produce an offset below 1.0 mV, only those offsets $\geq$ 1.0 mV were catalogued.

When an offset $\geq$ 1.0 mV was observed, all information about it and the state of the apparatus was entered in the catalog. Chart recorder pen positions varied by up to ±2.0 mm along the time axis which corresponds to an apparent time interval of ±40 sec. Cataloged monitor data thus consisted of signals above stable background and within an apparent two minute interval centered on the SQUID signal. The environmental monitors used in this run included a fluxgate magnetometer, an accelerometer, two pressure transducers, (to monitor atmospheric pressure and the pressure of the LN fill-system), and a sound-level meter. Also, the temperature and pressure of the cryostat and the level of the LHe in the reservoir were monitored by standard devices, (see chapter III). The rf voltmeter and line-voltage monitor were not installed for this run.

It is tacitly assumed that the only observable effect of a passing monopole is a d.c. offset in the SQUID signal(s) which would have no resolvable rise time or other structure at 1.0 Hz filtering.

This is what is observed, for instance, when the pseudopoles are stimulated. No signals above stable backgrounds are expected from any of the monitors at this time. If a monitor signal occurred simultaneously with the SQUID signal then there exists the possibility that the latter could have been caused by the disturbance that produced the monitor signal. The detector is therefore considered insensitive at this time and the offset is disregarded. Similarly, offsets with resolvable rise times or other structure inconsistent with the expected monopole signal are disregarded. (The number and cause of disregarded events will be discussed later.) D.c. offsets from the bottom circuit which survive these cuts are histogrammed in figure 28. The probability distribution for the signal of a monopole, (calculated in appendix A and chapter II), is also shown. None of the unvetoed offsets exceed 3.2 mV and none occur in coincidence with an offset in the top detector circuit. The probability that a monopole passing through the detector will produce an offset at or below 3.2 mV is ~1.2%. The complete absence of offsets in the high probability signal-size range thus indicates that the observed offsets represent a background of spurious signals whose sources were not detected by the monitors. It is probable that many of these offsets arise from vibration of the SQUID systems. These kinds of mechanical disturbances were not monitored in this run. In run 2, they were monitored to some extent by mounting the accelerometer to the SQUID rf heads. The subsequent occurrence of unvetoed offsets was dramatically reduced in that run.

Figure 28. D.c. offsets from runs 1 and 2 and detector response function for CFM I. Single d.c. offsets from Runs 1 and 2, (left-hand scale), and the calculated response function of the detector, (right-hand scale), giving the probability of a monopole passing through the detector producing a particular signal size. The shaded regions correspond to offsets from Run 1 and unshaded regions to offsets from Run 2. Only offsets which do not correlate with monitor signals are shown. There were no coincident offsets of this type.

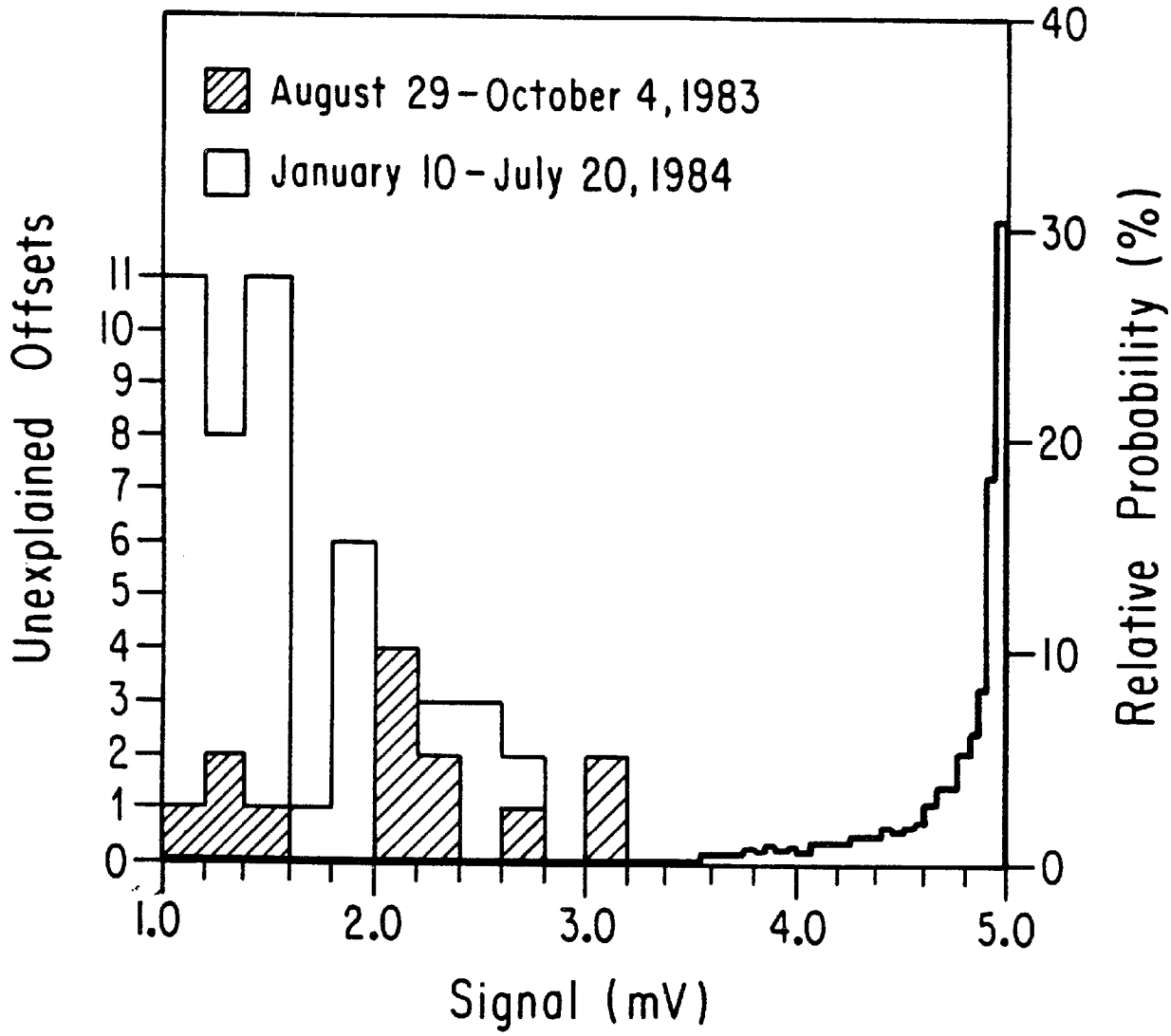

The area of one gradiometer averaged over solid angle is 1,400 cm^2. The detector was operated over a period of 37 days with a total live time exposure of 19.2 days. The absence of monopole candidate events thus sets a limit on the flux of $f_m \lesssim 7.7 \times 10^{-11}$ cm^{-2} sr^{-1} sec^{-1}, (90% Confidence Level).

Run 2: January 10 - July 17, 1984

Between early October and mid-December of 1983 the magnetic field leak of the top circuit was located and repaired. The apparatus was cooled in late December and we found that although the top circuit still showed more external field sensitivity than the bottom circuit, it was nevertheless adequate to detect monopoles. Figure 24 shows a typical data sample from this run. Table 6 compares the magnetic field sensitivities of the circuits in the two runs. At 1.0 Hz the SQUID signals had residual a.c. noise components in the range 0.4 - 0.7 mV pp and d.c. drifts less than 10.0 $mV\text{-}d^{-1}$.

As in run 1, the strip-charts were the primary data used in the analysis while the magnetic tapes were used for additional information regarding individual offsets. The data were analyzed in three scans. The first two scans proceeded in exactly the same manner as the two scans in the analysis of run 1 data. In the third scan, a careful determination of the dead time due to environmental disturbances was carried out.

Unlike the analysis of run 1 data, the offsets that were cataloged in scans 1 and 2 of run 2 data were entered into a computer file. A computer program was then written to study these signals and

TABLE 6

COMPARISON OF SENSITIVITY TO THE AMBIENT MAGNETIC FIELD BEFORE AND AFTER REPAIR OF SHIELD FOR TOP CIRCUIT

Current Coil Being Used to Produce the Ambient Magnetic Field	SQUID Response [mV]			
	Before Repair		After Repair	
	Bottom Circuit	Top Circuit	Bottom Circuit	Top Circuit
COIL 1	1.5	44.0	1.5	8.0
COIL 2	2.0	37.0	2.0	14.0
COIL 3	---	2.0	---	1.0

to apply successive cuts for correlations with monitor signals. The program also used the time information of the monitor signals relative to the SQUID signals to calibrate the chart recorder pen positions. This was done by histogramming the number of signals in each chart recorder channel as a function of the apparent time separating the signal from the SQUID signal offsets. If only one SQUID displays a signal in the event then the zero of time corresponds to the time at which that signal occurred. If both SQUIDs have signals above stable background then the top detector circuit is used as the time reference. The events which fall into this last category enable us to determine the relative pen positions for the SQUID channels. Figure 29 shows a typical timing histogram which, in this case, plots the number of magnetometer signals occurring in the vicinity of signals from the top detector circuit. The relative positioning of the pens along the time axis did not change throughout the experiment, (they were periodically checked), and so we expect simultaneous signals in the different channels to have apparent times relative to SQUID signals which are all within a narrow range. Furthermore, if the variance of the apparent times is only the result of human error in measuring these times on the chart records, then we expect the distribution of the number of signals to be gaussian. This is in fact observed as can be seen in figure 29. Note that 4 disturbances in the vicinity of $\Delta t = 0$ do not fall under the peak. In fact the mean and standard deviation for this peak are $\langle \Delta t \rangle = 12.41$ sec and $\sigma = 2.0$ sec so that all four of these signals occur at more than 3 standard deviations from the mean. We conclude that they cannot have occurred

simultaneously with the SQUID offsets. In general we require that a signal from a disturbance monitor occur within 2 standard deviations of the mean time to the SQUID signal to be considered a simultaneous and possibly correlated occurrence. Figure 30 shows the histogram of signals from the bottom detector circuit as a function of the apparent time to a signal from the top detector circuit. Only the two signals above $\Delta t = 5$ sec are inconsistent with a possible correlation. (As will be discussed below, all of these events also contain evidence for coincident environmental disturbances.)

Most of the work that was necessary to establish a stable operating configuration was performed in run 1 and consequently the percentage of crude dead time was reduced from 39% in run 1 to only 16% in this run. To determine the percentage of dead time from environmental disturbances of very short duration, a sample consisting of 252 hours of data was studied. The sample consists of twenty-one, 12-hour periods. These correspond to either daytime, (6:30 - 18:30) or nighttime, (18:30 - 6:30), and are distributed uniformly over the operating period of run 2. They also represent a uniform distribution over the seven days of the week. Consequently the dead time determination is not unevenly weighted by night or weekend data when the building is unoccupied and environmental disturbances are less frequent.

Dead time in the sample data was determined by the simple criterion that a monitor channel display a signal of at least two times the stable noise background of that channel. This noise is intrinsic to the monitor and/or the result of a continuous

Figure 29. Timing histogram for magnetometer signals relative to top gradiometer signal offsets in CFM I. The histogram plots the number of magnetometer signals versus the apparent time to an offset in the top detector circuit signal within a ±1 minute range as measured on the chart recorder. Such graphs are used to correct for relative pen positions of the chart recorder so as to determine whether a disturbance is truly simultaneous with the SQUID signal. The distribution is fit to a gaussian and signals occurring more than two standard deviations from the mean are not considered to be strongly correlated with the corresponding SQUID signals.

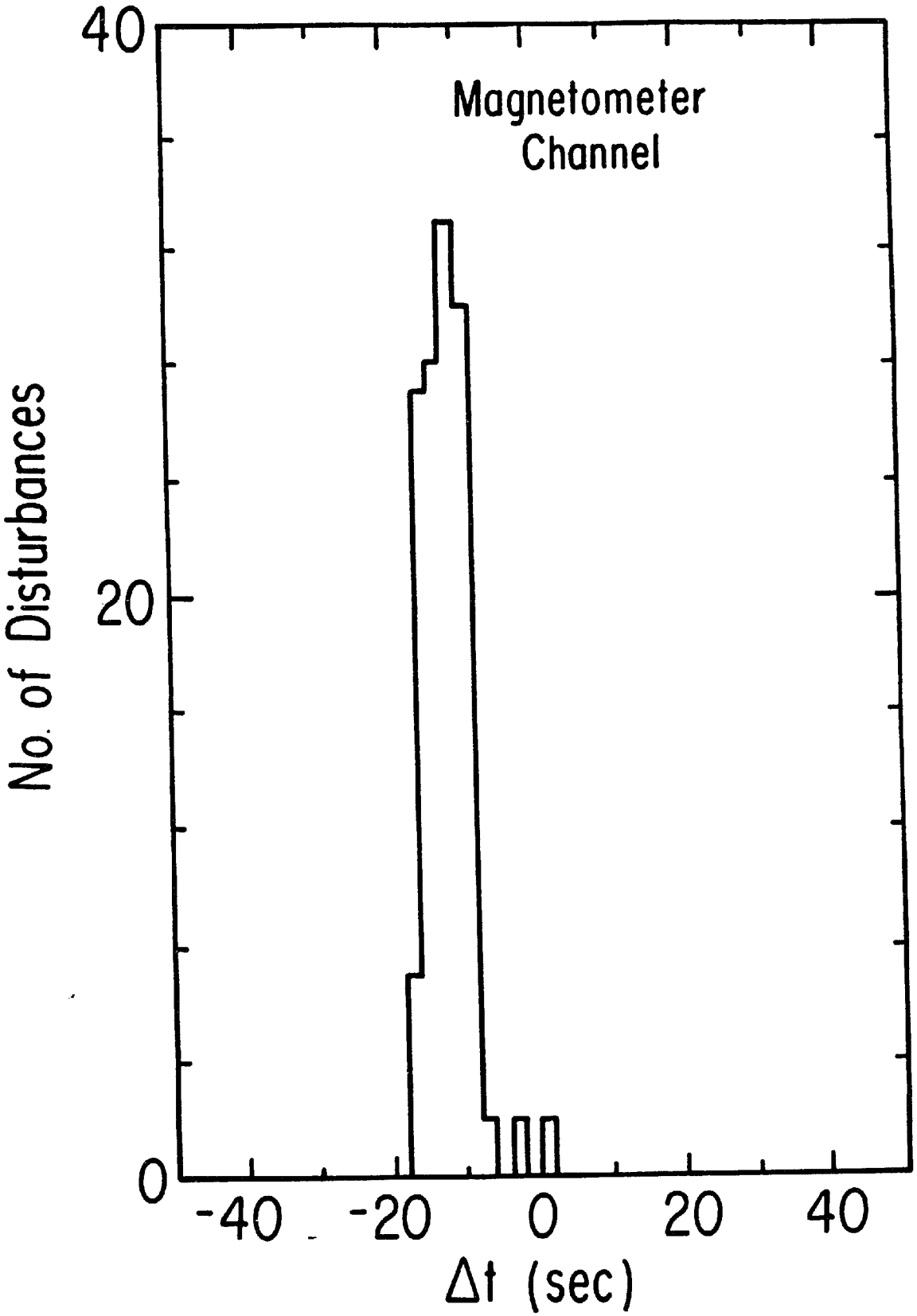

Figure 30. Timing histogram for bottom gradiometer signals relative to top gradiometer signal offsets in CFM I. The histogram plots the number of offsets in the bottom detector circuit signal as a function of the apparent time to an offset in the top detector circuit signal within a ±1 minute range as measured on the chart recorder. The distribution is fit to a gaussian. Offsets occurring more than two standard deviations from the mean are not considered to be correlated.

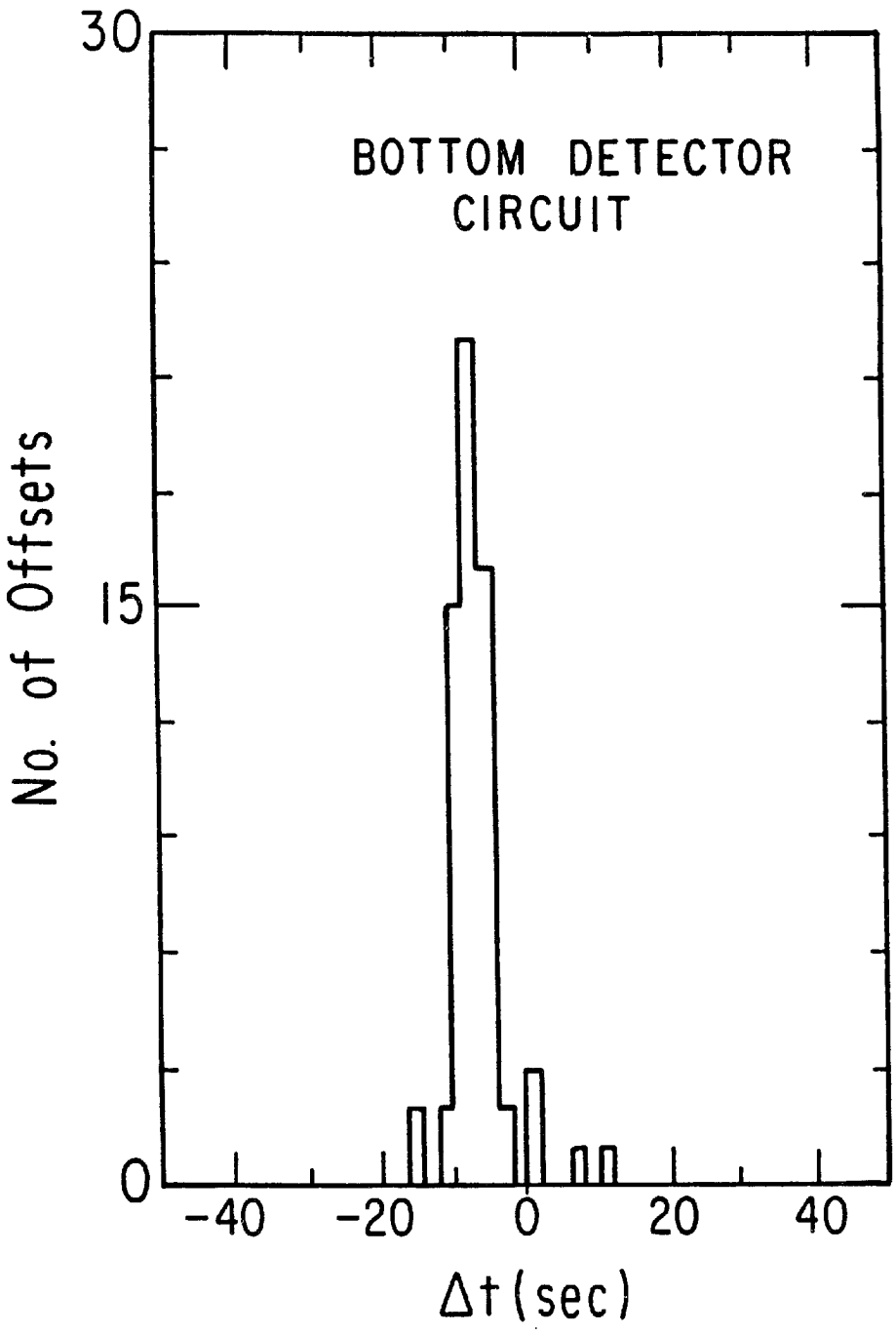

background of disturbances which do not affect the signals from the superconducting detector circuits.

When monitor signals meeting the dead time requirement were found in the sample data, the actual amount of dead time associated with the disturbance was taken to be the apparent duration of the signal, (typically a few to 10 seconds), plus an amount corresponding to our uncertainty in timing relative to the SQUID channels.[75] On average there were roughly 300 disturbances leading to dead time in each of the 21 periods. The results of the study are given in table 7. The average percentage dead time is ~15%.

We now turn to the study of the observed SQUID signal offsets. As for run 1, offsets $\geq$ 1 mV were cataloged along with monitor signals within a two minute interval. There were a total of 227 events cataloged. Thirty-one pieces of information plus a one line comment about each event were entered into a computer file for systematic analysis. Table 8 lists the information on file for an event containing a single 12.7 mV offset in the bottom detector circuit signal. For each event the file has provisions for information not only about the size of the signal but also its structure. SQUID offsets, for instance, often included spikes at the initiation or completion of the step before establishing a final new offset level, (see figure 23). These are called "overshoots." In addition, the SQUID signals sometimes displayed observable rise times. In this case a single bit in the record was used to indicate that the offset occurred too slowly to be caused by a monopole. Magnetic field variations also occurred in d.c. offsets with occasional "overshoots."

TABLE 7

DEAD TIME STUDY RESULTS

Period Day	Date	Live Time Remaining After Scan 1 Cut	Additional Dead Time Measured in Scan 3	% Dead Time (Scan 3)
Wed	Jan 11, 1984	565 min	213 min	37.8
Wed-Thu	Jan 25-26	711	43	6.1
Thu-Fri	Feb 2-3	707	35	4.9
Wed	Feb 15	344	77	22.5
Fri	Feb 24	375	66	17.3
Fri-Sat	Mar 9-10	552	48	8.7
Sat-Sun	Mar 17-18	704	32	4.5
Sat	Mar 24	704	47	6.7
Sun	Apr 1	697	58	8.3
Tue-Wed	Apr 10-11	704	47	6.6
Mon-Tue	Apr 15-16	712	29	4.0
Mon-Tue	Apr 23-24	710	42	5.9
Mon	Apr 30	697	272	39.0
Tue	May 15	415	170	41.0
Tue-Wed	May 22-23	710	71	10.0
Mon	May 28	710	126	17.7
Wed-Thu	Jun 6-7	700	96	13.7
Tue	Jun 12	653	222	34.0
Sun	Jun 17	484	53	11.0
Fri-Sat	Jun 29-30	222	20	9.2
Sat-Sun	Jul 7-8	692	20	2.9

Average Percentage Dead Time = 14.9%

TABLE 8

DATA RECORD FOR EVENT 39: A 12.7 mV OFFSET

Record: Line 1	
Event No.	39
Type (1 = Top, 2 = Bot, 3 = Both Circuits)	2
Date (Last Digit of Year, Month, Day)	40206
Time	1720
Day of Week (1 = Monday)	1
Chart Recorder Sheet No.	68A
Top Circuit Step Size (mV)	---
Overshoot at Start of Step	---
Overshoot at End of Step	---
Time of Bottom Circuit Step	---
Stepsize	-12.7
Overshoot at Start of Step	0.0
Overshoot at End of Step	-1.3
Slow Rise (0 = False, 1 = Yes Top Cct, 2 = Yes Bottom Cct)	0
Record: Line 2	
Time of Magnetometer Signal	---
Stepsize	---
Overshoot at Start of Step	---
Overshoot at End of Step	---
Time of Sound Monitor Signal	---
Signal Size	---
Duration of Signal	---
Noise Background	---
Time of Accelerometer Signal	---
Signal Size	---
Noise Background	---
Time of rf-Voltmeter Signal	---
Signal Size	---
Noise Background	---
Record: Line 3	
Time of LN-Pressure Monitor Signal	---
Signal Size	---
Time to Last LN Fill (Minutes)	381
Time to Last LHe Transfer (Minutes)	4455
Record: Line 4	
Comment	After Fire

The accelerometer and rf voltmeter almost always produced signals in narrow spikes so that only signal size and noise level were listed for these channels. The sound meter frequently produced signals of substantial duration, (up to 30 sec), so that the width of the signal was listed in this case. In the instance that some structure in a signal could not be described by the established categories, this information would be put into a one line comment. The event records also contain information about sudden changes of pressure in the LN fill-system since these could induce otherwise unheralded vibrations inside the detector apparatus. Information regarding time to last fill of LN or LHe cryogenic fluids were listed to enable us to determine whether the rate of SQUID signal offsets is enhanced in the hours following the rather disruptive fill processes.

The analysis of the event proceeded in several stages. Events containing an offset in only one SQUID were considered first. The events were then cut from the sample and disregarded if the information in the records indicated correlation with environmental disturbances as indicated by the monitor signals. A pass through the entire event catalog was made for each monitor before continuing on to consider correlations with other monitor signals. In order to veto an event at least two requirements must be fulfilled. First of all the monitor signal must be at least twice the size of the local noise background. (For the magnetometer and LN fill pressure monitor there were typically no backgrounds so that the minimum signal size for veto was taken to be 4 times the chart recorder pen-width.) Secondly, we require that the monitor signal occur simultaneous to the SQUID offset

as determined in the timing study discussed above. For each stage of the veto process a histogram is made of the unvetoed events vs. SQUID signal offset size. For the events containing signals from both SQUIDs, a succession of scatter plots are also produced. For the sake of brevity only the raw data plots and the plots produced at the end of the veto process are included in this work, (see figures 31, 32, and 28). In addition, table 9 breaks down the data into the number of events with correlations in various monitor channels. Note that only 77 of the vetoed events have correlations with only one monitor channel. Out of these events, 68 have a simultaneous monitor channel signal which is much larger than twice the current noise level in that channel. The remaining 9 events have simultaneous monitor signals which are only 2.0 to 5.0 times the noise level. However, 5 of these 9 events can also be eliminated because the SQUID offsets very clearly display additional structure that is not expected for a monopole. The remaining 4 events, which might be said to contain only very weak evidence of a simultaneous environmental disturbance, are listed in table 10. Because of the marginal quality of the monitor signals in these events as compared with other vetoed events we have chosen conservatively to reclassify them as unvetoed signals. All 4 events correspond to single offsets in one of the superconducting circuits. In addition, they all lie in the interval from 1.0 mV to 1.8 mV so that they are very unlikely to correspond to monopole events. Of the 182 events that were cut due to correlations with large monitor signals, 173 of the events correlated with a signal from the magnetometer or the sound level meter or both. Of the remaining 9

TABLE 9

NUMBER OF EVENTS CORRELATING WITH VARIOUS MONITORS

Correlating Monitors	Number of Events	No. of Events in Which Offsets Have Extra Structure
None	41	7
Magnetometer (MAG)	49	7
Sound Level Meter (SL)	19	4
Accelerometer (ACC)	5	1
rf-Voltmeter (RF)	3	1
LN Fill-Pressure Transducer (LN)	1	0
MAG + SL	82	8
MAG + ACC	5	1
ACC + SL	3	0
RF + SL	3	0
ACC + LN	1	0
MAG + LN	1	0
MAG + RF	1	1
MAG + SL + ACC	7	0
ACC + RF + SL	2	1
MAG + SL + LN	1	1
MAG + SL + RF	1	0
RF + LN + SL	1	0
ACC + RF + LN + SL	1	0
Totals	227	32

Figure 31. D.c. offsets prior to monitor signal cuts in CFM I. Single offsets observed in the signals from each detector circuit in Run 2 before cuts were made for correlation with environmental disturbances are shown.

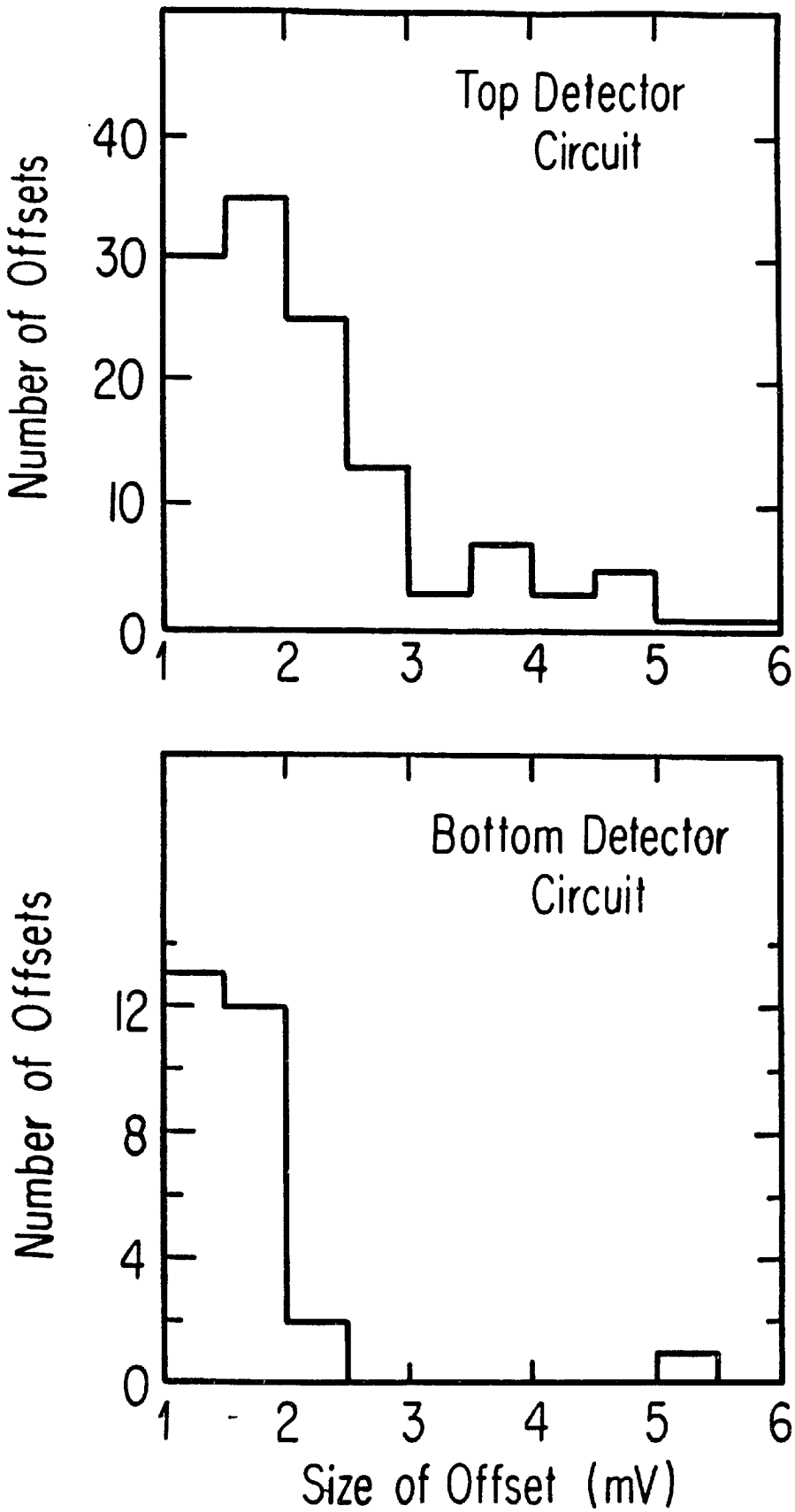

Figure 32. D.c. offsets after all cuts in CFM I. Single offsets in the signals from the detector circuits in Run 2 after all cuts were made for correlations with environmental disturbances are shown.

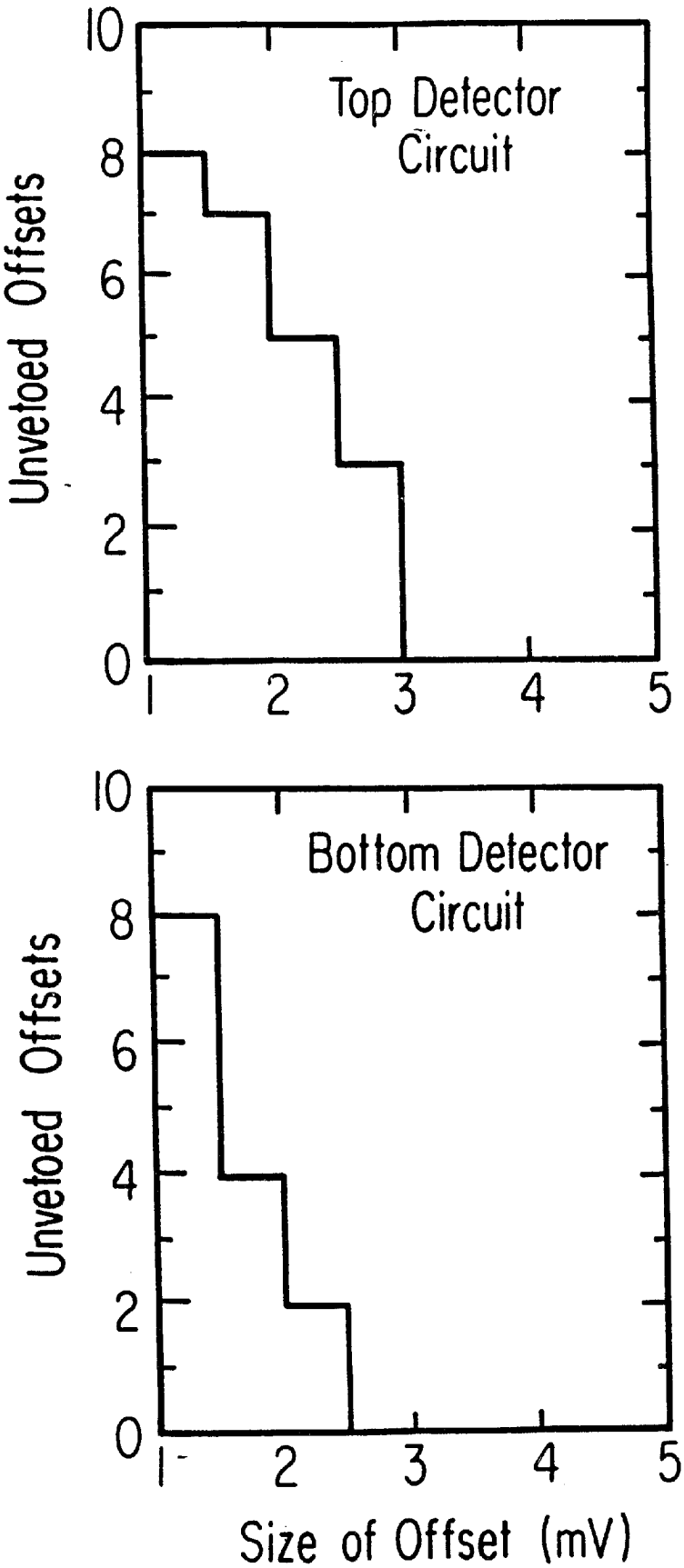

TABLE 10

FOUR EVENTS WITH A SINGLE WEAK MONITOR SIGNAL

Event No.	Circuit	Offset Size (mV)	Monitor	Monitor (Signal/Noise)	Date	Time
24	Bottom	1.5	Mag	2.8	Jan 25	1:31
114	Top	1.5	LN	4.0	Mar 28	18:06
127	Top	1.8	SL	5.0	Apr 8	15:27
174	Bottom	1.3	SL	6.5	May 12	5:33

events, 6 are correlated with a signal from the accelerometer and 3 correlate with a signal from the rf-voltmeter.

It is not surprising that many of the disturbances were manifested as magnetic field changes and as sound since the detector was located near to an area where heavy objects were loaded to trucks. Interference from rf radiation could most frequently be traced to the large solenoid valve used in the LN fill-system. The valve operated at 60 Hz, but very high frequency components were radiated as the valve was switched on and off.

Among the 41 events in which there are no monitor signals 7 events can be discounted as a result of clear extraneous structure in accompaniment to the d.c. offsets. All 7 of these events contain signals from one SQUID only and lie between 1.0 and 2.0 mV. The remaining 34 events cannot be vetoed on the basis of monitor signal or extra signal structure criteria. Together with the reclassified events in table 10, we are left with a group of 38 events for which there is no strong and direct evidence of a particular source. All but one of these events, (23 from the top circuit and 14 from the bottom circuit), are histogrammed in figures 32 and 28. The offset of 12.7 mV from the bottom detector is not shown. The recorded information from this event is listed in table 8. This signal occurred one hour after we recovered from a catastrophe in which the power cord of the computer caught fire. The rf voltmeter had not been installed as of that time. We suspect that this offset was due to rf interference. In any case it is not consistent in size with the signal expected for a single Dirac-charge monopole, or even an

integral number of Dirac charges. Discounting this offset, the unvetoed offsets from each detector circuit were fitted to the tails of gaussian distributions. The fits are very good in both cases with reduced chi-squares of slightly less than 1.0. It is probable that these events were produced by an internal source such as the release of internal stresses. From the fitted gaussians we can determine the probability for each circuit to have a false monopole event, (in the high probability range of 80% to 100% of maximum signal). We expect ~1 event every 4 months of live time in the top detector circuit and every 17 months in the bottom circuit. Note however that these are worst case estimates. It is in fact possible that the monitors were also sensitive to internal disturbances large enough to produce offsets above 3.0 mV and 2.5 mV respectively in the two circuits. This would explain the sudden cut-off of signals above these levels in figure 32. In this case the rates of spurious signals are smaller than those quoted above and cannot be systematically determined from the present data. Under the assumption that the two circuits are well isolated from one another, the above spurious event rates allow us to expect a rate of less than 1 spurious coincident signal per 10^5 yr.

The net live time exposure of run 2 is 136 days. The total sensitive area for a monopole passing through either or both of the gradiometers is 2100 cm^2. The exposure of this run thus sets a 90% C.L. limit of $f_m \lesssim 7.4 \times 10^{-12}$ cm^{-2} sr^{-1} sec^{-1}.

Results and Conclusions

The combined exposures of the two periods over which the detector was operated allow us to place a limit on the flux of monopoles at $f_m \lesssim 6.7 \times 10^{-12}$ cm^{-2} sr^{-1} sec^{-1} (90% C.L.).[76] Table 11 compares this limit with limits obtained from other experiments. This limit pertains to monopoles having an integer multiple of Dirac-charges and in fact depends only upon charge. The exposure of this experiment corresponds to 215 times the exposure of the experiment by B. Cabrera[57] in which a magnetic monopole candidate was reported. The probability that these two results are compatible is less than 0.5% and consequently we are led to conclude that Cabrera's candidate event was the result of some more mundane occurrence. We have presented evidence that indicates that monopole-like events can be generated by environmental disturbances and that this background can be discriminated to a large extent by the use of monitors. Unfortunately no monitor devices were present in the first experiment performed by Cabrera.

This experiment demonstrates that fairly large superconducting detectors can be operated in easily obtained ambient magnetic fields of ~1-10 mGauss. This is achieved by careful isolation of the detector from the environment and by continually monitoring the apparatus for environmental disturbances. A final safeguard against spurious monopole-like signals is provided by operating two superconducting loops with some degree of coincident acceptance area. The detector loops are twisted gradiometer patterns having small inductive coupling to the superconducting shields in which they are enclosed which in turn allows larger area loops to be used.

TABLE 11

MONOPOLE FLUX LIMITS FROM INDUCTION DETECTORS

Detector	Averaged Area [m^2-sr]	Exposure Time [hours]	Limit (90% C.L.) [cm^{-2} sr^{-1} sec^{-1}]	Date
Chicago-Fermilab--Michigan	0.21	3,624	6.7×10^{-12}	July 2, 1984
IBM	0.10	9,100	5.5×10^{-12}	June 26, 1985
Stanford II	0.05	19,554	5.3×10^{-12}	Sept 5, 1985
Imperial College*	0.18	8,242	3.4×10^{-12}	Feb 6, 1986
National Bureau of Standards	0.12	8,523	5.0×10^{-12}	Feb 19, 1986

*One candidate event was observed in this experiment but later disregarded by one member of the group (Chris Guy). The limit shown in the table above assumes that no monopoles were observed.

In the next chapter we present the design and performance of an upgraded superconducting detector with 1.1 m diameter gradiometer loops. This detector will be seen to employ an innovation which allows gradiometers to be overlapped with no mutual inductance to obtain a high proportion of coincident detection area.

CHAPTER V

A SECOND GENERATION DETECTOR

In this chapter I present the first results from an induction detector with four 1.1m diameter gradiometer loops.[77] The detector was cooled in an ambient magnetic field of ~5-125 mGauss. Once again high field operation is made possible by closed superconducting shields and isolation from the environment.

Several factors of this experiment are special. First of all the new gradiometers apply the techniques of "distributed-parallel" and "series-parallel" layouts.[70] This allows them to be manufactured on a single side of plated circuit-board with minimal loss in coupling to the SQUID. The gradiometer pattern itself is also new. It is comprised of concentric circles with polarity alternation along the radius. By limiting the polarity changes to one coordinate direction less filament is necessary and so a larger signal is obtained. The radial cell widths are chosen to give a uniform signal for monopoles penetrating the detector along all possible trajectories. In addition we have found that gradiometers with similar patterns can be oriented to lie directly on top of one another with no inductive coupling. We call these "close-packed orthogonal gradiometers." In the experiment that will be presented in this chapter, two gradiometers are close-packed in each of two shields to obtain better than 98% efficiency in coincident detection area. This detector also uses inexpensive

piezoelectric strain gauges attached directly to detector surfaces inside the vacuum vessel in order to monitor the detector for internal vibrations.

In this chapter I present the design of the detector shield and gradiometers. The physical apparatus is described in some detail as well as the performance of the apparatus in two test runs. Finally, our results and conclusions with regard to this detector are presented.

Detector Design

Shields

The detector loops are enclosed completely by superconducting Pb shields. The shields are cylindrical with a diameter of 112 cm. The endcaps of the cylinders are spherically domed with a 4 m radius of curvature. The height of the shield cylinder thus varies between 17 cm at the cylinder walls and 24 cm along the cylinder axis. The Pb shields were formed by cold-spinning 1.0 mm thick Pb sheets on a wooden form.[69] Each spinning consists of a single continuous sheet and represents one-half of a completed shield. The preformed Pb was bonded to high-conductivity Cu which was also cold spun to mate smoothly with the Pb. The bonding was obtained with low melting point Ostalloy metal[78] which superconducts at about the same temperature as Pb.

Although the basic design, (if not the scale), of these shields is very reminiscent of our previous detector, the construction procedure described above represents a vast improvement in quality and

in ease of manufacture. The contiguous Pb sheets used in the spinning process assure a completely closed shield of uniform thickness. The difficulties of casting the shields with molten Pb, (i.e. the inability to control the thickness or to completely prevent cracking while cooling), are entirely avoided. Most importantly, the new construction process allows us to use 1 mm thick shields as opposed to 3-6 mm thick cast Pb.

Gradiometers

The net flux impinging upon a gradiometer from vortex currents in the shield is found by integrating the z-component of the field, ($B_z = -\partial V/\partial z$, where V is given by equation (2.15)), multiplied by the cell polarity (± 1), over the plane of the loops. With such a calculation the signal for the monopole can be determined, (as was discussed in some detail in chapter II). For the particular monopole trajectory shown in figure 5, the z-component of the magnetic field in the plane of the gradiometer is a smoothly varying function with maxima in the vicinity of (ρ_1, ϕ_1) and (ρ_2, ϕ_2). This can be seen clearly in the plot of figure 33. Decoupling from the shield therefore depends upon the cell widths in these regions. At least one polarity change in these regions is required to obtain flux cancellation. Calculations were performed to determine the cell widths necessary to yield better than 90% decoupling at all radii. The results of these calculations are plotted in figure 34 for various values of the ratio of diameter (2B) to height (H) for cylindrical shields with flat endcaps. The plots indicate that the cells should

diminish linearly in width near the cylinder wall. For 2B/H = 5, (corresponding to the apparatus being presented in this chapter), this is most easily accomplished by the concentric loop pattern shown in figure 35. The response function for this pattern, based on 5,000 simulated monopole events, is shown in figure 36. As expected, the response function indicates better than 90% decoupling from the shield for 97% of all monopole trajectories. The low inductance of the concentric loop gradiometer due to its minimal filament length results in more than twice the signal size that could be obtained by a square-cell gradiometer having the same decoupling from the shield.

Close-Packed Orthogonal Gradiometers

Consider a gradiometer composed of two identical rectangular cells of opposite polarity. A single rectangular loop positioned to overlap the two cells equally, (figure 37), will be insensitive to changes in the d.c. current in the cells. This is because a current in the gradiometer will produce exactly equal and opposite fields in its two loops. The net flux change in the single loop is then zero.

Using symmetry arguments one can show that for certain gradiometers shapes, large numbers of gradiometers can be designed which are mutually decoupled when overlapped, (see appendix C). We obtained orthogonality of the concentric loop gradiometers by designing the pattern to be antisymmetric in cell polarities upon reflection through a particular bisecting line (see figure 35). In this way, one gradiometer can be rotated 90° relative to the other so that any one cell in either gradiometer always symmetrically overlaps

Figure 33. Plot of z component of the trapped field. Shown is the z component of the field in the plane of the gradiometer along a radial line at polar angle $\phi = 0$ for (a) a monopole passing through the shield endcaps at $\rho_1 = \rho_2 = B/2$ and polar angles $\phi_1 = \phi_2 = 0$, (b) a monopole passing through the shield endcaps at $\rho_1 = B/6$, $\rho_2 = 5B/6$ and $\phi_1 = \phi_2 = 0$.

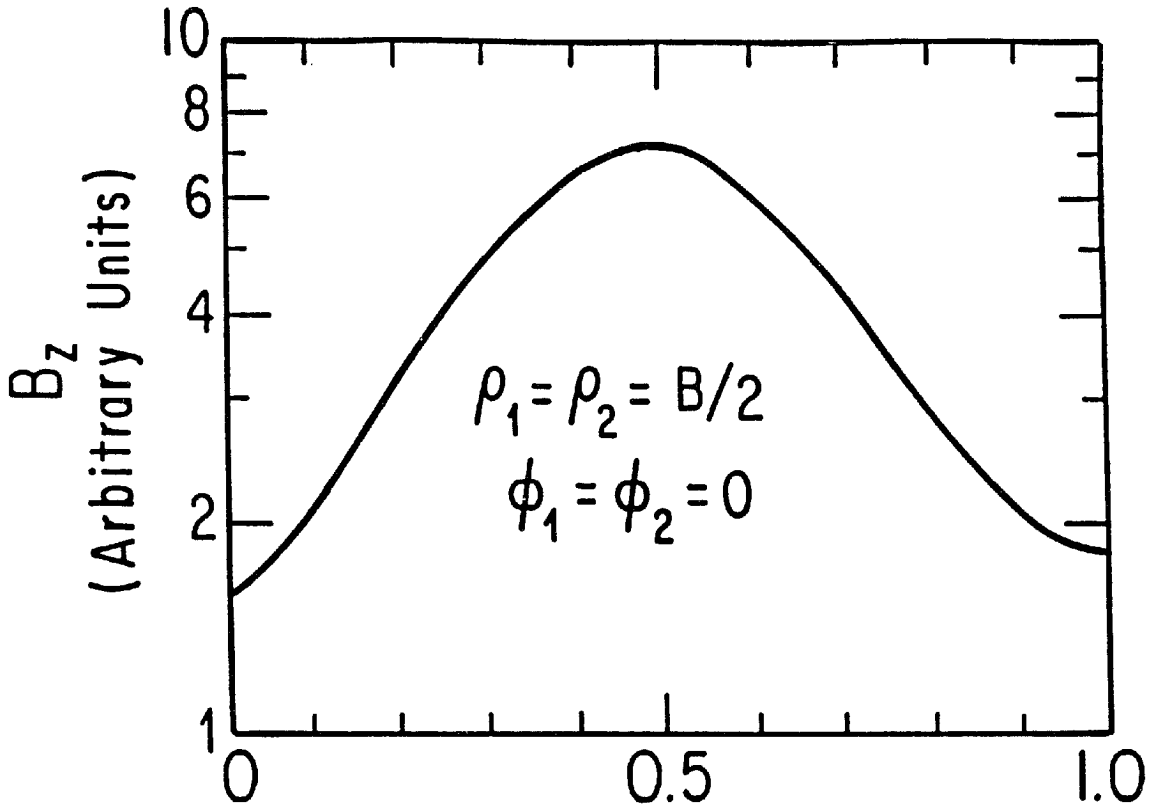

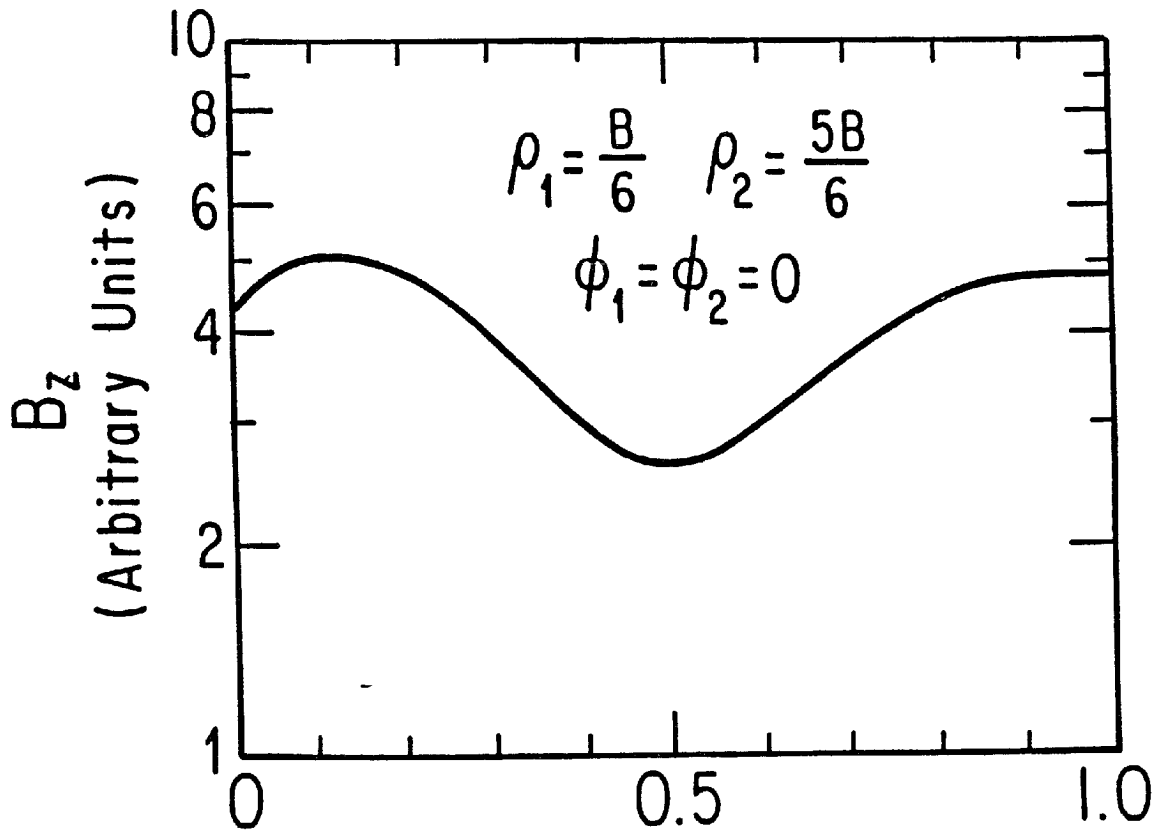

Figure 34. Cell width versus radial position for $>_{\sim}$ 90% decoupling from the shield. The cell width, (in units of cylinder height H), is plotted versus radial position, (in units of cylinder radius B), for $\gtrsim$ 90% decoupling from the shield as determined by calculation. The shields in the experiment of Chapter V have ratio 2B/H = 5.

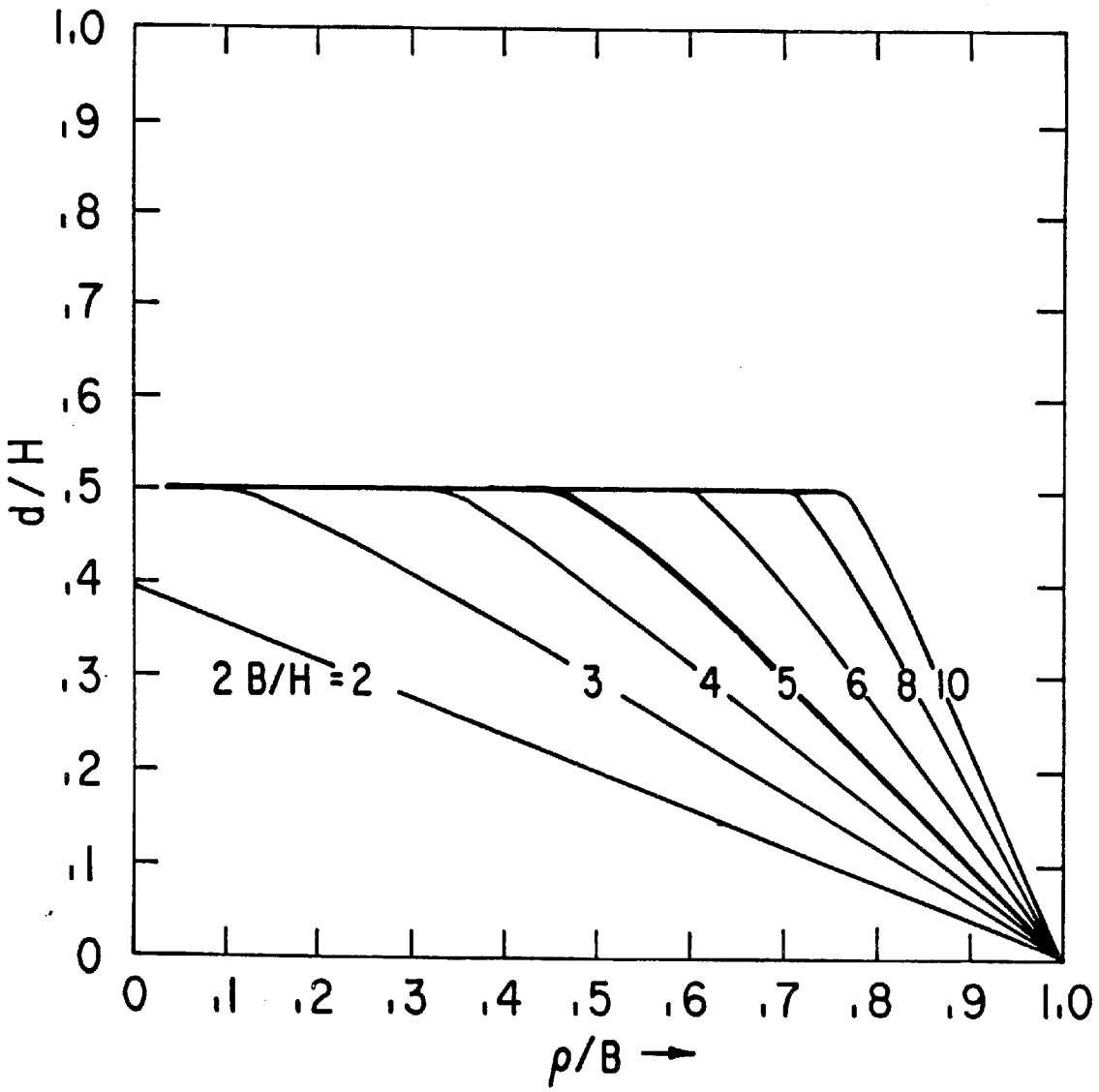

Figure 35. The 1.1 meter diameter concentric loop gradiometer. Arrows indicate a possible direction of current flow.

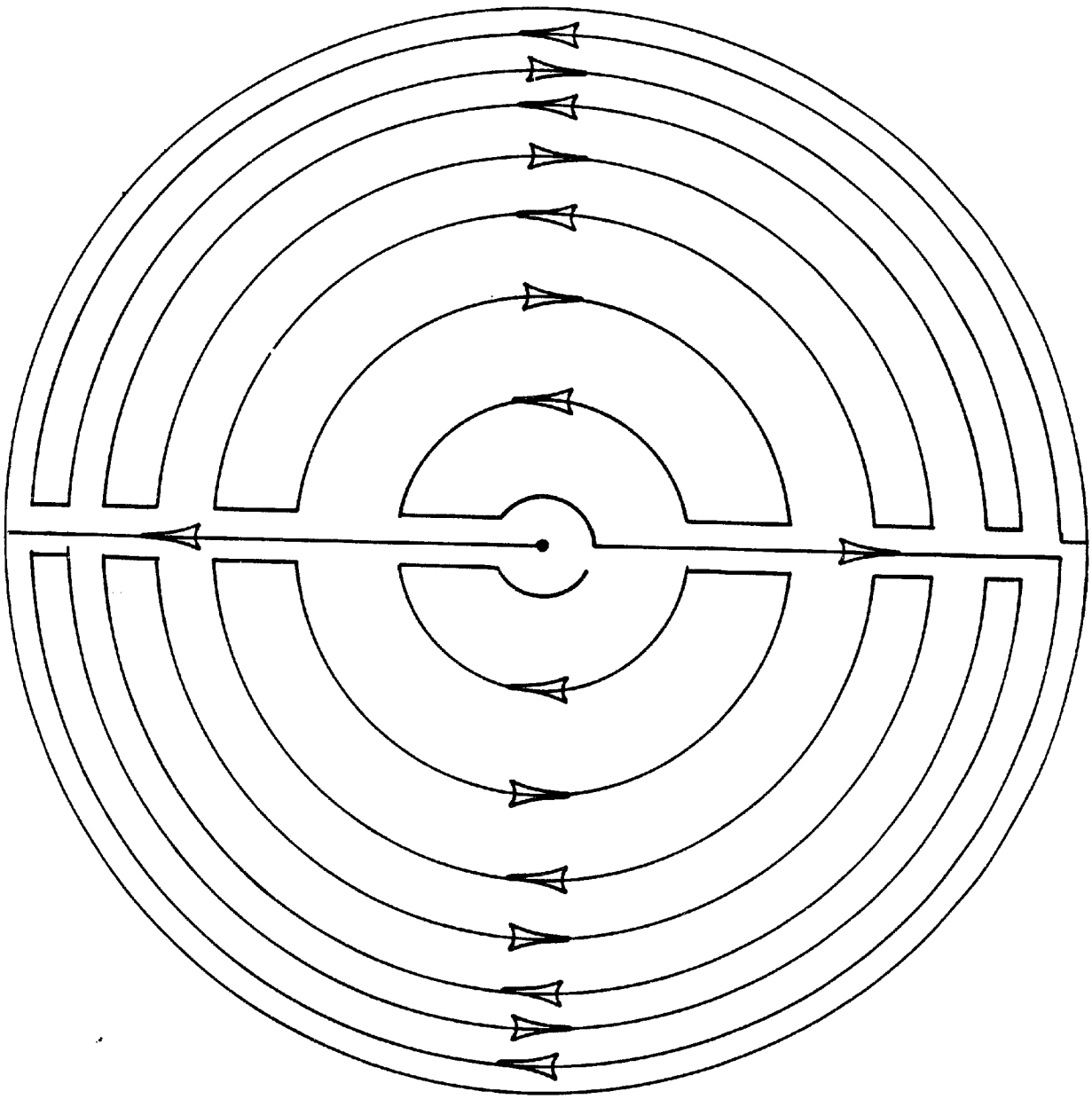

Figure 36. The response function for CFM II. The inductive coupling of the gradiometer to the shield reduces the signal by an amount which depends upon the monopole trajectory. The curve indicates the probability of a monopole producing a particular signal size and was produced by calculating the signal for 5,000 random events. The maximum signal corresponds to no inductive coupling to the shield.

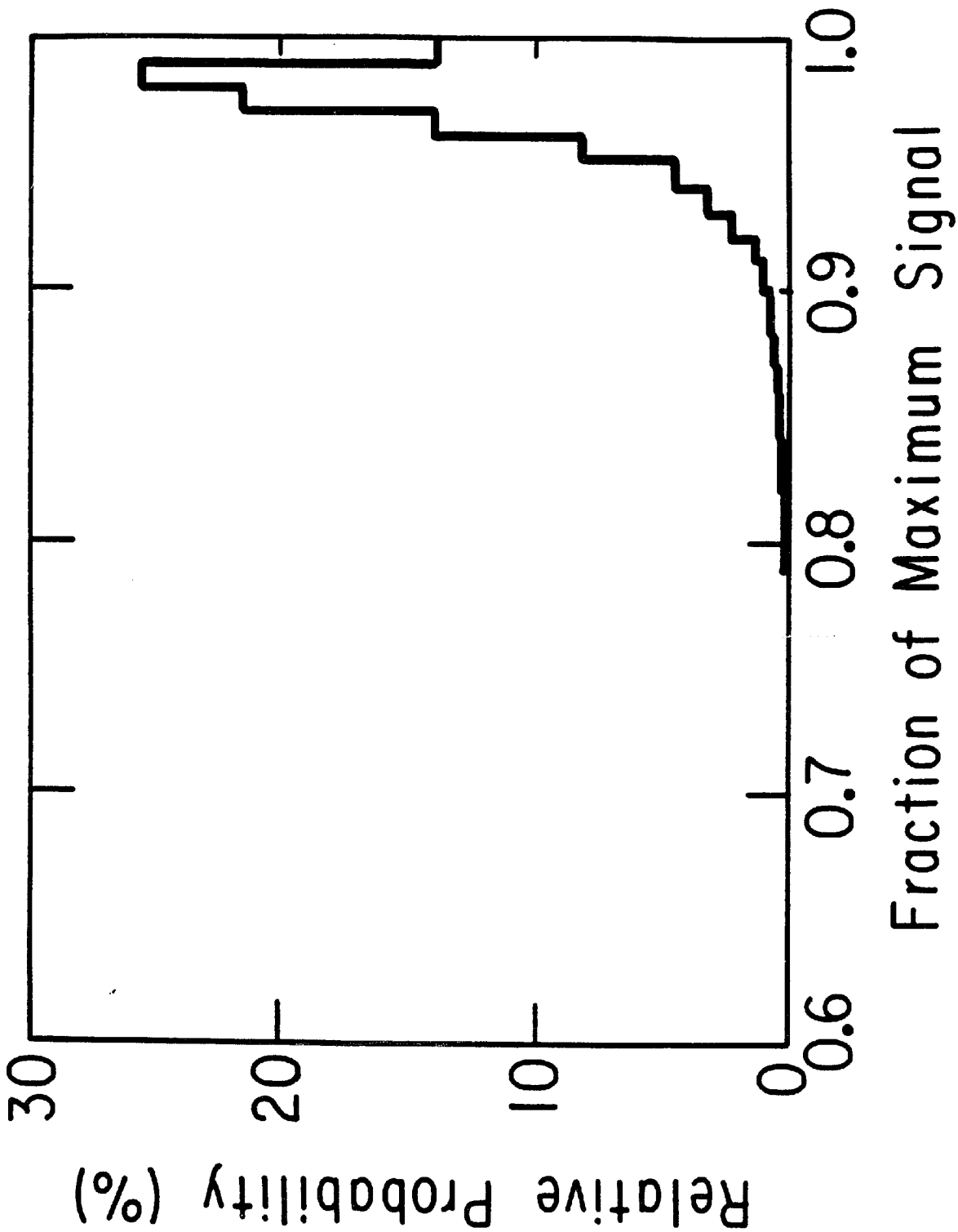

Figure 37. Overlapping of simple rectangular grids. A rectangular loop overlaps a two-cell gradiometer which is made by twisting a rectangular loop about the center. A current induced in the gradiometer, flowing in the directions indicated by the arrows, would not induce a current in the overlapping loop. This is because the field at an arbitrary point (x,y) is exactly opposite to the field at the symmetric point (-x,y). The net flux impinging upon the loop can thus be seen to integrate to zero.

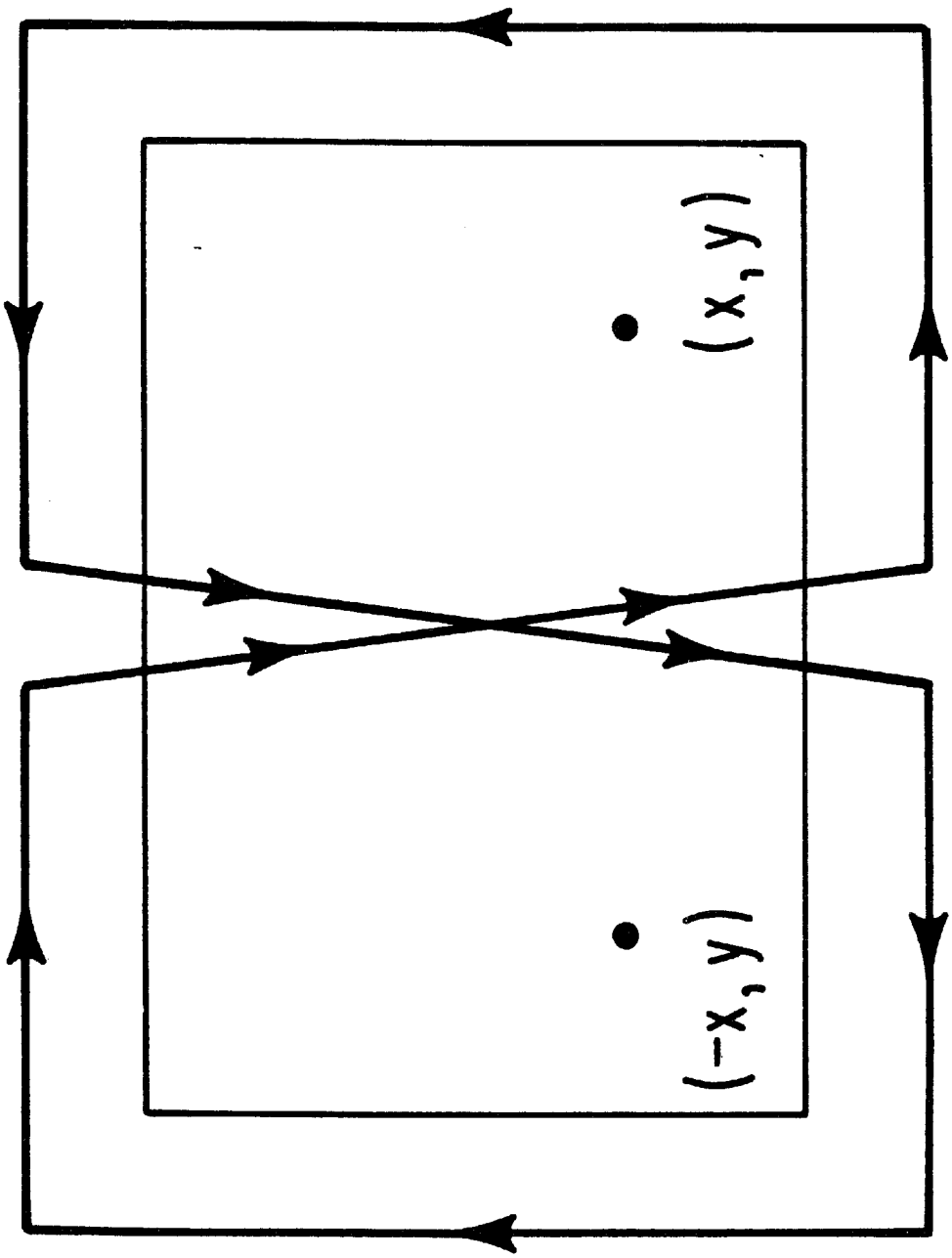

two cells of opposite polarities in the other gradiometer. Complete decoupling is demonstrated by an argument similar to that given above for the simple example of rectangular loops. In actuality, the gradiometers are separated by a 1 cm thick G-10 support disc. The separation results in ~2% loss of coincident detection area. There is an additional 5% loss in coincident sensitive area resulting from the fact that no signal is generated if a monopole passes through the superconducting filament which is .254 cm wide.

Series-Parallel and Distributed-Parallel Gradiometers

We saw in chapter III, that transformer coupling of the SQUID and detector loop is superior to direct coupling because the measured current in the SQUID coil is proportional to $L^{-1/2}$ in the former case and L^{-1} in the latter case, where L is the inductance of the detector loop. In fact we have found that gradiometer detector loops can be designed to automatically impedance-match the SQUID input coil thereby eliminating the need for a transformer.[70]

To see how this is accomplished, consider a gradiometer which has been broken up into n spatially disjoint and equivalent subsections, each with inductance L/n. The subsections can now be reconnected in parallel with each other and also with the SQUID as seen in figure 38. In this case, the effective inductance of the gradiometer, as seen by the SQUID would be:

$$L_{eff} = \frac{L}{n^2} \tag{5.1}$$

Now suppose that the magnetic monopole passes through the jth subsection of the gradiometer. Figure 39 shows the remaining subsections lumped together with equivalent inductance L/[n(n-1)] in parallel with the SQUID and the jth subsection. After a simple network calculation, we find:

$$i_{SQUID} = 4\pi g \frac{n}{(L + n^2 L_S)} \tag{5.2}$$

For fixed values of L and L_S, equation (5.2) can be maximized by a suitable choice of n. The dots in figure 40 represent the maximized SQUID current as a function of L/L_S. Figure 41 shows the effective inductance of the gradiometer for optimized n values as a function of the series inductance L, (in units of L_S). With optimized n values and in the limit as L becomes very large we find $L_{eff} \rightarrow L_S$ and also:

$$i_{SQUID} \rightarrow \frac{2\pi g}{\sqrt{LL_S}} \tag{5.3}$$

which is the same as equation (3.2) for the current in the case of transformer coupling.

We tested the series-parallel gradiometer scheme using a BTI SQUID[61] with voltage/current gain of 2.86×10^{10} V/A. Table 12 shows our results from tests done at Fermilab in February of 1984. We compared observed and expected signals for both series and series-parallel schemes using pseudopoles. The results, accurate to 5%, are in good agreement with the calculations above.

In addition to realizing that impedance matching to the SQUID can be designed into the gradiometer itself, we also found that the

Figure 38. Series-parallel circuit. A set of n gradiometers, each of inductance L/n, are attached in parallel with one another and with the SQUID input inductance L_S.

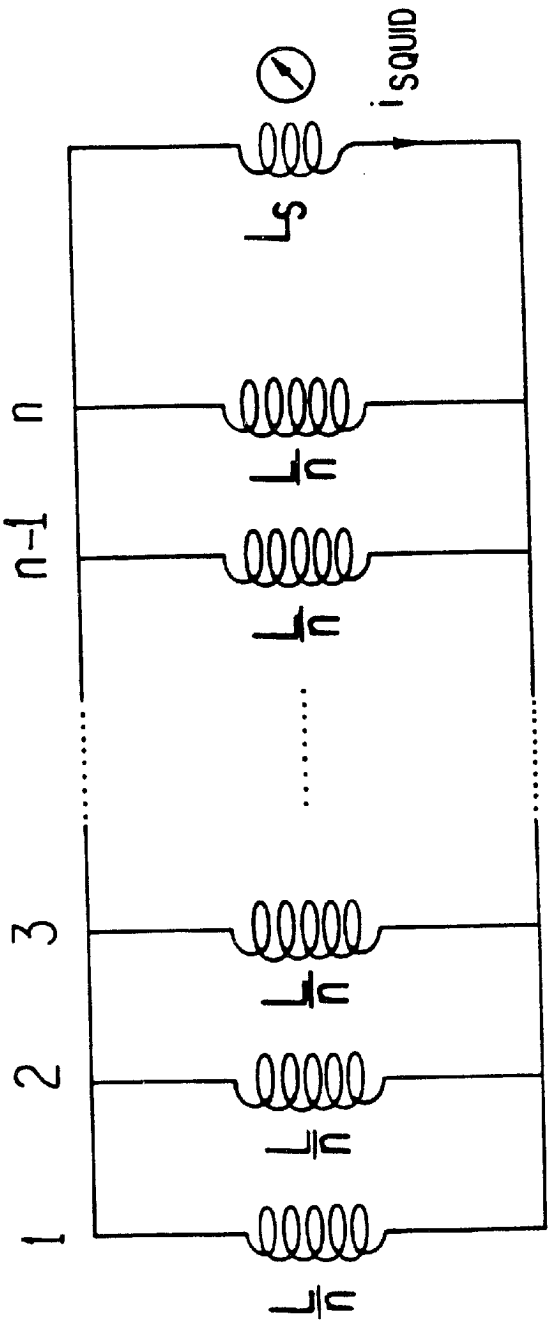

Figure 39. Equivalent series-parallel circuit diagram for the calculation of the SQUID current after passage of a monopole through the jth subsection.

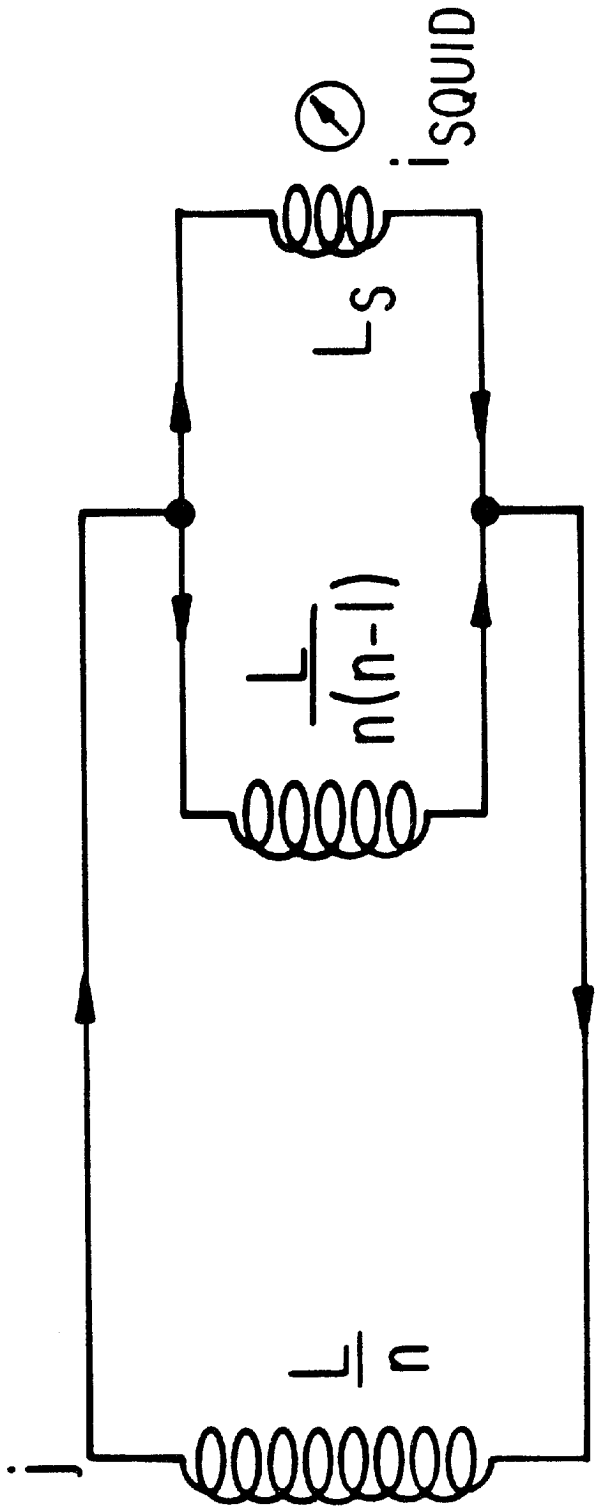

Figure 40. Plot of SQUID current versus inductance of optimized series-parallel gradiometers. The SQUID current, (in units $4\pi g/L_S$), is plotted versus inductance L, (in units of SQUID input inductance L_S), for a series gradiometer and a series-parallel gradiometer of n subsections where n is the number indicated next to the curve.

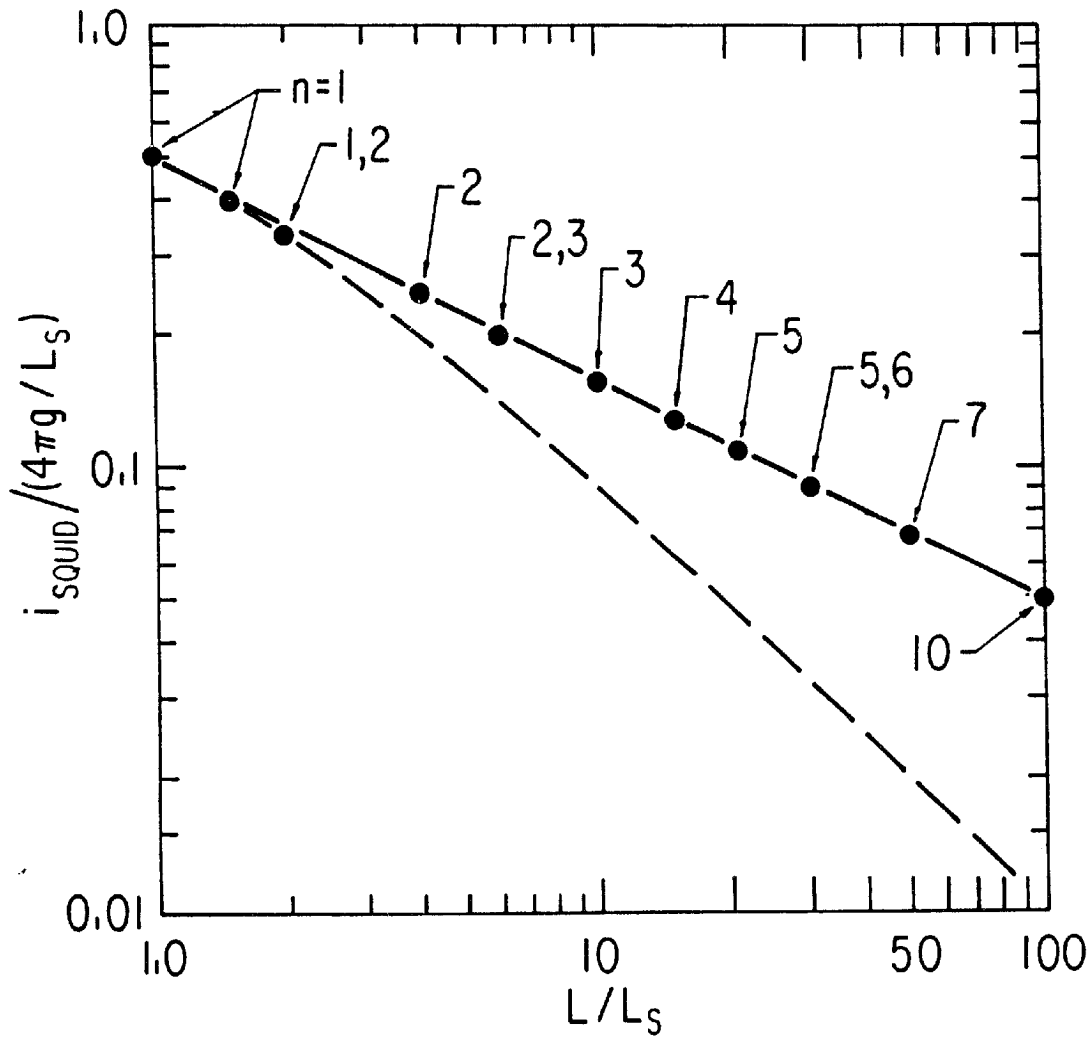

Figure 41. Effective inductance of optimized series-parallel gradiometers. The effective inductance of a series gradiometer which has been subdivided into an optimal number n of subgradiometers and reattached in parallel is plotted. Inductances are in units of the SQUID input inductance. As the inductance L increases, the optimal number of subdivisions increases and the effective inductance approaches an exact match to the SQUID input inductance.

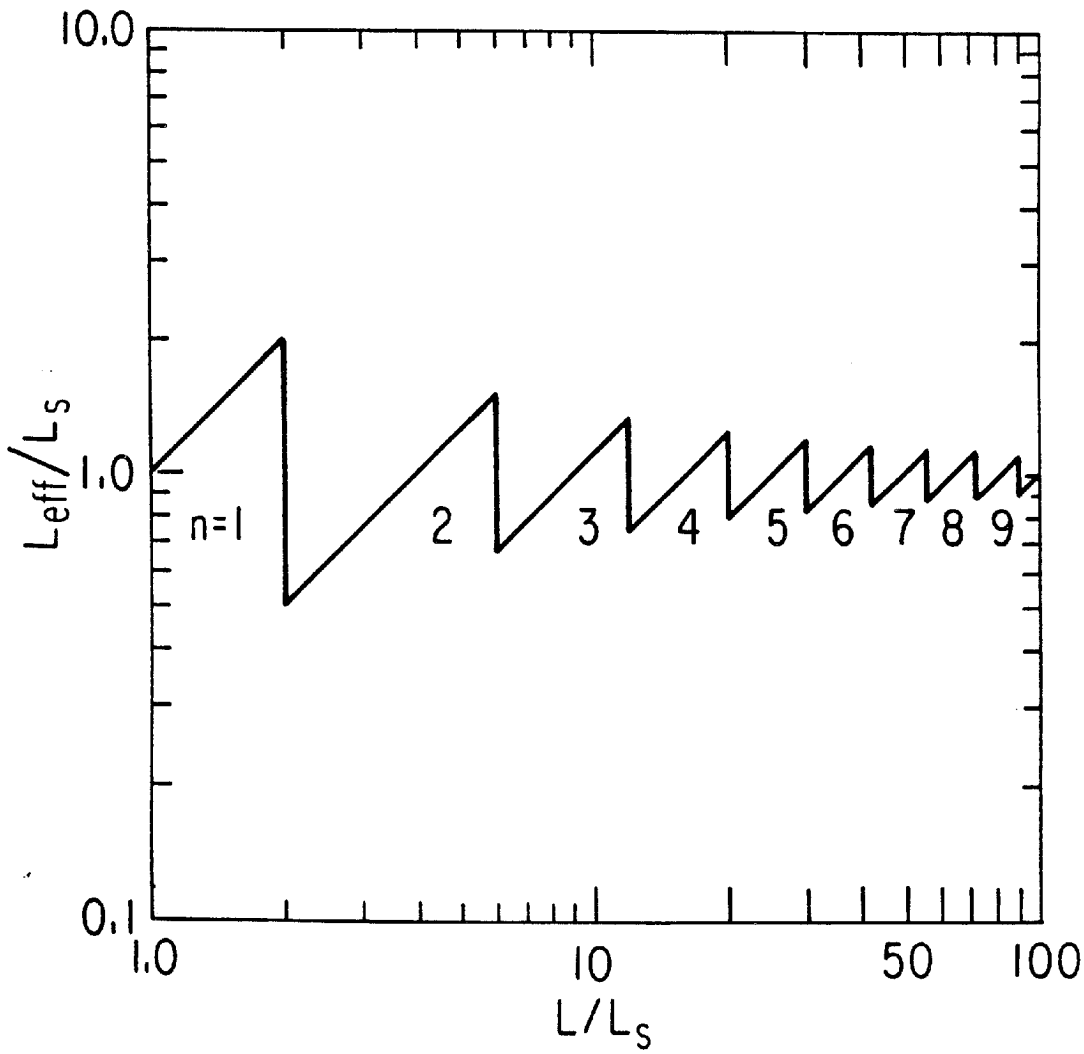

TABLE 12

COMPARISON OF OBSERVED WITH PREDICTED SIGNALS FOR SERIES AND SERIES-PARALLEL GRADIOMETERS

Type	L_s	L	$\Delta\Phi$	Predicted	Observed
Series	2.0 μH	2.26 μH	5.6×10^{-14} Wb	375 mV	370±20 mV
Parallel (n=2)	2.0 μH	0.80 μH	5.6×10^{-14} Wb	283 mV	280±15 mV

layout of the gradiometer pattern and its construction can be simplified. Previously, a gradiometer design consisted of taking a simple loop as in figure 42a, and twisting it into a pattern in which each cell is topologically closed as in figure 42b. This results in two filaments carrying current in the same direction on the border of each cell, (except on the periphery of the loop). This, in turn, requires that two-sided circuit-boards be used, (see figure 15).

An alternative scheme is to start from a configuration with two loops of opposite polarity and in parallel as shown in figure 43a. The common boundary of the loops can then be deformed to the "distributed-parallel" gradiometer in figure 43b. There is only one current element on each cell border and the pattern can be produced on just one side of plated circuit-board. Large gradiometers can be produced by connecting many such units in parallel or in series, or in any combination of the two which gives the optimum signal. The gradiometers used in the experiment of this chapter consist of two distributed-parallel gradiometers which are connected in series. We found that with regard to the series-parallel discussion above, this configuration behaves like a gradiometer which is divided into four subsections reconnected in parallel.

Description of the Apparatus

Overview

The apparatus, (see figure 44) consists of two detectors suspended in vacuum and cooled by conduction. The shielded detectors are 1.12 m diameter cylinders with spherically domed endcaps. They

Figure 42. Standard gradiometer obtained from a simple loop by twists. A gradiometer (b) is obtained from a simple loop (a) by twisting so that there are two filaments on each boundary between two cells.

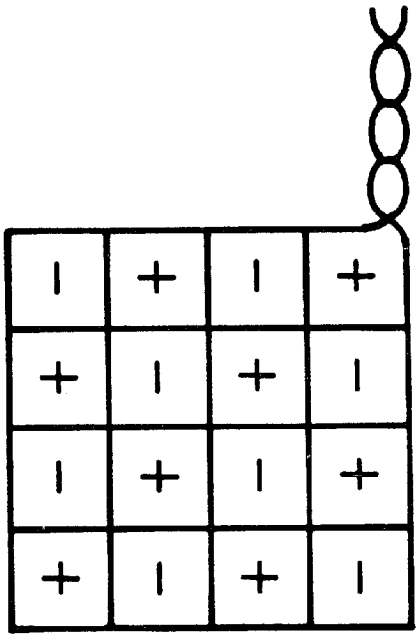

(b) Gradiometer

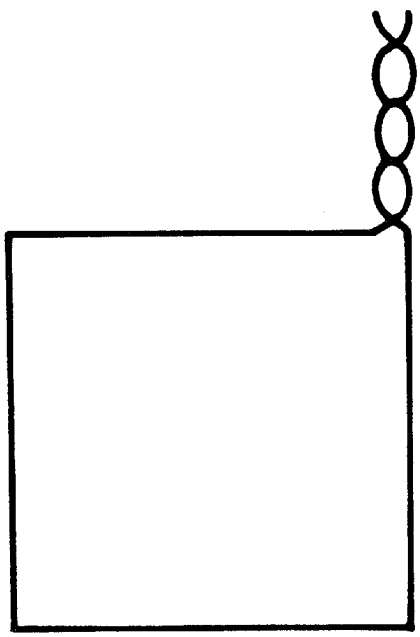

(a) Simple Loop

Figure 43. Distributed-parallel gradiometer formation. In the distributed-parallel scheme a simple loop (a) is bisected by a filament to which the SQUID is attached creating regions of opposite polarity with respect to the SQUID. The bisecting filament can be continuously deformed (b) to redistribute the different polarity regions in a gradiometer pattern.

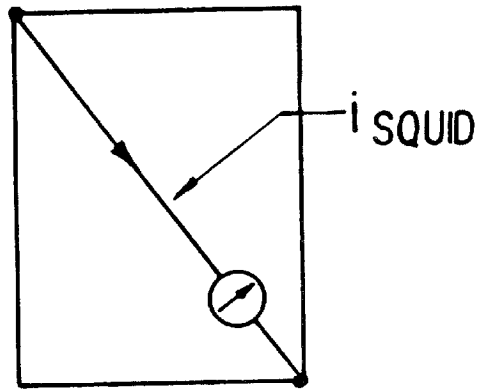

(a) Two Loops in Parallel

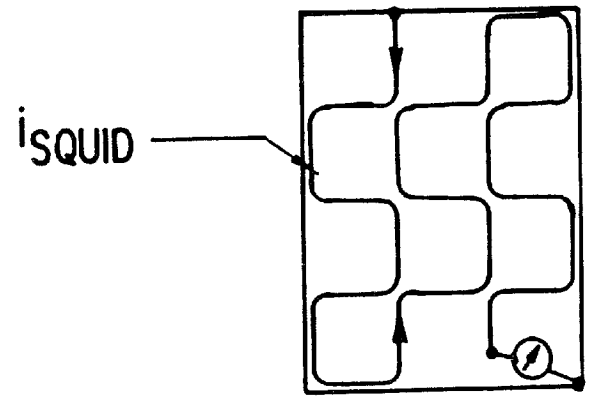

(b) Distributed Parallel Gradiometer

Figure 44. CFM II apparatur. The detector apparatus for the 1.1 m diameter overlapped gradiometers is shown and special features, discussed in Chapter V, are highlighted.

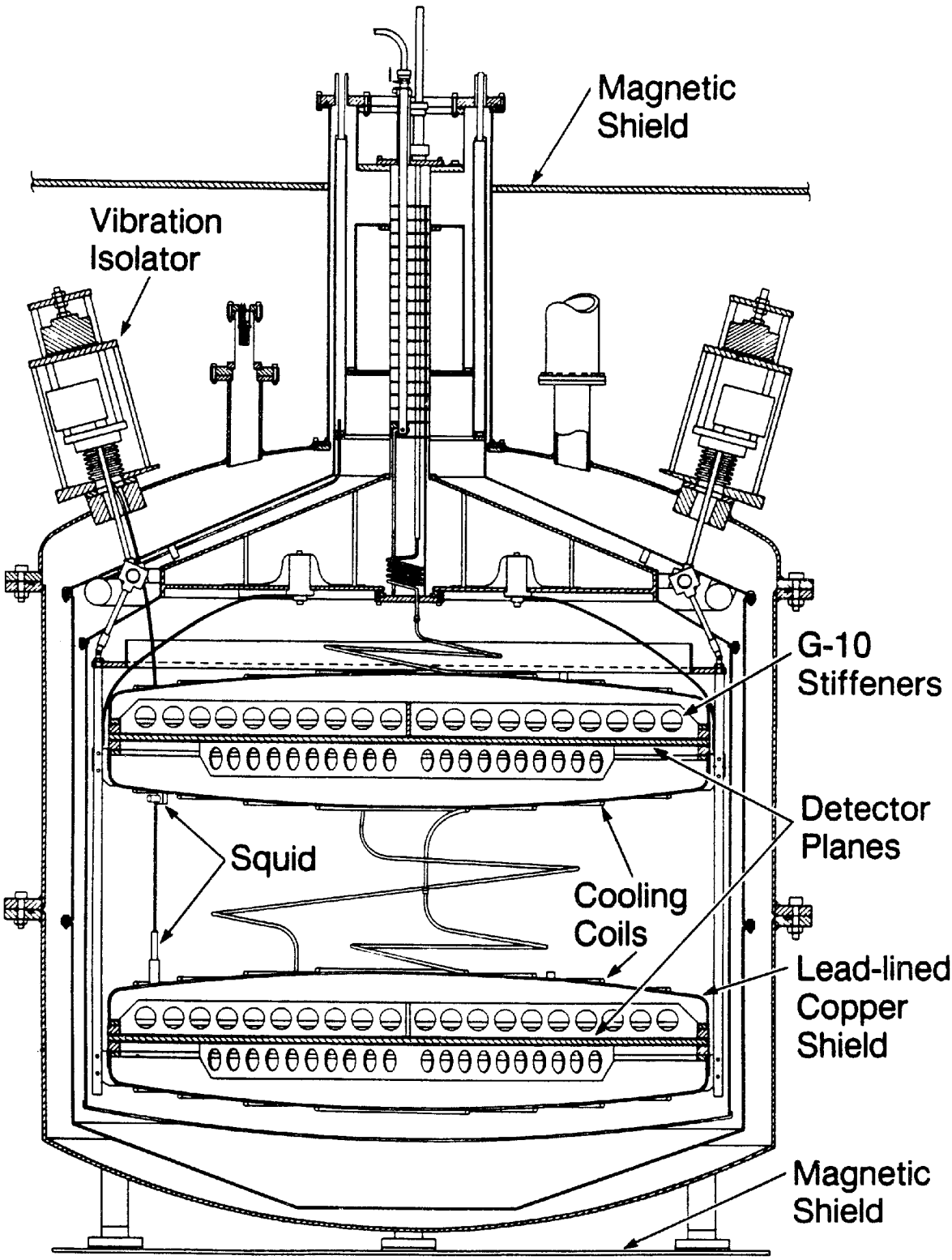

are completely surrounded by thermal radiation and magnetic field shields. The radiation shields have diameters of 1.20 m and 1.23 m and are maintained at nominal temperatures of 4.2°K and 78°K respectively.

The vacuum vessel is made up of three pieces and has a total volume of 1,800 l. It is essentially the same as in the last experiment (chapters III and IV) but with a middle section added for vertical enlargement. A 70 l LHe reservoir and a 30 l two-part LN reservoir are also contained in the volume. The vessel is partially enclosed by the open steel pipe described in chapter III which is again used for crude shielding from the earth's magnetic field.

Gradiometers, Superconducting Shields and Pseudopoles

The gradiometers are again fabricated as conventional solder-plated circuit-boards in which standard 60-40 solder is used as the superconducting filament. The size of the gradiometers made it necessary to construct them by adjoining four circuit-boards. Several junctions were made between the boards to complete the circuit.

To inhibit vibration, the two gradiometers in each detector are strapped to opposite sides of a 1.0 cm thick G-10 disk for rigid support. Additional stiffening is provided by G-10 cross-braces captured by G-10 hoops at the perimeter of the assembly. The cross braces and support disc have patterns of holes cut in them to reduce their mass by 70%. The gradiometers and support assembly are tightly fitted into cylindrical Pb shields with spherically domed endcaps.

The top detector has 8 pseudopoles used to calibrate the response of the detector for arbitrary monopole trajectories and to measure the inductive coupling of the overlapped gradiometers. The bottom detector has 4 pseudopoles. By comparing the response of the bottom detector pseudopoles with those for similarly positioned pseudopoles in the top detector, the overall response of the bottom detector can also be determined.

SQUIDs

Each of the signals from the 4 gradiometers is continuously monitored by an rf (radio frequency) biased SQUID.[61] The SQUIDs are mounted directly onto the shielded detectors. The leads connecting the SQUIDs to the rf heads pass from vacuum to atmospheric pressure by means of vacuum feed-through connectors on vibrationally isolated suspension devices where the rf heads are attached. The superconducting leads from each gradiometer pass through the shield to their corresponding SQUID by means of a hole in a Pb block to which the SQUID is mounted. This completes the magnetic shielding of the superconducting detector circuit.

There are several important advantages to the SQUID mounting discussed above. Primarily, this scheme assures that the SQUIDs, rf heads, and shielded gradiometers - which together comprise the principle components of the detector - are all part of the vibrationally isolated system. Thus, relative motions of the pieces are greatly reduced. Also, by placing the SQUIDs in vacuum, the vibration encountered in a bath of liquid helium is avoided. An

equally important consideration is that by placing the SQUIDs and signal leads inside of the closed aluminum vacuum vessel, the system is much less susceptible to rf interference. The 4.2°K radiation shield, which is solder-coated to superconduct, also provides shielding from low frequency magnetic fields.

To use the SQUIDs in this way, several modifications of the commercial design were necessary. In particular, 0.15 cm diameter flexible stainless steel tubing was used to shield the copper leads between the rf heads and the SQUIDs. In two places this tubing was then replaced by 15 cm lengths of 0.30 cm diameter copper tubing. The flexible tubing was necessary to enable the leads to follow the circuitous pathways between the rf heads and the SQUIDs in the final assembly. The copper tubing segments are needed to cool the copper leads from 300°K at the rf heads to sufficiently low temperatures at the SQUIDs so as to maintain the latter superconducting. The heat-sinking of the leads was achieved by filling the tubes with low vapor pressure grease[79] and connecting the copper sections to cold surfaces with high-conductivity copper straps. The length of the copper tubing sections was chosen to compensate for the low thermal conductivity of the grease.

Detector Cooling

The total mass of the detectors is ~230 kg. To cool this mass quickly and efficiently we hard-soldered a coil of 1 cm diameter hollow copper tubing to the copper shells of the detectors. Helium gas can be circulated through the coil, passing first through a heat

exchanger immersed in cryogenic fluid, and then to the detectors to absorb heat. The gas can then be vented to atmosphere or cycled again through the coil.

When the detectors have reached stable minimum temperatures, the cooling tubes are evacuated and sealed. The detector is maintained at these temperatures by conducting heat to the liquid helium reservoir via flexible copper straps.

To maintain ~4.2° K operating temperatures, the detectors must be shielded from 300°K thermal radiation. To this end they are completely surrounded by conducting surfaces maintained at 4.2°K and 78°K. The shields are cooled by conduction to the LHe and LN reservoirs respectively. To reduce the heat load on the cryogenic liquids the shields are wrapped in multiple layers of thermally insulated, highly reflecting aluminized mylar.

Vibration Isolation and Environmental Disturbance Monitors

The detectors are suspended with copper rods attached to a G-10 ring. The ring is suspended by 6 hollow G-10 tubes from a stainless steel ring. This load ring is in turn connected at 3 points to hollow G-10 rods which attach to flanges on the exterior of the vacuum vessel. The flanges are vibrationally isolated from the vacuum vessel by means of flexible bellows and critically damped inflatable cushions.[80]

In spite of the vibration isolation just described, some mechanical disturbances may still be transmitted to the detectors or

initiated by the relief of stresses in the detectors themselves. In this experiment 8 piezoelectric strain gauges[81] were used to monitor these disturbances. Four of the gauges were clamped to the SQUID lead tubes, two were placed on the copper shells of the detectors and two were attached to the 4.2°K radiation shield. We found that the 115 kg detectors were the quietest objects in the apparatus. The SQUID lead tubes were therefore clamped to the detectors. In this configuration we found the SQUID signals were fairly insensitive to induced vibrations in the SQUID lead tubes (see figure 45).

Magnetic field, rf radiation, and liquid nitrogen fill-system pressure were also monitored as sources of spurious signals. Because of the improved vibration monitoring in this experiment the sound level meter was not used.

Reduction of Ambient Magnetic Fields

The detectors and superconducting shields were cooled below the superconducting transition temperature in an average magnetic field of 35 mGauss which ranged from a minimum of 5 mGauss to a maximum of 125 mGauss. This is roughly 10 times the field of our previous experiment. To reduce the ambient field to this level we once again used currents in the coils wrapped around the steel pipe surrounding the vacuum vessel. We calculated an optimum current setting in the coils which minimizes the average field at the detectors by linear extrapolation from field values for current settings of ±0.5A and 0.0A in each of the 3 coils. This current setting was established during cooldown. During the superconducting transition, a fraction of this

field may be expelled from the detector region while the remainder is trapped at pin sites in the shields. The magnitude of the pinned field was not measured. The wide range of field values, and the consequent large average field, is due to the fact that we cannot zero out the field over such a large area given the size of our present steel shield.

Data Acquisition

Data from the SQUIDs and monitors were continuously recorded by an 8 channel chart recorder. Data could also be written to computer tape after being digitized by a 32 channel ADC. The results of this experiment are based on an analysis of the strip chart recordings.

Test Runs and Detector Performance

The detector was cooled down for the first time in April of 1985. All four SQUIDs were found to be operating and the pseudopoles indicated an adequate signal size for a single Dirac-charge monopole. The inductive coupling of the close-packed gradiometers was also measured. Unfortunately, loose SQUID lead tubes caused the signals to be too strongly affected by vibration to allow a monopole flux measurement. The run was terminated to fix the vibration problem and to repair a vacuum leak.

A second cooldown was begun in August. One SQUID for the top detector did not operate due to a change in heat-sinking which caused it to warm above the superconducting temperature. In addition, a new

Figure 45. Vibration sensitivity test data for CFM II. The two SQUID signals for the bottom detector unit are shown. The topmost channel is the summed signals of 6 strain gauges. Repeated tapping at various positions on the apparatus, including the vibration isolation suspension mounts, is seen not to affect the signals from the detector circuits.

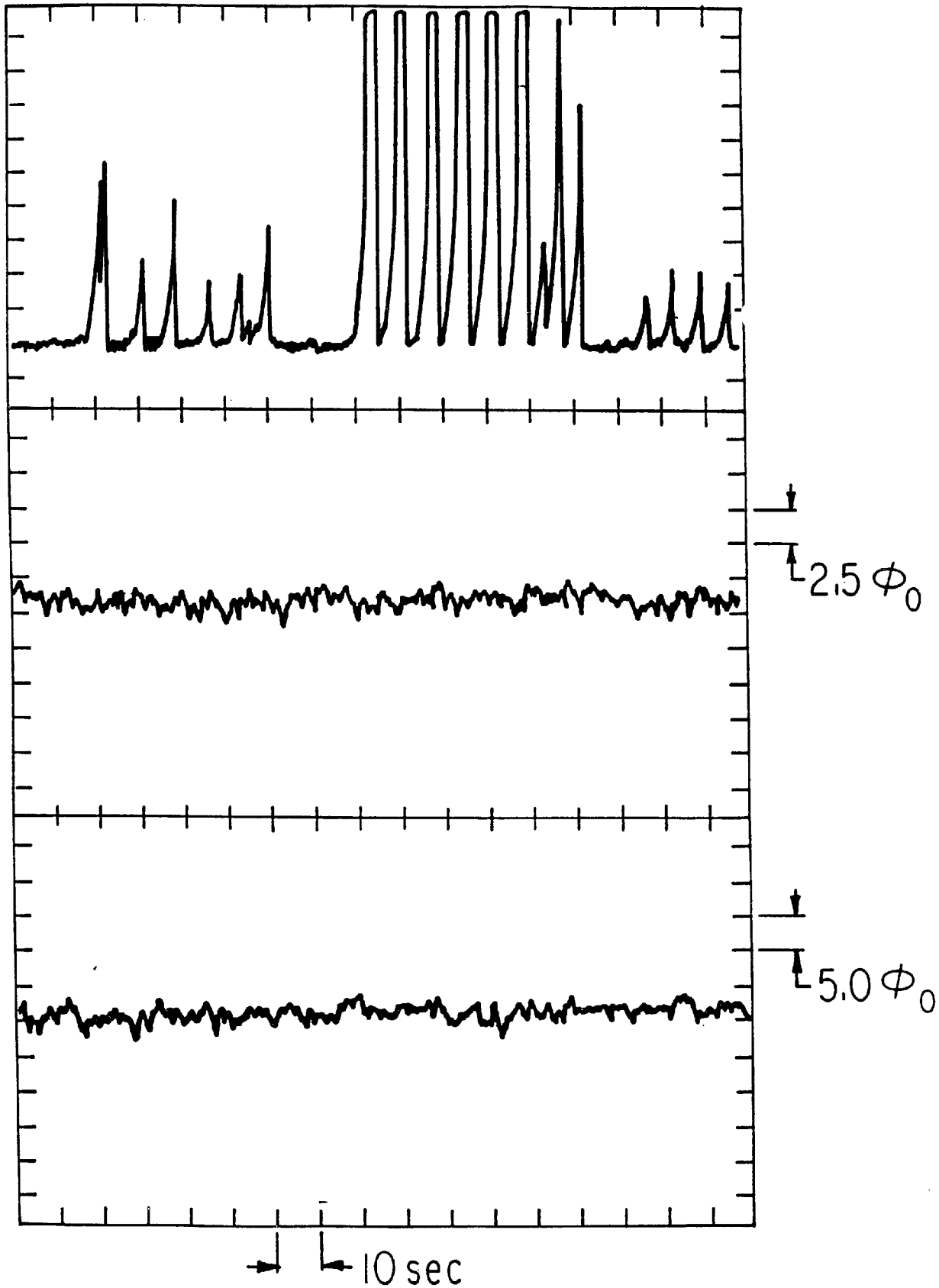

vacuum leak developed leading to a high rate of LHe consumption. However, we found that the vibrational sensitivity of the operating SQUIDs had been dramatically reduced by clamping the lead tubes to the detectors. The bottom detector could therefore be used to detect monopoles unambiguously and was operated over a period of 12 days after which the detector was warmed up to repair the vacuum leak.

Decoupling of Overlapped Gradiometers and Detector Signal Size

To measure the coupling of the overlapped gradiometers, two pseudopoles were positioned to penetrate a single cell in one gradiometer and two cells of opposite polarity in the other.[82] By the symmetry of their placement, the stimulation of the pseudopoles leads to $6\phi_o$, (or $60\phi_o$ depending on the excitation current), of flux in one gradiometer and none in the other. If the gradiometers are truly decoupled, the stimulated pseudopoles will then induce a current in only one gradiometer. Any coupling, on the other hand, would reduce this current while producing a corresponding non-zero current in the other gradiometer. From a series of repeated measurements of the signals induced in the gradiometers, (figure 46), the inductive coupling was determined to be less than 1%.

The signal sizes for trajectories at various radii were measured by stimulating pseudopoles positioned at these radii. The induced signals were found to lie within a 5% range as expected, (cf. figure 36). The maximum signal size for a single Dirac-charge monopole varied between 3.5 mV and 4.2 mV[83] for the four gradiometers

as a result of variation in SQUID sensitivities. The d.c. offset of the SQUID signals was found to drift by less than ~1.2 mV/hr. With a low pass filter of 1 Hz, an a.c. noise component of from 3-6 mV pp was also measured. At 0.1 Hz filtering the voltage signal to noise ratio was between 6 and 10 to 1. The a.c. noise component is believed to be due to the large amount of trapped flux in the SQUID and/or because the SQUIDs are being operated at temperatures too near to their critical superconducting temperature. Nevertheless, the d.c. offset corresponding to a monopole is clearly visible and unambiguous.

Sensitivity to Environmental Disturbances

Vibrational sensitivity was measured by tapping the apparatus at various places. Impulses could be imparted to the detectors and SQUIDs by tapping the isolation devices to which the detector suspension rods and the SQUID lead tubes are attached. For tapping at all positions, the signals from the bottom detector were unaffected (see figure 45). (Prior tests, completed before the SQUID tubes were clamped, induced signals as large as ~$50\phi_o$.)

Sensitivity to external magnetic fields was measured by circulating 400 mA currents in the coils on the steel pipe surrounding the apparatus. The bottom detector signals varied by less than $2\phi_o$ for field changes of about 50 mGauss. (This represents an increase in shielding power of two orders of magnitude as compared with the experiment of chapters III and IV.) The top detector showed roughly 20 times this sensitivity. The detectors themselves are adequately shielded. We believe the remaining sensitivity to external magnetic

Figure 46. Gradiometer coupling data for CFM II. The $30\phi_o$ signal for each of two separate pseudopoles is measured simultaneously in each gradiometer. Both pseudopoles are then excited repeatedly. As expected, the steady-state signal is negligible in one gradiometer and doubled in the other.

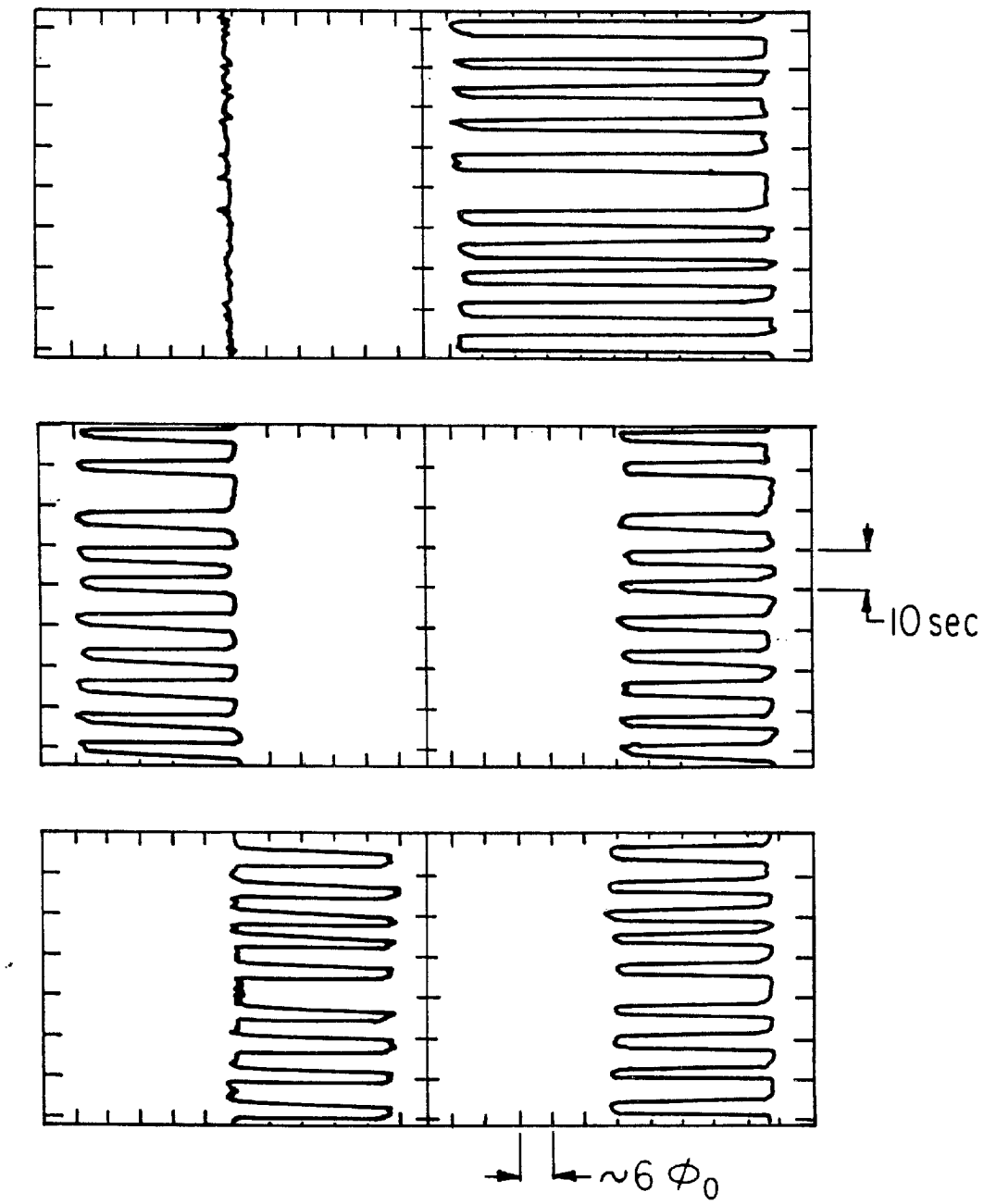

field is in the SQUIDs themselves, which can easily be shielded. The reduced sensitivity of the bottom detector was obtained by wrapping the SQUIDs for this detector in 0.1 mm thick Pb foil that extends roughly 10 cm along the SQUID lead tubes from the end of the niobium SQUID casing.

Results and Conclusions

Chart recorder data from 12 days of operation of the bottom detector were scanned for monopole-like signal offsets. Live time corresponded only to those periods when no work was being done on the apparatus and no cryogenic fluids were being transferred. In addition, we demanded that both gradiometers in the functioning bottom detector be sensitive and that all monitors be operating. A live time sample of 161 hours was thus accumulated. A monopole candidate event for the detector would correspond to coincident signals from the two gradiometers which are in the high probability response region (0.8-1.0 of maximum signal - see figure 36). The monitors must also indicate that no environmental disturbance is occurring at this time. No such monopole candidates were observed.

Single d.c. offsets observed in the two circuits which do not correlate with disturbance monitor signals are histogrammed in figure 47. In one of the two circuits (figure 47a) the typical a.c. noise is ~5 mV pp and consequently offsets below ~3.0 mV cannot be counted at full efficiency.[84] Similarly the a.c. noise level in the other circuit is typically ~3.0 mV pp and so offsets below ~1.5 mV could

not be included in the figure. There were no coincident offsets observed.

In the absence of coincident offsets we use the data for single offsets in the two gradiometers to estimate the rate of spurious monopole events due to accidental coincidence. In the noisier circuit there is one offset of ~3.7 mV which is consistent with the signal size expected for a monopole. From this one spurious signal in 161 hours we obtain a spurious monopole rate[85] of $\nu_a \lesssim 6.6 \times 10^{-6}$ sec^{-1} at the 90% C.L. for this circuit. The absence of such signals in the other circuit allows us to place a limit on the rate of false monopole events at $\nu_b \lesssim 3.9 \times 10^{-6}$ sec^{-1} (90% C.L.), for this circuit. At a 1.0 Hz sampling rate it then follows that the rate of accidental coincidence of monopole size offsets is $\nu \lesssim 6.0 \times 10^{-11}$ sec^{-1} (90% C.L.) or less than one every 500 years.

The total coincident area of the single operating detector unit, with two close-packed orthogonal gradiometers, averaged over all angles is 0.440 m^2. The exposure enables us to set a limit on the flux of cosmic ray magnetic monopoles, $f \lesssim 7.1 \times 10^{-11}$ cm^{-2} sr^{-1} sec^{-1} (90% C.L.). At this point the detector was warmed up to fix the vacuum leak. Although this flux limit is less stringent than the recent measurements of J. Incandela et al.,[76] A.D. Caplin et al.,[86] S. Bermon et al.,[87] M.W. Cromar et al.,[88] and B. Cabrera et al.,[58] each of which is in the 6×10^{-12} cm^{-2} sr^{-1} sec^{-1} region, the detector unit represents a larger detection area by a factor of 2.2, 2.8, 3.9, 4.7, and 9.4 respectively, over the detectors used in these previous experiments.[89]

Figure 47. D.c. offsets in the two overlapped gradiometers after all cuts. Histograms of the d.c. offsets in each of the two overlapped gradiometer circuits during 161 hours of live time are shown. Only those offsets which do not correlate with environmental disturbances are shown. In both cases the maximum signal is expected to be ~4.2 mV for a single Dirac-charge monopole. No coincident offsets were observed.

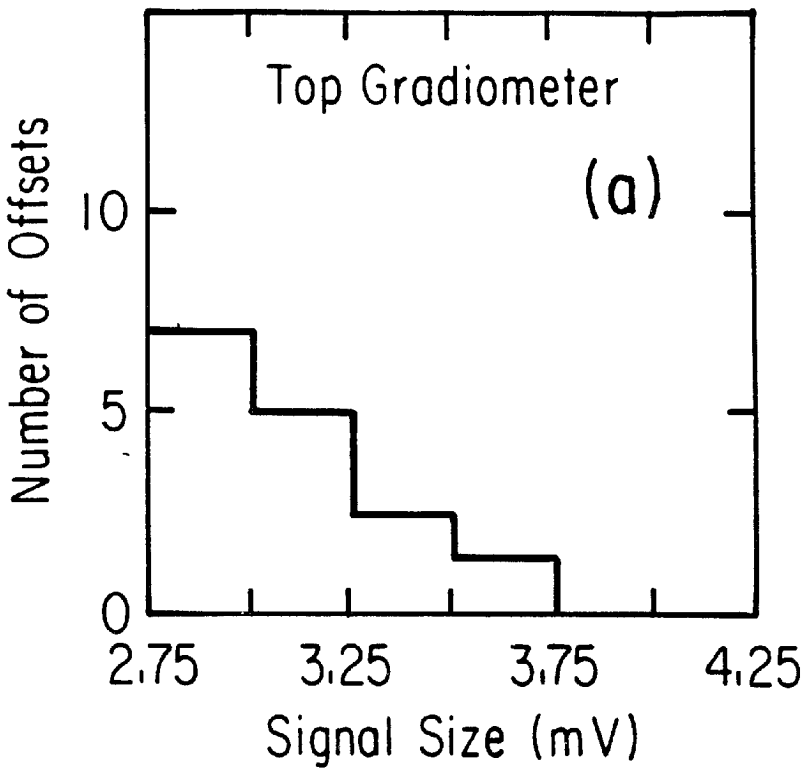

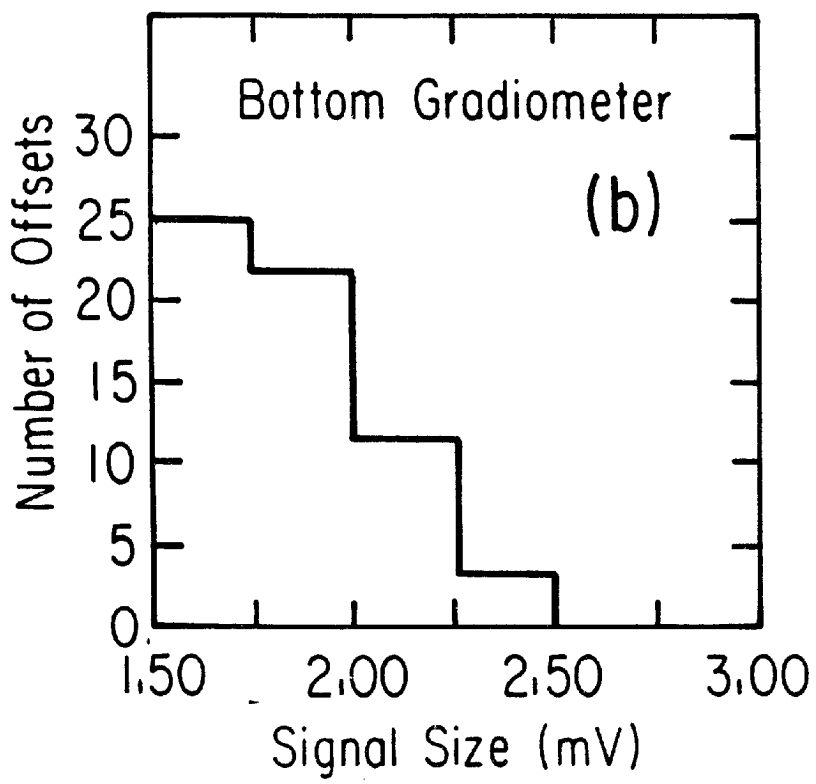

We conclude from the test runs of this apparatus that induction detectors with gradiometer loops in excess of 1 m diameter per SQUID can be constructed and operated in magnetic fields as high as 125 mGauss. Furthermore, we have demonstrated that by means of close-packed orthogonal gradiometers, high redundancy of signal can be obtained without increasing detector volume. The detectors used in this experiment are inexpensive and simple to construct and could be replicated as the subunits of a large planar array sensitive to a monopole flux at the Parker bound.

EPILOGUE

Our research, as presented in this thesis, has fulfilled our main goals as outlined in the forward. Our flux measurement, (presented in chapter IV), corresponds to 215 times the exposure of the Stanford I experiment, and the complete absence of candidate signals in this exposure thus casts a long shadow of doubt upon the Stanford candidate. (Cabrera now believes that the latter was the result of shifting trapped flux in the SQUID used to monitor the detector loop supercurrent.) Furthermore, the innovations in gradiometer design and the close-packed orthogonal gradiometer scheme presented in chapter V have made it possible to build 1.1 m diameter detectors with high redundancy that can be operated in high ambient magnetic fields. Consequently our second goal of developing a robust submodule for a large planar array is largely achieved. From our experience with induction detectors we believe it is now possible to contemplate the construction of a 1000 m^2 induction detector capable of measuring a monopole flux at the Parker bound[32] in 1 year of operation. The detector units of chapter V, for instance, if modified slightly to reduce the rate of spurious monopole signals, could be replicated as the subunits of a larger planar array of this kind.

As presented in chapter V, the rate of spurious monopole events for the 1.1 m diameter detector unit with area of ~0.5 m^2, (averaged over solid angle), is on the order of one event every 500 years. In order to construct a 1000 m^2 array, 2000 of these detector units would be required so that the rate of spurious monopole signals for the

Figure 48. Hypothetical large area detector. A hypothetical large area monopole detector is depicted in which submodules containing overlapped gradiometers are arrayed side by side in long cylindrical cryostats. The detector is shown installed in the old accelerator building of the Enrico Fermi Institute.

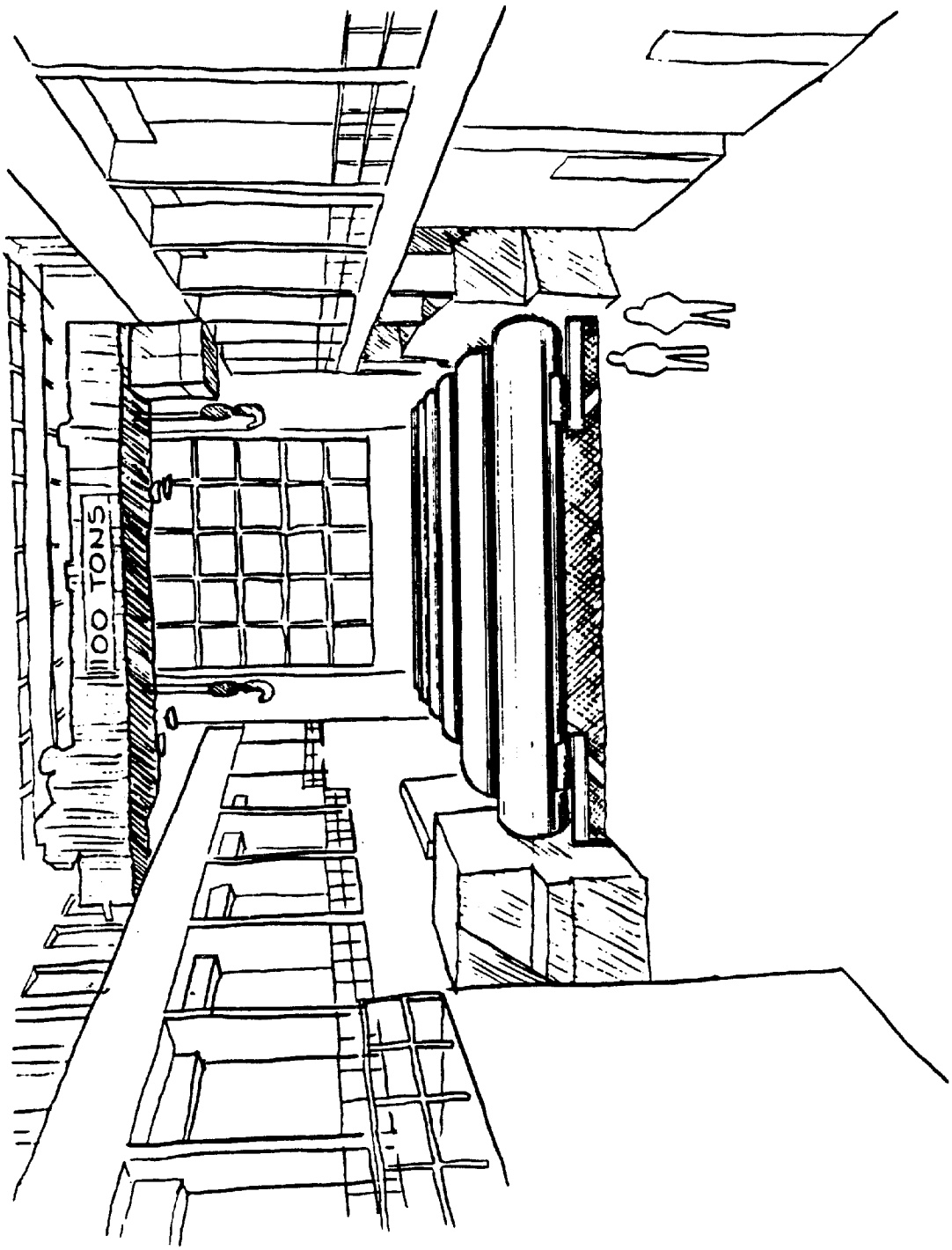

entire array would be ~4 per year. Thus a flux at the level of the Parker bound could not be measured. It is possible however that this accidental rate could be reduced by as much as 2 orders of magnitude by cooling in lower magnetic field. Our 0.6 m diameter detectors, for instance, were cooled in ~1-10 mGauss fields and had a rate of accidental coincidence of monopole signals less than 1 per 3×10^5 years.[90] Even without a reduction of the field, the rate of spurious monopole signals can be drastically reduced by using more than two close-packed orthogonal gradiometers in each detector unit. For an accidental rate of monopole size offsets per gradiometer as high as $\nu_1 \sim 6.6 \times 10^{-6}$ sec^{-1}, as presented in chapter V, the rate of accidental triple coincidence at 1.0 Hz sampling rate is $\nu_3 \sim 3.0 \times 10^{-16}$ sec^{-1} or one event every 100,000,000 years. For a 1000 m^2 array, this translates into one spurious monopole event every 100,000 years which is more than adequate to measure a monopole flux at or below the Parker bound.

Large area detectors could be constructed cheaply by cooling many detector units side by side in very long cylindrical dewars. A large area array might then look something like that shown in figure 48.

It is unfortunate that we did not detect any of these wonderful particles. Their significance to physics is very great in a very fundamental way. It is likely that the search for them will go on.

APPENDIX A

DETERMINATION OF THE RESPONSE FUNCTIONS

In chapter II we discussed the problem of signal loss due to inductive coupling of the detector loop to the surrounding superconducting shield. We use gradiometer detector loops to mitigate this problem but some degree of coupling remains causing a dispersion of the monopole signal over a range of possible values.

In the absence of coupling, the monopole would produce a signal corresponding to a flux change of $4\pi g$ in the detector loop. The effect of coupling is to reduce the apparent[91] flux change in the loop by an amount $|F'|$ where F' is the net flux impinging upon the gradiometer from vortex currents induced in the shield by the monopole, (see the discussion of chapter II). This flux will depend upon the monopole trajectory, (specifically the points P_1 and P_2 where the trajectory intersects the shield; see figure 5), the geometry of the shield, the plane $z = x_3^o$ of the gradiometer, and the pattern of cell polarities, $p(\rho, \phi)$ of the gradiometer. Thus:

$$F' = - \int_o^{2\pi} d\phi \int_o^R \rho d\rho \left\{ \left[\frac{\partial}{\partial z} V (P_1, P_2, B; \rho, \phi, z) \right]_{z = x_3^o} \cdot p(\rho, \phi) \right\} \qquad (A.1)$$

where R is the radius of the gradiometer, and B is the inside radius of the cylindrical shield. The corresponding signal will correspond to an apparent flux change in the gradiometer given by:

$$\tilde{F} = 4\pi g - |F'|$$

or, in units of the monopole flux, $4\pi g$;

$$F = \frac{\tilde{F}}{4\pi g} = 1 - \frac{|F'|}{4\pi g} \qquad (A.2)$$

Recall that for $p(\rho,\phi) \equiv 1$, (simple, single polarity loop) and for R = B, $|F'| = 4\pi g$ and consequently F is seen to be constrained to the interval from 0 to 1.

In order to determine the overall response of the detector we need to determine the distribution of probability versus signal size, P(F). This distribution will depend upon the nature of the monopole flux in the galaxy. In our experiments we have assumed a uniform and isotropic flux in accordance with the current predictions[47] that the mass of the monopole is extremely large. For a large number N_o of monopole events, we would count a number N(F) of these events which produce a signal corresponding to a flux change in the range [F,F+dF]. The probability distribution is then given as:

$$P(F) = \lim_{N_o \to \infty} \frac{N(F)}{N_o} \qquad (A.3)$$

For the detectors discussed in this work P(F) is calculated by simulating 3,000 to 5,000 monopole events with a computer. For each event the signal flux F is calculated and for the entire sample P(F) is determined as a histogram of the relative number of events, $N(F)/N_o$, in each of 100 bins over the range $F \in [0,1]$.

In this appendix I sketch the method in which P(F) was numerically determined. The main components of the computer program used for this calculation include; (i) the random generation of an event trajectory and determination of the positions of the vortex currents in the shields, (ii) the calculation of the normal component

of the magnetic field produced by these vortex currents at an arbitrary point (ρ,ϕ) in the plane of the gradiometer, (iii) numerical integration of equation (A.1) to obtain $|F'|$ and F, and finally (iv) determination of P(F). Furthermore, as a result of the complexity of equation (2.15), various streamlining methods were required in the calculation of F' to allow thousands of events to be included in the calculation without requiring impossible amounts of CPU time. All of these points will be discussed below.

Random Generation of Event Trajectories

In generating a trajectory, the point of intersection with the gradiometer is obtained first. To assure that these points are uniformly distributed over the surface of the gradiometers, the coordinates are obtained as follows:

$$\rho_o = R\sqrt{\text{RANDOM}}$$
$$\phi_o = 2\pi \cdot \text{RANDOM} \qquad \text{(A.4)}$$

where RANDOM is a freshly generated random number between 0 and 1, and R is the radius of the gradiometer.

The trajectory is now obtained by generating a velocity vector as follows:

$$v_1 = \sqrt{r_1}\cos 2\pi r_2$$
$$v_2 = \sqrt{r_1}\sin 2\pi r_2 \qquad \text{(A.5)}$$
$$v_3 = \sqrt{1 - r_1}$$

where r_1 and r_2 are different random numbers in the interval [0,1]. The points where the trajectory intersects the shield are then expressed in terms of a single parameter t:

$$x_i = x_i^o + v_i t \tag{A.6}$$

where $x_i^o = \rho_o \cos \phi_o$, $x_2^o = \rho_o \sin \phi_o$ and x_3^o is the z coordinate of the plane of the gradiometer. In terms of the geometric quantities shown in figure 49, the parameter t for trajectories through the top or bottom endcap is:

$$t_{end}^{\pm} = \mp (x_1^o v_1 + x_2^o v_2 \pm z_o v_3) \tag{A.7}$$

$$+ \sqrt{(x_1^0 v_1 + x_2^0 v_2 + z_0 v_3)^2 - [(x_1^0)^2 + (x_2^0)^2 + z_0^2 - R_0^2]}$$

where t_{end}^{+}, (t_{end}^{-}) corresponds to the case of intersection with the upper, (lower) endcap. If the trajectory intersects a side wall of the cylinder, $(\rho = B)$, then one uses:

$$t_{side}^{\pm} = \pm \left(\frac{x_1^0 v_1 + x_2^0 v_2}{v_1^2 + v_2^2} \right) + \sqrt{\left(\frac{x_1^0 v_1 + x_2^0 v_2}{v_1^2 + v_2^2} \right)^2 + \frac{B^2 - \rho_o^2}{v_1^2 + v_2^2}} \tag{A.8}$$

where t_{side}^{+} (t_{side}^{-}) corresponds to an intersection with the sidewall above (below) the gradiometer plane at x_3^0.

Numerical Evaluation of the Field Strength

The normal component of the field produced by the vortex currents at the gradiometer plane is derived from the scalar potential V of equation (2.15) as;

$$B_z (\rho, \phi, x_3^0) = -\frac{\partial V}{\partial z}\bigg|_{z = x_3^0} \tag{A.9}$$

In the numerical calculation, the two infinite sums in the explicit expression for B_z must be terminated at finite values of m and n. As a result of the differentiation of V with respect to z, the hyperbolic cosines in the numerator of the summand become hyperbolic sines and together with the hyperbolic sine in the denominator these factors lead to the convergence of the sum for most trajectories. To see this note that typically, (for i=1, 2); $|k_{mn}z_i| \gtrsim \xi_{mn}$ H/2B, and $k_{mn}(z_1 - z_2) \gtrsim \xi_{mn}$ H/B, where H is the vertical height of the shield at ρ = B. For the shield geometries used in our experiments H/2B ~ 0.2. As a result:

$$\frac{|\sinh k_{mn} z_i|}{\sinh k_{mn}(z_1 - z_2)} \simeq e^{-0.2\ \xi_{mn}} \qquad \text{for } \xi_{mn} >> 1$$

For this reason the maximum n value for each m was determined by the criterion that ξ_{mn} need not exceed 25.0 at which point the summand would have a numerical value a factor of at least e^5 smaller than the leading terms in the sum. In this way it is seen that the error in the field strength cannot exceed 1 part in 10^2. (Typically it did not exceed 1 part in 10^4 - this was seen by comparing the size of the final terms in the sum with the total sum for ~100 randomly distributed trajectories.)

Calculation of the Apparent Flux Change

For each trajectory the field was calculated at 1,018 points, uniformly distributed over the gradiometer. As seen in figure 33 the field strength varies extremely smoothly over the gradiometer plane

Figure 49. Graphic representation of geometric quantities used in the calculation of the position of the vortex currents.

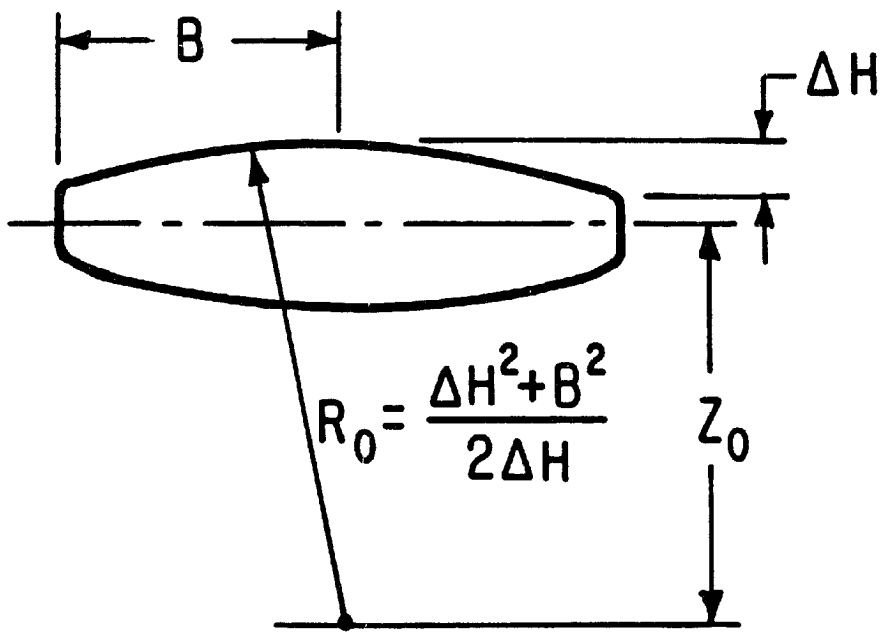

and consequently the 1,018 integration points should be sufficient to determine |F´| without introducing additional errors. By integrating the flux directly for a random sample of 100 events using;

$$f_{TOTAL} = \int_o^B \rho d\rho \int_o^{2\pi} d\phi \left[\frac{\partial \phi}{\partial z}\right]_{z = z_o}$$

it was found that the value f_{TOTAL} agreed with the expected value $4\pi g$ at the 99% level.

Streamlining of the Calculation Program

From equation (2.15) we see that for each of the 43 terms in the sum evaluated at each of the 1,018 points of integration in the flux determination we must have evaluated four Bessel functions; $J_m(k_{mn}\rho_1)$, $J_m(k_{mn}\rho_2)$, $J_m(\xi_{mn})$ and $J_m(\rho)$. Because the Bessel functions are themselves represented by infinite sums it is desirable to avoid calculating these ~175,000 Bessel functions from scratch for each one of the thousands of events in the sample. In fact, the CPU time required to calculate F for a single event when each Bessel function is evaluated from scratch is ~20 minutes on a Harris 100 computer, (a VAX 780 equivalent). For a sample of 5,000 events this implies a total CPU time of ~3 months.

Streamlining of the program is thus obtained by avoiding direct Bessel function evaluations in which the infinite sum expression is used. This is accomplished by calculating $J_{10}(x_n)$ and $J_9(x_n)$ at 1,000 points, ($x_n = 0.025$ for n = 1, ..., 1000), to a precision of 1 part in 10^6. Using stable downward iteration $J_8(x_n)$, ..., $J_0(x_n)$ are

determined from the recurrence relations for Bessel functions. The 11,000 values; $J_m(x_n)$ for m=0, ..., 10 and n=1, ..., 1,000 are stored in arrays. The value of $J_m(x)$ at an arbitrary point $x \epsilon [0,25]$ can now be determined by interpolation. If, out of the 1,000 discrete points, ($x_n = 0.025n$), x is nearest to a particular x_k then a second order Taylor expansion about x_k yields:

$$J_m(x) = J_m(x_k) + J_m'(x_k)\ (x-x_k) + \frac{1}{2} J_m''(x_k)\ (x-x_k)^2 + 0((x-x_k)^3) \quad (A.10)$$

Note that $x - x_k \leq 1/2\ (x_{k+1} - x_k) \sim 10^{-2}$ and so the second order expression has an error of roughly 1 part in 10^6. From the derivative relation:

$$J_m'(x) = \frac{1}{2} [J_{m-1}(x) - J_{m+1}(x)] \quad (A.11)$$

Equation (A.10) can be written as:[92]

$$J_m(x) \cong J_m(x_k) + \frac{1}{2} (x - x_k)\ (J_{m-1}(x_k) - J_{m+1}(x_k)) \quad (A.12)$$

$$+ \frac{1}{8} (x - x_k)^2\ (J_{m-2}(x_k) - 2J_m(x_k) + J_{m+2}(x_k))$$

Interpolated values of $J_m(x)$ at various, arbitrarily chosen values of $x \epsilon [0, 25]$ were compared with values obtained from direct evaluation of the infinite sum expression for $J_m(x)$. In all cases the error in the interpolated values was less than 1 part in 10^5.

By interpolating the Bessel functions, the field calculation time was reduced by an order of magnitude to roughly 1.5 minutes per event. The calculation of P(F) for the experiment discussed in chapters III and IV consisted of 3,000 simulated events and required ~5,000 CPU minutes. For the detector of chapter V there were 5,000

simulated events and the calculation required ~8,000 CPU minutes to complete. Histograms of P(F) from these calculations are shown in figures 10 and 36 respectively.

APPENDIX B

OPERATION OF RF-BIASED SQUIDS AND STRAIN GAUGE SIGNAL PROCESSING

RF-Biased SQUIDs

Superconducting Ring with a Single Weak Link[93]

A weak link is a region connecting two superconductors in which the critical current of momentum-paired electrons is lower than the critical currents of the superconductor which it joins. Weak links can be Josephson[94] tunnel junctions, (in which the link corresponds to a gap in the superconductor typically of thickness $\lesssim 10^{-7}$ cm formed as an oxide layer), or a point contact. The requisite properties of weak links that enable rf-SQUID operation are essentially the same for both types of junction. I will therefore only discuss in detail the point contact type of link for which the quantitative analysis of relevant properties is somewhat more simple.

Consider a ring superconductor with a single point contact weak link as first studied by Silver and Zimmerman.[95] The point contact may be considered to be a constriction in the ring of length t and having a circular cross section of area σ. The diameter of the constriction has thickness $2\sqrt{\sigma/\pi} \ll \Lambda$ where Λ is the London penetration depth[96] of the superconductor. The macroscopic Cooper pair wave function in the superconductor must be single-valued and so the integral of the phase around a closed contour C in the ring must be an integral multiple of 2π:

$$\frac{2\pi}{hc} \int_C \vec{p} \cdot d\vec{\ell} = 2\pi k, \qquad k \text{ an integer} \tag{B.1}$$

where $\vec{p}$ is the canonical momentum of each Cooper pair and h is Planck's constant. In a magnetic field described by a vector potential $\vec{A}$, the Cooper pair will have canonical momentum:

$$\vec{p} = 2m\vec{v} + 2e\vec{A} \tag{B.2}$$

where $\vec{v}$ is the velocity of the center of mass of the pair and m and e are the mass and charge, respectively, of the electron. Thus (B.1) is written:

$$\frac{m}{e} \int_C \vec{v} \cdot d\vec{\ell} + \int_C \vec{A} \cdot d\vec{\ell} = k\phi_o \tag{B.3}$$

where both sides of (B.1) have been multiplied by (hc/4πe) and where $\phi_o = hc/2e$ is the quantum of magnetic flux. The second term in (B.3) is simply the magnetic flux ϕ enclosed in the ring. To evaluate the first term we note that the expression for the current density is $\vec{j} = ne\vec{v}$ where n is the density of electrons participating in the current. Thus we may write:

$$\frac{m}{e} \int_C \vec{v} \cdot d\vec{\ell} = \frac{m}{ne^2} \int_C \vec{j} \cdot d\vec{\ell} \tag{B.4}$$

Everywhere along C except at the weak link we can choose our integration path to lie well below the surface of the superconductor where $\vec{j} = 0$ as predicted by London's equation. At the weak link however, the thickness of the constriction is smaller than the penetration depth so that a path cannot be found along which $\vec{j} = 0$. Following Silver and Zimmerman,[95] assume that σ is sufficiently small

that $\vec{j}$ is uniform throughout the cross-section of the link. Then $i = j\sigma$ = constant and we have:

$$\frac{m}{ne^2} \int_{link} \vec{j} \cdot d\vec{\ell} = \left[\frac{m}{ne^2} \left(\frac{t}{\sigma}\right) \frac{1}{L} \right] Li = \gamma Li \qquad (B.5)$$

where L is the ring inductance and $\gamma \equiv (m/ne^2)(t/\sigma L)$. Equation (B.3) can now be written:

$$\gamma Li + \phi = k\phi_o \qquad (B.6)$$

As for any superconducting ring, the flux ϕ in the ring is the sum of the external flux, ϕ_x, and the flux, Li, produced by the current in the ring:

$$\phi = Li + \phi_x \qquad (B.7)$$

Using (B.6) and (B.7) we can solve for the current in the ring and the flux in the ring in terms of the applied flux ϕ_x:

$$Li = (\phi_x - k\phi_o)/(1 + \gamma)$$

$$\phi = (k\phi_o + \gamma\phi_x)/(1 + \gamma) \qquad (B.8)$$

The weak link has a critical current i_c given by:[95]

$$i_c \sim \Delta/eR \qquad (B.9)$$

where Δ is the energy gap of the superconductor and R is the normal state resistance of the link, ($R = \rho t/\sigma$, where ρ is the normal state resistivity). From (B.8) we see that for a given k and for $|\phi_x - k\phi_o| < Li_c(1 + \gamma)$, the loop current will respond linearly to an applied flux ϕ_x. Over this range of ϕ_x, the internal flux ϕ will thus be constrained to the interval:

$$k\phi_o - \gamma Li_c \leq \phi \leq k\phi_o + \gamma Li_c \qquad (B.10)$$

The range of ϕ in (B.10) defines a "stationary magnetic state" centered on $\phi = k\phi_o$ which we will call the "k level" of internal flux. Typically γ is small compared to unity for cases of interest[97] and so for simplicity we will take $\gamma = 0$. Thus we see that the range over which Li is linear in ϕ_x for fixed k is given by $|\phi_x - k\phi_o| \leq Li_c$ and the corresponding stationary magnetic state over this range of ϕ_x is the state with $\phi = k\phi_o$ = constant.

The behavior of the superconducting ring with a single weak link is seen to fall into three categories: (a) $i_c < \phi_o/2La$, (b) $i_c = \phi_o/2La$ and (c) $i_c > \phi_o/2La$, where $a = 1 + \gamma \sim 1$ for the linear model of the point contact being considered here, and $a = \pi$ for a Josephson junction.[95] For the linear model we see from equations (B.8) with $\gamma = 0$ that if $i_c < \phi_o/2L$, the range in ϕ_x corresponding to the k level does not contain any values in common with the range of ϕ_x for any other level. If $i_c = \phi_o/2L$, successive levels have common endpoints, (the maximum value of ϕ_x in the k level corresponds to the minimum value of ϕ_x in the (k + 1) level for all k). For $i_c > \phi_o/2L$, the values of ϕ_x for successive levels overlap. Since the length of each k level is $2Li_c$, and each level is offset from each successive level by ϕ_o along the ϕ_x axis in a plot of ϕ versus ϕ_x, it follows that consecutive levels will overlap for a range of values $\Delta\phi_x = 2Li_c - \phi_o$. Thus we see that ϕ is not single-valued for this range. It is this phenomenon that is the basis of operation of rf-biased SQUIDs. Henceforth it will be understood that we are considering only those rings with a single weak link for which $i_c > \phi_o/2L$.

Transitions Between Stationary
Magnetic States and Hysteresis

If in the k level we gradually increase the external flux ϕ_x, the superconducting ring will respond with an induced current i such that Li produces a flux equal and opposite to the external flux ϕ_x. This is merely a restatement of the fact that a superconducting ring obeys Lenz's law exactly. When $\phi_x = k\phi_o + Li_c$ however, the current in the weak link will have reached the critical value i_c. The current cannot, therefore, continue to increase in response to increasing ϕ_x and the screening of the external flux becomes imperfect. As a result, external flux leaks into the ring while at the same time the current in the ring diminishes. Over a time $\tau = L/R$, (where L is the inductance of the ring and R is the normal state resistance of the link) a quantum of flux, ϕ_o, is leaked into the ring and a transition to the k + 1 level takes place.[98] During the transition the current in the loop decreases in magnitude by an amount corresponding to the change in flux in the loop; i.e. $\Delta i(k \rightarrow k + 1) = \phi_o/L$.

The transition takes place at constant $\phi_x = Li_c + k\phi_o$. If we now proceed to decrease the external flux, the downward transition $k + 1 \rightarrow k$ will take place at a value $\phi_x = (k + 1)\,\phi_o - Li_c$. Thus we see that by alternately increasing and decreasing the external flux, the system will execute a hysteresis loop in ϕ versus ϕ_x. The change in energy associated with the traversal of the loop is the change in Gibb's free energy, (i.e. the magnetic energy of the current flowing in inductance L) which is just the area of the hysteresis loop divided by L:

$$\Delta G = [k\phi_o + Li_c - ((k + 1)\ \phi_o - Li_c)]\ \phi_o/L = 2i_c\phi_o - \phi_o^2/L \qquad (B.11)$$

The Effects of a Time-Varying External Flux

To understand the operation of the rf-biased SQUID we now consider the effects of a time-varying external flux, $\phi_x(t)$, on the superconducting ring with single weak link. The effects that we will consider were first studied quantitatively by Silver and Zimmerman[95] but the approach that we will take in understanding these effects follows closely to that presented by Giffard, Webb, and Wheatley[99] whose rf-biased SQUID design is essentially that used by the BTI Corporation in the manufacture of the SQUIDs used in our experiments.

We will now consider what happens when the external flux varies sinusoidally in time at radio frequencies.[100] The flux is provided by an rf coil coupled to the SQUID.[101] The rf coil in turn is part of an LCR resonance circuit driven by an rf voltage source, (denoted V_d), operated at the resonant frequency, (ω_o) of the circuit. A dc voltage is also applied to the rf coil to produce a dc level in the external flux about which the sinusoidal variation takes place. The external flux at the SQUID loop produced by the rf tank circuit is thus of the form:

$$\phi_x(t) = \phi_{dc} + \phi_{rf}^o \exp(t/2\tau) \sin \omega_o t \qquad (B.12)$$

where $\tau = L_T/R_T = Q/\omega_o$, (the subscript T is in reference to the rf LCR tank circuit components and Q is the quality factor of the resonance). Thus at $t = 0$, $\phi_x = \phi_{dc}$ and as t increases the external flux at the SQUID oscillates about ϕ_{dc} with exponentially increasing amplitude as

energy gets accumulated in the tank circuit. Suppose that initially the SQUID is in the k quantum level with external flux $k\phi_o$. After some time t_o the amplitude of the external flux will be great enough that $\phi_x(t_o)$ will correspond to an endpoint of the k level and a transition will take place. If $Li_c \lesssim 10\phi_o$ the transition will take place to an adjacent state,[102] $k \pm 1$. If the coupling coefficient between the rf coil L_T and the SQUID loop L_o is κ and the mutual inductance is M then the current in the rf coil will be reduced at the transition by $\kappa^2 \Delta i_o = \kappa^2 \phi_o / M$. In other words the lowering of the Gibb's free energy of the SQUID also corresponds to a lowering of the free energy of the rf coil. The lost energy is dissipated either thermally, radiatively, or both.[103]

If initially $\phi_{dc} = k\phi_o + \phi_o/2$, an upward transition to the $k + 1$ level will occur at time t_1 where $\phi_{rf}^o \exp(t_1/2\tau)$ just exceeds $Li_c - \phi_o/2$. When the energy lost in the transition is just repleted by the rf voltage source, a downward transition back to the k level will occur at an external flux $\phi_x = (k + 1/2)\phi_o - Li_c$. Hysteresis thus takes place continually and an energy $|\Delta G|$ is lost in each hysteresis cycle where ΔG is given by (B.11). The amplitude of the external flux variation, $\phi_{rf}^o \exp(t_1/2\tau)$, cannot be exceeded until the energy supplied by the rf-drive per rf cycle just exceeds the energy lost per hysteresis cycle. When this occurs, the amplitude of the external flux variation will again increase linearly with increasing rf drive amplitude. A plot of the amplitude of the voltage across the rf coil versus the amplitude of the rf drive voltage will thus rise linearly then remain constant over a range of drive voltage amplitude

beginning with the onset of hysteresis and ending at the point where the energy provided by the drive per rf cycle compensates the energy lost per hysteresis cycle. This "step" is then followed by a second "riser"; (in which the coil voltage amplitude again increases linearly with increasing drive amplitude). At even higher drive amplitudes, multiple-loop hysteresis takes place. We thus see that there exists a whole series of steps and risers. Let V_A be the amplitude of the rf coil voltage on the first step.

When we start in the k level with $\phi_{dc} = k\phi_o$, the first transition will take place at amplitude $\phi_{rf}^{o} \exp(t_2/2\tau) = k\phi_o \pm Li_c$. Since the downward transition to the k - 1 state is equidistant from ϕ_{dc} as the upward transition to the k + 1 level, either transition could occur first. Let us assume that the upward transition takes place. In the k + 1 level $\phi_{dc} = k\phi_o$ is much closer to the leftmost edge of that level than to the rightmost edge so that an immediate downward transition back to the k level will occur. Note that in this case, the amplitude of the rf-drive must be larger than before since the oscillation of external flux must have an amplitude of Li_c rather than $Li_c - \phi_o/2$ at the onset of hysteresis. Let V_B denote the amplitude of the rf coil voltage of the new step obtained for $\phi_{dc} = k\phi_o$.

For all other values of ϕ_{dc} on the k level, (for any integer k) it can be shown that the amplitude of rf coil voltage, V_{STEP}, on the corresponding step will lie between V_B and V_A. Furthermore, as ϕ_{dc} is continually increased, V_{STEP} will sweep out a triangle pattern of peak to peak amplitude[104] $V_\Delta = V_B - V_A$ with period ϕ_o.

The Detection of the Mean Level of Flux in the SQUID

In order to detect magnetic field changes in a detection coil, (in our case a gradiometer), a "signal" coil is coupled to the SQUID.[105] The signal coil can be attached to the detection coil so that a change of flux in the latter will induce a current in the former leading to a net flux change at the SQUID.[106]

To detect a change in mean level of flux, $\bar{\phi}$, in the SQUID a small sinusoidal modulation flux at an angular frequency ω_m and peak-to-peak amplitude $\alpha\phi_o$ is applied to the SQUID by means of a small af current in the rf coil. (The parameter α is called the "modulation index" and is set equal to 1/2 for normal operation.)

As we saw in the last section, the triangle pattern of peak voltage across the rf coil as a function of the mean flux in the SQUID has slope $2V_\Delta/\phi_o$ and period ϕ_o. Application of a sinusoidal modulation of frequency ω_m thus results in an envelope of modulation on the rf voltage across the rf coil. The af modulated flux at the SQUID with peak-to-peak amplitude $\alpha\phi_o$ is adjusted to be centered on an integral or half-integral value of ϕ_o.[107] The envelope of modulation of the rf coil voltage thus has the form:

$$V(t) = (2V_\Delta/\phi_o)[(\alpha\phi_o/2)\sin(\omega_m t)], \qquad 2n\pi < \omega_m t < (2n+1)\pi$$

$$V(t) = -(2V_\Delta/\phi_o)[(\alpha\phi_o/2)\sin(\omega_m t)], \qquad (2n+1)\pi < \omega_m t < (2n+2)\pi$$

If now the signal coil adds an additional flux, $s\phi_o$, to the mean level of flux applied to the SQUID, the center of the modulation will be shifted by $s\phi_o$ and the envelope of the modulated voltage becomes:

$$V(t) = (2V_\Delta/\phi_o)[(\alpha\phi_o/2)\sin(\omega_m t) + s\phi_o], \qquad 2n\pi - \eta < \omega_m < (2n+1)\pi + \eta$$

(B.13)

$$V(t) = -(2V_{\Delta}/\phi_o)[(\alpha\phi_o/2)\sin(\omega_m t) + s\phi_o],\ (2n+1)\pi + \eta < \omega_m t < (2n+2)\pi - \eta$$

where $\eta = \sin^{-1}(2s\phi_o/\alpha)$.

The rf coil voltage V(t) is detected, (it is passed through an integrator which eliminates the rf component of the variation of the voltage but which does not attenuate the af component) and amplified. The signal from the amplifier is then fed to a lock-in amplifier which puts out a dc signal proportional to a_1, the first fundamental of the wave form V(t). Since V(t) is symmetric about $\omega_m t = (2n + 1/2)\pi$, the Fourier components will be of the form $a_\ell \sin(\ell\ \omega_m t)$. The first fundamental, a_1, is thus:

$$a_1 = \frac{\omega_m}{\pi} \int_o^{2\pi/\omega_m} V(t) \sin(\omega_m t)\, dt \qquad (B.14)$$

Substituting (B.13) for V(t) into (B.14) and performing the integration we find:

$$a_1 = (2V_{\Delta}/\pi\phi_o)[(\alpha\phi_o/2)(\sin(2\eta) - 2\eta) + 4s\phi_o \cos\eta] \qquad (B.15)$$

We are interested in the response of the system to small changes in the mean flux at the SQUID. Hence we consider (B.15) in the limit where s is very small. In this case we find:

$$a_1 = s(8V_{\Delta}/\pi) \equiv s\Gamma \qquad (B.16)$$

Thus the system, (SQUID, rf amplifier, detector, and lock-in amplifier) may be characterized by a forward flux-voltage transfer characteristic $G_{\phi v}$ connecting the output voltage with the mean input flux change, $s\phi_o$, by the equation:

$$e_o = G_{\phi v}\ s\phi_o \qquad (B.17)$$

where e_o is the output of the lock-in amplifier.

In order to increase the dynamic range of the system (i.e. the range over which the system responds linearly to changes of input flux, $s\phi_o$), a negative feedback flux ϕ_F proportional to e_o is applied to the SQUID via the rf coil. To accomplish this, the output of the lock-in amplifier is fed back to the rf coil through a series resistance, R_F, which determines the feedback current.

The feedback loop is thus characterized by a voltage to flux transfer characteristic, $g_{v\phi}$, given by:

$$g_{v\phi} = M/R_F \tag{B.18}$$

where M is the mutual inductance coupling of the rf coil to the SQUID. The feedback flux is thus $\phi_F = g_{v\phi}e_o$ and R_F is adjusted so that $\phi_F + s\phi_o = 0$. The maximum feedback flux is determined by the maximum output voltage, $(e_o)_{max}$, and $g_{v\phi}$ to be:

$$(\phi_o)_{max} = (M/R_F)(e_o)_{max} \tag{B.19}$$

In practice, a dynamic range of more than $\pm 500\phi_o$ is typically achieved.

In the above discussion we have seen that changes in magnetic field in a detection loop connected to a signal coil which, in turn couples to the SQUID, can be measured by monitoring the output voltage of the lock-in amplifier. To determine the smallest flux change in the signal coil which can be detected it is necessary to know the noise voltage of the system associated with the output voltage e_o. A careful analysis by Giffard et al.[99] shows that the noise in the device consists of two uncorrelated components - "equivalent flux

noise" and "intrinsic flux noise." The former corresponds to noise in the amplifiers and other components comprising the detection electronics. The latter is due to flux noise in the SQUID, (caused by thermal fluctuations which result in slight variations in the level of external flux, ϕ_x, at which the transition between different magnetic states take place), and also flux variations at the SQUID corresponding to current or flux noise in the detection coil. In the absence of the detection coil, (signal coil shorted at the SQUID), the equivalent and intrinsic flux noise are roughly equal and together generate a total flux noise of about 10^{-4} $\phi_o/\sqrt{Hz}$. In our systems, the gradiometer circuits have a flux noise which is typically between 4×10^{-4} $\phi_o/\sqrt{Hz}$ and 3×10^{-3} $\phi_o/\sqrt{Hz}$, and is therefore the dominant source of noise.

Strain Gauge Signal Processing

The strain gauges used to monitor vibration in the experiment of chapter V are piezoelectric devices.[81] Distortion of the gauges, as caused by vibration, will therefore produce small voltages, (typically ~0.1 - 10.0 mV or so). In order to detect sudden sharp impulses above a continuous background of vibration, (noise), the signal from each strain gauge is processed by the electronic circuit shown in figure 50. The signal is first passed through a differential amplifier. The amplifier is differential so that common mode signals - which might be induced in the twisted pair signal leads, (connecting the strain gauges to the amplifier) via capacitive coupling to the shielding for the leads - are rejected. The gain of this first stage

amplifier is ~ 500. In the second stage, the signal is half-wave rectified and integrated with a time constant of ~0.2 seconds. The purpose of the integration is to convert any continuous ac noise in the signal to a roughly constant dc level. Sudden impulses above the noise background will then result in a sudden and transient shift in the dc output of the integrator. This is found to greatly enhance the signal-to-noise ratio. The series capacitor and series resistor between the first and second amplification stages eliminates undesirable dc offsets in the output of the differential amplifier. Finally, the output of the integrator is buffered.

The output of the buffer can be read out directly and is also fed to three summing circuits, (not shown in the figure) where different strain gauge signals can be added. Switches in the leads connecting the output of the buffer stage to the summing circuits enable us to choose different combinations of added signals. The signals are summed in this manner to allow us to monitor all eight of the strain gauges inside the detector on the chart recorder without using all eight of the chart recorder channels. In our standard mode of operation, signals from six strain gauges were summed and read out on one chart recorder channel as in figure 45. The summing circuits include an additional factor of 20 in amplification.

Figure 50. Strain gauge signal processing circuit.

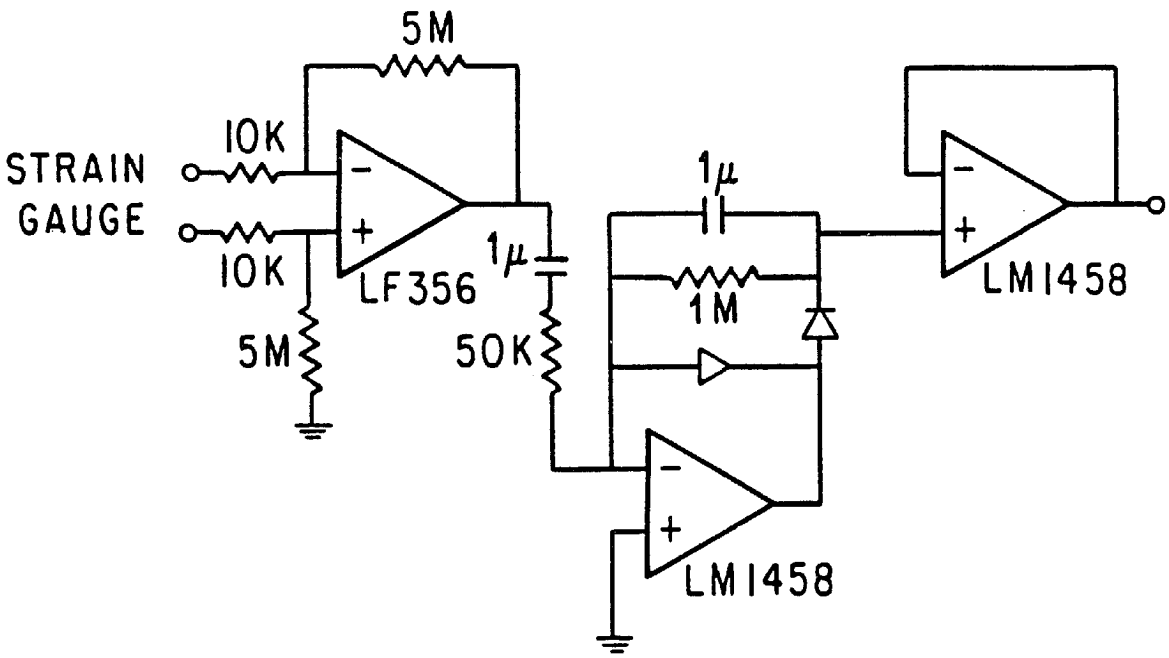

APPENDIX C

MUTUALLY ORTHOGONAL GRADIOMETERS

In this appendix the concept of mutually orthogonal gradiometers is formally developed and related to the symmetries inherent in the shape of the planar region to be occupied by the overlapped grids. A systematic method of classifying mutually orthogonal gradiometers according to their behavior under symmetry transformations is then developed. In this way mutually orthogonal patterns, can be found without detailed calculations. It is shown that for planar regions with n-fold symmetry a maximum number, $N = 2(\ell + 1)$ mutually orthogonal patterns can be found in this manner, where ℓ is the multiplicity of the factor 2 in a prime factorization of n. For regions with continuous symmetries it is shown that the number of patterns that can be systematically classified from symmetry considerations is infinite.

Orthogonality and Symmetry

To any gradiometer lying in the xy-plane we can associate a characteristic function, p(x,y), which we will call the "polarity function." The polarity function defines the relative polarities of the cells in the grid and thus takes on the values +1 and -1 except at the position of the current filament and outside the gradiometer where it will be defined to be zero. The polarity function is related to the normal component of magnetic field in the plane, $B_z(x,y)$, that is produced by a current in the grid:

$$p(x,y) = \frac{\pm B_z(x,y)}{|B_z(x,y)|} \tag{C.1}$$

One fixes the sign of B_z in (C.1) as positive or negative depending upon the convention that is chosen for the definition of positive polarity.

We will restrict our attention to 'balanced' gradiometers, (i.e. those which have equal areas of opposite polarity cells), so that the following condition is satisfied:

$$\iint_{\Lambda} dxdy\ p(x,y) = 0 \tag{C.2}$$

where Λ is the area occupied by the gradiometer in the plane.

Now consider two gradiometers, labelled 1 and 2, which have the same shape and size and which have been overlapped to occupy the same region Λ in the plane. If a current is circulated in grid 1 to produce a field with normal component $B_{1z}(x,y)$ in the plane, then a current will be induced in grid 2 in proportion to the net magnetic flux impinging upon it. The net flux is given by the integral of the normal component of the field weighted by the polarity function for grid 2:

$$\Delta\Phi = \iint_{\Lambda} dxdy\ B_{1z}(x,y)\ p_2(x,y) \tag{C.3}$$

Suppose now that the region Λ is symmetric with respect to a non-trivial unitary coordinate transformation A; i.e. for A: $(x,y) \rightarrow (x',y')$, $\Lambda \rightarrow \Lambda' = \Lambda$. The transformation A is a symmetry transformation of Λ. It follows from the balance condition (C.2) that we can construct patterns for grids 1 and 2 that are even and odd, respectively, under the operation A:

Figure 51. Effect of a 180° rotation on two rectangular gradiometer patterns. (a) Two rectangular gradiometers. (b) The same rectangular gradiometers after a 180° clockwise rotation of the coordinates. The pattern on the left is even, (+), under this transformation while the one on the right is odd, (-). Black and white regions have opposite polarity.

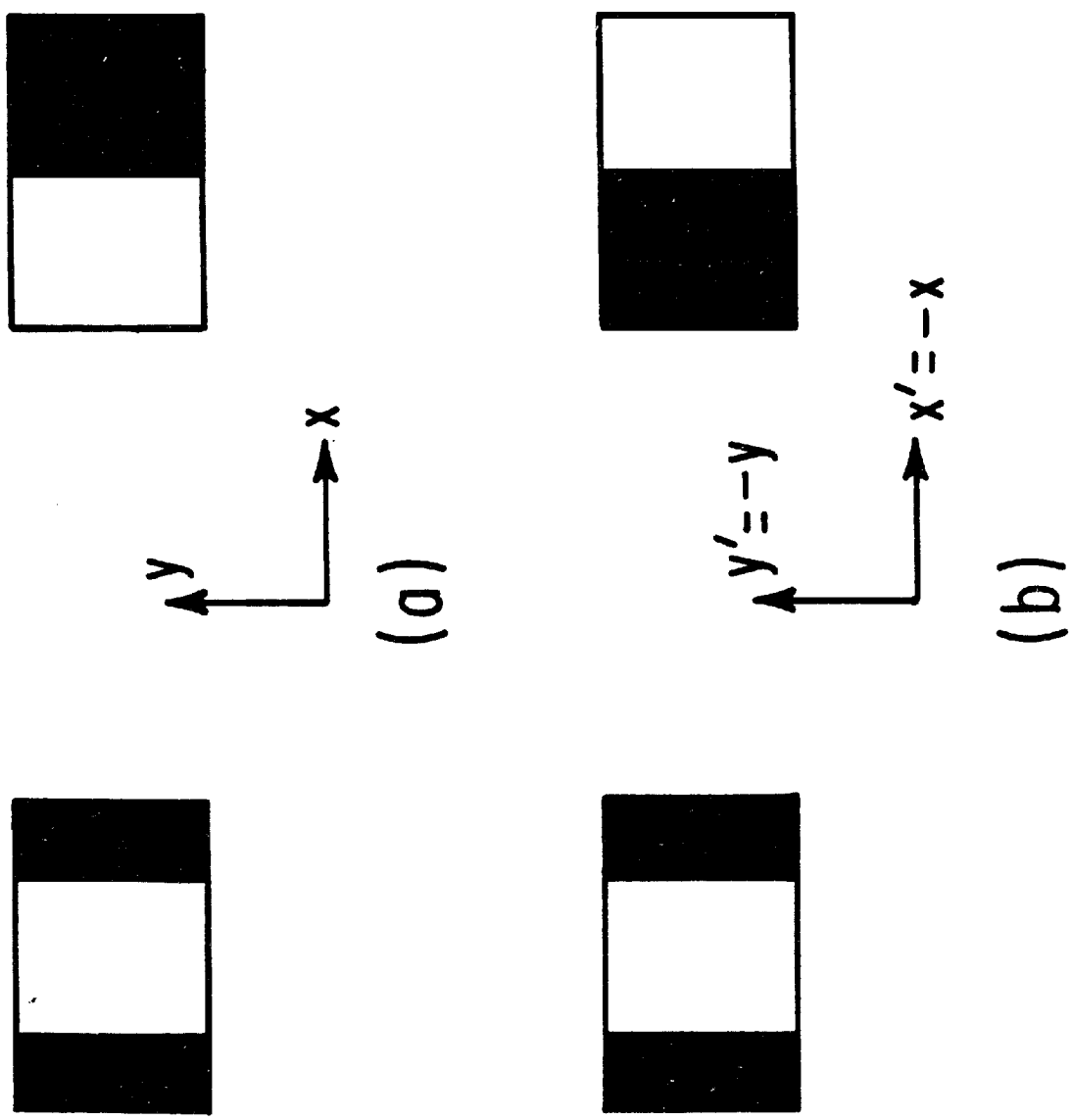

$$p_1(x',y') = p_1(x,y)$$
$$p_2(x',y') = -p_2(x,y) \qquad (C.4)$$

Both gradiometers will have current-carrying filaments in the same places in the new coordinate system as they did in the original coordinate system. The only observable difference will be that grid 2 will have all of its cell polarities flipped. (This is demonstrated in figure 51 for the case of two rectangular gradiometers under the operation of a 180° counterclockwise rotation of coordinates.) We see therefore that the magnetic field produced by a current in grid 1 will also be even under A:

$$B_{1z}(x',y') = B_{1z}(x,y) \qquad (C.5)$$

Using $dx'dy' = dxdy$ for a unitary transformation, we can write the net flux impinging upon grid 2 in the new coordinate system as:

$$\Delta\Phi' = \iint_{\Lambda'} dx'dy'\ B_{1z}(x',y')\ p_2(x',y')$$
$$= \iint_{\Lambda} dxdy\ B_{1z}(x,y)\ (-p_2(x,y)) = -\Delta\Phi$$

We know however that the net flux is independent of the coordinate system in which we measure it and so $\Delta\Phi' = \Delta\Phi$ from which we may conclude that $\Delta\Phi = 0$. Thus for every non-trivial one-to-one unitary transformation A mapping Λ onto itself there exists a pair of orthogonal gradiometer patterns.

To obtain more than two mutually orthogonal gradiometers it is necessary to find patterns which have even and odd character with respect to two or more symmetry transformations of the region Λ. If

for instance A and B are two such distinct transformations then it may be possible to construct a set of four mutually orthogonal gradiometers corresponding to the four possibilities: (A,B) = (+,+), (+,-), (-,+) and (-,-), where the shorthand notation of a plus (minus) sign is used to represent even (odd) character under the respective transformations indicated in the ordered pair to the left of the equal sign. To determine all of the orthogonal patterns that can be placed in region Λ we must find all of the possible even and odd transformation combinations for the complete set of symmetry transformations of Λ.

Gradiometers with n-Fold Symmetric Shapes

As an example of practical interest consider regions Λ_n which have n-fold symmetry, (where $n \geq 2$) by which it is meant that Λ_n has n distinct reflection symmetries and an n-fold rotation axis. An example of such a shape is an n-sided equilateral polygon. The set of all symmetry transformations of a physical system is a group and the symmetry transformations of Λ_n form the group[108] C_{nv} of order 2n. Not counting the identity element there are 2n-1 non-trivial transformations in C_{nv}. Naively one might therefore be tempted to conclude that there are 2^{2n-1} distinct combinations of even and odd symmetry character. However it must be remembered that C_{nv} is closed under the group product. This means for instance, that if the symmetry character of a pattern in Λ_n is fixed for two transformations A and B as even and odd respectively then for a third transformation C = AB it is necessarily odd. To find the set of allowed distinct patterns in Λ_n that still have specific even or odd symmetry for all

TABLE 13

THE CLASSIFICATION OF FOUR PATTERNS WITH EVEN/ODD, (+/-), CHARACTER FOR ALL TRANSFORMATIONS IN C_{4v}

Transformation	Pattern			
	1	2	3	4
C_4) Generators	+	+	-	-
$M_4(1)$)	+	-	+	-
$C_4^2 = C_4 \cdot C_4$	+	+	+	+
$C_4^3 = C_4 \cdot C_4 \cdot C_4$	+	+	-	-
$M_4(2) = C_4 \cdot M_4(1)$	+	-	-	+
$M_4(3) = M_4(1) \cdot C_4 \cdot C_4$	+	-	+	-
$M_4(4) = M_4(1) \cdot C_4$	+	-	-	+
$E = M_4(1) \cdot M_4(1)$	+	+	+	+

$A \in C_{nv}$ we must find the smallest set of elements whose integral powers and products of integral powers produce all of the elements of the group. Thus we seek a minimal set of generators of the group C_{nv}. Group theory tells us that for every $n \geq 2$ the group C_{nv} can be generated by a rotation through an angle $2\pi/n$, denoted C_n, together with any one of the n reflections $m_n(i)$; $i = 1, \ldots, n$. Thus once we have fixed the even-odd character of a pattern under C_n and a reflection $m_n(i)$, the even-odd character of the pattern under every transformation in C_{nv} will have been determined.

For every $n \geq 2$ there are two patterns that can be obtained which correspond to even and odd character under the generator $m_n(i)$. If n is odd these are the only possible patterns. (This follows from the fact that if n is odd, the generator C_n must be even since if it were odd then C_n to the odd power n must also be odd. This is not possible since $C_n^n = E$, the identity transformation, for which all patterns are even.) If on the other hand n is even, then $n = 2k$ for some integer k and it is not inconsistent to construct a pattern which is odd under C_n. In this case the two possible even-odd character possibilities for both C_n and $m_n(i)$ combine to allow $2 \cdot 2 = 4$ possible mutually orthogonal patterns. The four possibilities for C_{4v} are listed in table 13. Figure 52 shows the axes about which the reflections $m_4(i)$ are performed.

We have not yet exhausted all of the possible orthogonal patterns of Λ_n since we have not considered patterns which have symmetry character for some but not all of the transformations in C_{nv}. Although such patterns break some of the inherent symmetries of C_{nv}

Figure 52. Reflection axes for 4-fold symmetry. An example of an object with 4-fold symmetry is a square.

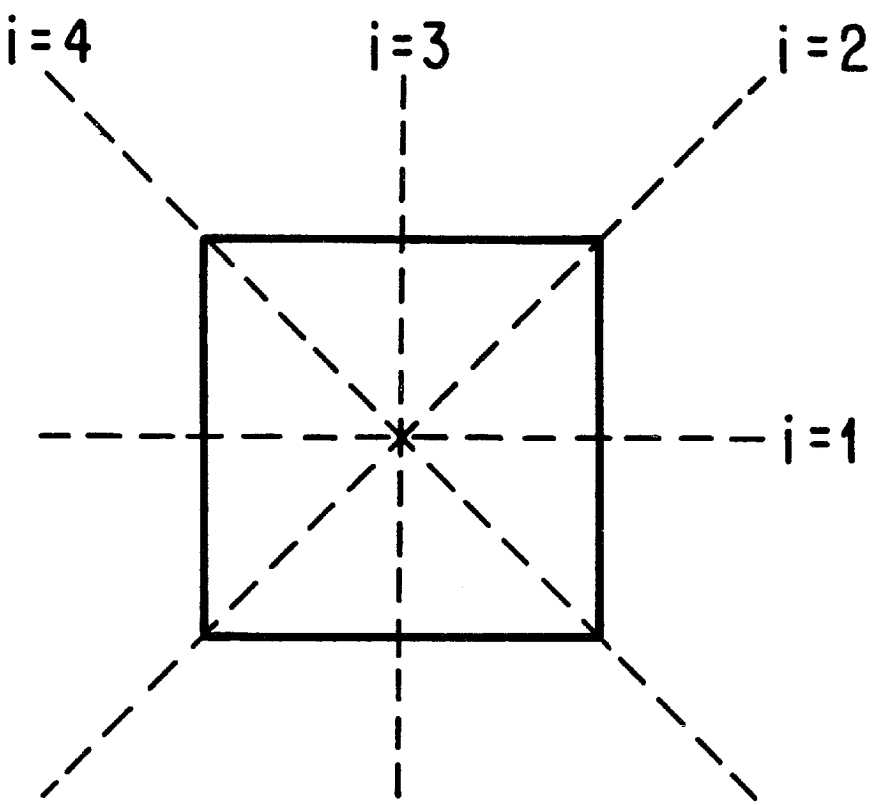

the remaining unbroken symmetries will still correspond to a group of symmetry transformations. For this reason we now consider the subgroups of C_{nv}.

The subgroups of C_{nv} are of three types. Namely, those which contain only rotations, those which contain only reflections and those which contain both rotations and reflections. For each $n \geq 2$, C_{nv} has a distinct subgroup of rotations corresponding to each distinct integer factor k of n. These are generated by C_n^k and have order h given by $h = n/k$. These are all of the rotation subgroups of C_{nv}.[109] (In C_{12v} for instance there are 6 rotation subgroups generated by C_{12}, C_{12}^2, C_{12}^3, C_{12}^4, C_{12}^6 and $C_{12}^{12} = E \equiv$ identity, of order 12, 6, 4, 3, 2 and 1 respectively.) The remaining subgroups of C_{nv} can be found by combining rotations, (which includes $E = C_n^n$) and reflections.

To this end we first note that C_n^k for $k \leq n$ corresponds, in the passive viewpoint, to a counterclockwise rotation of the coordinates by an angle $2\pi k/n$. Thus C_n^k rotates the line of reflection labelled i to the position of the line labelled j in the original coordinate system where $j=(i + k)$ modulo(n). This is demonstrated schematically in figure 53. Any subgroup which contains C_n^k and $m_n(i)$ must therefore contain $m_n(j)$. It is then clear that to each rotation subgroup generated by C_n^k there are k corresponding subgroups of order $2h = 2n/k$ which contain both rotations and reflections. In C_{12v} for $k = 3$ we thus find three subgroups of order 8; i.e.

$$(E, C_{12}^3, C_{12}^6, C_{12}^9, M_{12}(1), M_{12}(4), M_{12}(7), M_{12}(10))$$
$$(E, C_{12}^3, C_{12}^6, C_{12}^9, M_{12}(2), M_{12}(5), M_{12}(8), M_{12}(11))$$

$$(E,\ C_{12}^{\ 3},\ C_{12}^{\ 6},\ C_{12}^{\ 9},\ M_{12}(3),\ M_{12}(6),\ M_{12}(9),\ M_{12}(12)).$$

When k = 1 we obtain the entire group C_{nv} and when k = n we get the n reflection subgroups of order 2: i.e. $(E,\ m_n(i))$, i = 1, ..., n. Together with the rotation subgroups, these comprise all of the subgroups of C_{nv}. If n has ℓ distinct integer factors k_i, we see that the total number of subgroups of C_{nv} is:

$$M = \sum_{i=1}^{\ell} (k_i + 1).$$

(In C_{4v}, for example, there are $\ell = 3$ distinct factors; $k_1 = 1$, $k_2 = 2$, and $k_3 = 4$. The number of subgroups of C_{4v} is thus M = 10. These are listed in table 14.)

Since two patterns must have opposite symmetry character with respect to a common transformation in order to be orthogonal, we know that patterns with rotational symmetries alone cannot be orthogonal to patterns having only reflection symmetries. Similarly patterns having only the symmetries of the group generated by $C_n^{\ k}$ will not be orthogonal to all of the patterns having the symmetries of the group generated by $(C_n^{\ k},\ m_n(i))$. This is because each of the former with even, (or odd), character under $C_n^{\ k}$ will correspond to two of the latter with the same character under $C_n^{\ k}$ - i.e. one which is even under $m_n(i)$ and the other of which is odd under $m_n(i)$. With very similar reasoning the patterns with only a single reflection symmetry will be nonorthogonal to at least one pattern obtained from every subgroup generated by a rotation $C_n^{\ k} \neq E$ and a reflection. We conclude therefore that none of the patterns with reflection or

Figure 53. Rotation of relection axes. Under a clockwise rotation of coordinates through an angle of $2\pi k/n$, the ith reflection axis is rotated counterclockwise to the position of the jth axis. Thus if the symmetry group of a pattern contains c_n^k and $m_n(i)$, it must also contain $m_n(j)$.

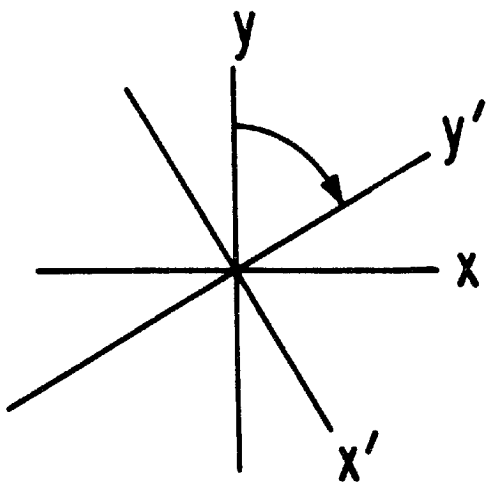

(a)

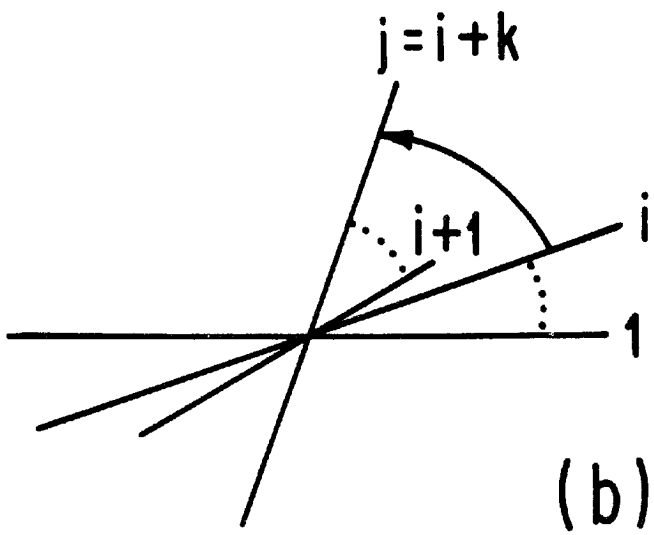

(b)

TABLE 14

SUBGROUPS OF C_{4v}, THEIR GENERATORS, AND THE NUMBER OF PATTERNS ASSOCIATED WITH EACH

Subgroup	A Generating Set	Number of Patterns
$S_1 = (C_4, C_4^2, C_4^3, E)$	(C_4)	2
$S_2 = (C_4^2, E)$	(C_4^2)	2
$S_3 = (E)$	(E)	-
$S_4 = C_{4v}$	$(C_4, M_4(1)$	4
$S_5 = (C_4^2, E, M_4(1), M_4(3))$	$(C_4^2, M_4(1))$	4
$S_6 = (C_4^2, E, M_4(2), M_4(4))$	$(C_4^2, M_4(2))$	4
$S_7 = (E, M_4(1))$	$(M_4(1))$	2
$S_8 = (E, M_4(2))$	$(M_4(2))$	2
$S_9 = (E, M_4(3))$	$(M_4(3))$	2
$S_{10} = (E, M_4(4))$	$(M_4(4))$	2

rotation symmetries alone can be orthogonal to all of the patterns with both types of symmetry. Since the latter are at least as numerous as the former it suffices to restrict our attention to their case only in our pursuit of the largest set of mutually orthogonal gradiometers.

Among the patterns with both reflection and rotation symmetries, several further restrictions can be found. First of all, patterns generated by the same rotation, C_n^k, but having different reflection symmetries cannot all be mutually orthogonal since they only have rotations in common. Consequently of the k subgroups generated by $(C_n^k, m_n(i))$; i = 1, ..., k, we need only consider one. To further eliminate subgroups we must now consider separately the cases where n is odd or even.

As in the case of the entire group, if n is an odd integer it cannot have any factors k_i which are even and patterns cannot be odd under the operation of the generator C_n^k. Thus each subgroup generated by $(C_n^k, m_n(i))$ for every factor k will have two possible patterns for which all of the rotations are even and the reflections are even and odd respectively. Obviously these patterns will not be orthogonal to all of the patterns of any other subgroup or of the full group. We conclude therefore that subgroups do not contribute additional patterns so that, for n an odd integer, there are at most two mutually orthogonal patterns that can be obtained.

If n is even then there can be patterns which are odd under C_n, (as discussed above), so that there are 4 patterns with all of the symmetries of the group C_{nv}. In all four cases C_n^{2k} is an even

transformation for all positive integers k. Consequently if h = n/2 is an even integer, two patterns can be obtained from the subgroup generated by $(C_n^2, m_n(1))$ which are odd under C_n^2, (i.e. $(C_n^2, m_n(1))$ = (-,-) or (-,+)) and therefore mutually orthogonal to the 4 patterns obtained above for C_{nv}. Moreover, each pattern must be even under C_n^4. In general it is easy to see that the argument can be repeated to show that if $n/2^{\ell}$ is even then there are two patterns with odd character under C_n^{2j} corresponding to the subgroups generated by $(C_n^{2j}, M_n(i))$ for each j = 1, ..., ℓ. All of these patterns will be mutually orthogonal with each other and also with the four patterns obtained when C_n is an even or odd transformation.

We have exhausted our consideration of the patterns that can be obtained with some or all of the symmetries of Λ_n. The total number N of possible mutually orthogonal patterns that can be found in this way is seen to be:

$$N = 2(\ell + 1) \tag{C.5}$$

where ℓ is a positive integer given by the condition:

$$n = 2^{\ell} \cdot m \tag{C.6}$$

and m is some positive odd integer. As a specific example the 6 orthogonal character combinations for n = 4 are listed in table 15. Graphic representations of patterns with these symmetry characteristics are shown in figure 54 where Λ_4 is chosen to be a square. The general classification scheme for $n = 2^{\ell} \cdot m$ is given in table 16.

TABLE 15

EVEN/ODD, (+/-), CLASSIFICATION OF 6 MUTUALLY ORTHOGONAL PATTERNS IN C_{4v} UNDER TRANSFORMATIONS* IN C_{4v}

Transformation	Pattern 1	2	3	4	5	6
E	+	+	+	+	+	+
C_4	+	+	-	-		
C_4^2	+	+	+	+	-	-
C_4^3	+	+	-	-		
$M_4(1)$	+	-	+	-	+	-
$M_4(2)$	+	-	-	+		
$M_4(3)$	+	-	+	-	-	+
$M_4(4)$	+	-	-	+		

*Blanks in the table indicate that a pattern has no symmetry under that transformation.

Figure 54. Six mutually orthogonal patterns with symmetries of the group C_{4v}. A set of 6 mutually orthogonal gradiometers with square boundaries is shown. Under at least one of the symmetry transformations of a square, (an element of C_{4v}), each of the patterns (a) - (f) will be either even, (+), or odd, (-), with respect to cell polarities. Furthermore, for any two of the patterns there is at least one transformation in C_{4v} for which one pattern will be even while the other will be odd so that gradiometers with these patterns can be expected to have no mutual inductance.

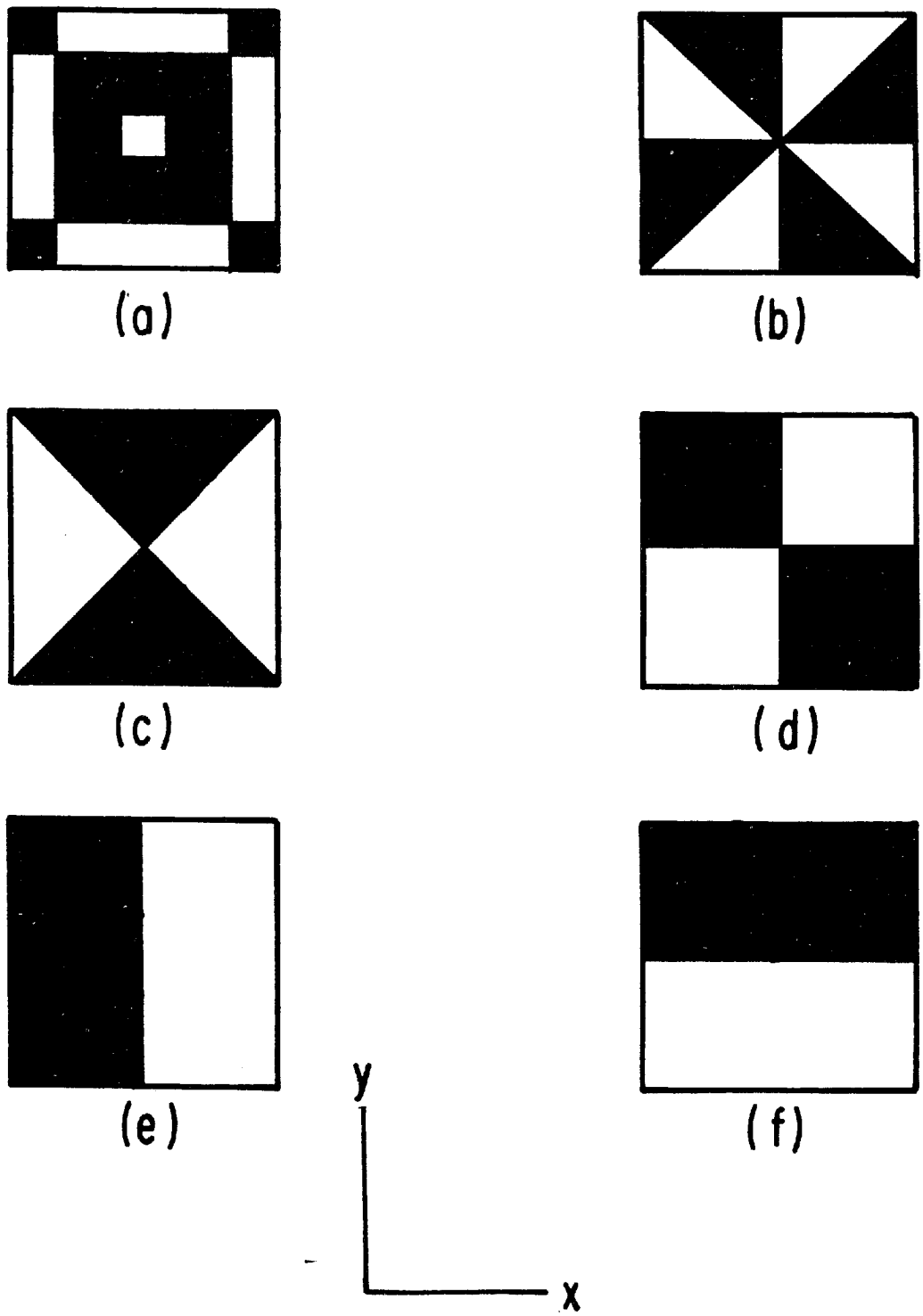

TABLE 16

CLASSIFICATION SCHEME FOR MUTUALLY ORTHOGONAL GRADIOMETERS WITH n-FOLD SYMMETRIC SHAPES

Multiplicity of factor 2	Symmetry Character of the Subgroup Generators*	Total Number of Mutually Orthogonal Patterns
0	$(C_n, m_n) = (+,+), (+,-)$	2
1	All of the Above Plus $(C_n, m_n) = (-,+), (-,-)$	4
2	All of the Above Plus $(C_n^2, m_n) = (-,+), (-,-)$	6
3	All of the Above Plus $(C_n^4, m_n) = (-,+), (-,-)$	8
4	All of the Above Plus $(C_n^8, m_n) = (-,+), (-,-)$	10
.	.	.
.	.	.
.	.	.
ℓ	All of the Above Plus $(C_n^{\alpha}, m_n) = (-,+), (-,-)$	$2(\ell + 1)$

Where $\alpha = 2^{\ell-1}$

*Since any one of the reflections $m_n(i)$, (for i = 1, ..., n), may be used, the reflection in the generator set is given the generic symbol m_n.

Regions with Continuous Symmetries

When $\Lambda_n \to \infty$ the region will have translational symmetry, i.e. $A: \Lambda_n \to \Lambda_n$ where $A\vec{x} = \vec{x}' = \vec{x} + \vec{a}$ and $\vec{a}$ is any constant vector in R^2. Since this is a continuous symmetry it follows that the symmetry group of Λ_n is infinite. I will now show that there exists an infinite number of mutually orthogonal gradiometers of infinite extent.

Consider the gradiometer whose pattern function is given by:

$$p(x,y) = \frac{\sin \frac{\pi x}{a} f(y)}{\left|\sin \frac{\pi x}{a} f(y)\right|} \qquad (C.7)$$

where $f(y)$ is some arbitrary smooth function of y. Clearly $p(x,y)$ is odd for a reflection about $x = (2n + 1)\, a/2$ for any integer n. It follows that this pattern will be orthogonal to any pattern which is even about any axis $x = na$ or which is odd about $x = (2n + 1)\, a/2$. This can be seen to represent an infinite set of mutually orthogonal grids. As an example consider the set of patterns:

$$\left\{ p_n(x,y) = \frac{\sin \frac{2^n \pi x}{a} f(y)}{\left|\sin \frac{2^n \pi x}{a} f(y)\right|}, \text{ for } n = 0, 1, 2, \ldots \right\}$$

Choose two distinct members of this set arbitrarily; $p_m(x,y)$ and $p_n(x,y)$. Suppose, without loss of generality, that $m > n$ so that $m = n + q$ for some integer q. Then for x in a given interval

$$\left(\frac{ka}{2^n}, \frac{(k+1)a}{2^n} \right)$$

with $k > 0$ an integer, the pattern $p_n(x,y)$ has the same polarity for fixed y, while the polarity of $p_n(x,y)$ will change 2^q times. Furthermore $p_m(x,y)$ will be odd for reflection about $\tilde{x} = (k+1/2)a/2^n$ while $p_n(x,y)$ will be even about $\tilde{x}$. Thus the two patterns must be orthogonal. Since they were chosen arbitrarily it follows that all of the patterns in the set must be mutually orthogonal. In general, any region which has a continuous symmetry will have a corresponding infinite set of mutually orthogonal patterns even if the region is finite.

A circular region for instance is symmetric for any rotation about an axis through its center. An infinite set of mutually orthogonal patterns for such a region is then given by:

$$\left\{ p_n(r,\theta) = \frac{\sin \frac{2^n\theta}{\pi} \cdot f(r)}{\left|\sin \frac{2^n\theta}{\pi} \cdot f(r)\right|}, \; n = 0, 1, \ldots \right\}$$

Since a circle can be approximated by an equilateral polygon of n sides in the limit as n becomes infinite we could have predicted that there are an infinite number of mutually orthogonal patterns for such a region from our previous result for regions with n-fold symmetry.

REFERENCES

1. P.A.M. Dirac, Proc. Roy. Soc. London, Ser. A 133, 60 (1931).

2. There is no a priori reason for the nodal line to have these properties. Dirac goes on to show however that these properties do in fact lead to a mathematically consistent formalism. See reference 1.

3. From a modern perspective, it is natural to ask why the electron charge appears in the quantization condition. Why not consider the down quark charge instead so that the minimal Dirac charge is increased by a factor 3?

   Since quarks are confined it makes sense to consider them only over distances less than a fermi. It is true that the d quark transported about the Dirac monopole picks up a phase. The quark however also carries color and so the monopole string will be undetectable if the monopole also carries a color magnetic charge such that the phase picked up by the quark due to its color interaction with the monopole compensates the phase from the electromagnetic interaction. We then see that a monopole with Dirac magnetic charge is allowed if it also has a color magnetic charge of the right value. The color magnetic field of the monopole cannot be detected on the macroscopic level since it will be screened for distances greater than 1 fm as a result of nonperturbative color effects. See reference 14.

4. T.T. Wu and C.N. Yang, Phys. Rev. D12, 3845 (1975).

5. T.T. Wu and C.N. Yang, Nucl. Phys. B107, 365 (1976). For any such choice there will be two poles. A mapping of the surface of the sphere onto a plane will then result in one pole mapping to all points at infinity.

6. Ig. Tamm, Z. Phys. 71, 141 (1931).

7. See, for example: E. Amaldi in, Old and New Problems in Elementary Particles, G. Puppi, ed.,(Academic Press, New York, 1968) 1.

8. As a result, laboratory magnetic fields could be used to collect monopoles impinging upon a larger surface area than the area of the detection devices. See, for example; W.V.R. Malkus, Phys. Rev. 83, 899 (1951).

9. Processing of materials to search for trapped monopoles is discussed in the article of reference 7. Also see; L.W. Alvarez et al., Rev. of Sci. Instr. 42, 326 (1970), for the description of an induction type material processing instrument.

10. See, for example; E.M. Purcell et al., Phys. Rev. 129, 2326 (1963) or H. Bradne and W.M. Isbel, Phys. Rev. 114 603 (1958).

11. The discussion of this section is based upon the review articles of references 14 and 17.

12. See, for example, I.J.R. Aitchison and A.J.G. Hey, Gauge Theories in Particle Physics, (Adam Hilger Ltd., Bristol, 1982) 291, and section 8.5.

13. Thus monopoles are not required in the electroweak spontaneously broken gauge field theory developed by Glashow, Weinberg and Salam.

14. J. Preskill, Ann. Rev. Part. Sci. 34, 461 (1984).

15. G. 't Hooft, Nucl. Phys. B79, 276 (1974).

16. A.M. Polyakov, Zh ETF Pis. Red. 20, No. 6, 430 (1974).

17. The discussion of the appearance of monopoles in G = SO(3) presented here closely follows that given by P. Goddard and D.I. Olive in Rep. Prog. Phys. 41, 1357 (1978). The SO(3) example is the easiest to visualize because the order parameter of the spontaneous symmetry breaking, which is the isovector Higgs field, can be thought of as spontaneously choosing a direction in internal symmetry space.

18. H. Georgi and S.L. Glashow Phys. Rev. D6, 2977 (1972).

19. Since the subgroups $H_{\vec{\phi}}$ of rotations about the $\vec{\phi}$ axis for fixed $\vec{\phi} \in A_o$ are all isomorphic they are all denoted generically by the same symbol H.

20. P.W. Higgs, Phys. Rev. Lett. 12, 132 (1964), and Phys. Rev. Lett. 13, 508 (1964).

21. The Higgs mechanism by which the massless gauge particles become massive is analogous to the situation in superconductivity whereby the coherent motion of Cooper pair electrons acts to screen out external magnetic fields. To see this, consider the covariant Maxwell equation $\partial^\mu \partial_\mu A^\nu = j^\nu$, (where the Lorentz gauge $\partial^\mu A_\mu = 0$ has been assumed). The covariant generalization of the current of a charged scalar field is $j^\mu = iq[\phi^*(\partial^\mu \phi) - (\partial^\mu \phi^*)\phi] - 2q^2 A^\mu |\phi|^2$. This is the Klein-Gordon current made gauge invariant by the replacement $\partial^\mu \to D^\mu = \partial^\mu + iqA^\mu$. In superconductivity ϕ is the order parameter or "macroscopic wave function" describing the coherent Cooper pairs. In particle physics it is the Higgs field. If we choose a gauge in which the non-zero vacuum value, $\phi = f/\sqrt{2}$, is a real constant then the current is $j^\nu = -q^2 f^2 A^\nu \equiv -M^2 A^\nu$. In superconductivity, this is called the "screening current" since from Maxwell's equations, $\vec{\nabla} \times \vec{B} = \vec{j}$ so that if $\vec{j} = -M^2 \vec{A}$, where $M > 0$ is constant, then taking the curl we get $\nabla^2 \vec{B} = M^2 \vec{B}$ and so $\vec{B} \sim e^{-Mx}$. Thus M^{-1} is

the penetration depth of the magnetic field. In particle physics $\Box A^{\nu} = j^{\nu} = -M^2 A^{\nu}$ is the wave equation for a free vector particle of mass M.

22. If more fields are added T_a may have half integer values in which case the eigenvalues Q are integer multiples of 1/2 q $\hbar$.

23. "You can't comb the hair on a billiard ball without leaving a part," J. Preskill, reference 14.

24. The quantity q is a coupling constant and not an electric charge. It has inverse charge dimensions and is related to the electric charge e_1 by $q = e_1/\hbar c$, thus $e_1 g = \hbar c$, consistent with the Dirac condition (1.3). Note however that e_1 is not the smallest charge which may enter since the isotopic generators may have half integer eigenvalues, (reference 22), in which case the smallest charge is $e = 1/2\ e_1$ and so $eg/\hbar c = 1/2$ and $g = g_D$, the smallest Dirac charge.

25. Confer the article of reference 17, 1375.

26. With larger groups you can find an SU(2) subgroup which when broken yields the monopole solution in the same manner discussed above for SO(3). This SU(2) subgroup need not be broken to U(1). The U(1) factor necessary for electromagnetism is obtained from the breaking of the entire group and will involve generators from other subgroups of G as well as the SU(2) subgroup which when broken yields the monopole solution.

27. The ensuing discussion of the microscopic properties of monopoles is taken from, J. Preskill in Inner Space Outer Space; E. Kolb, M.S. Turner, D. Lindley, K. Olive and D. Seckel, eds. (The University of Chicago Press, Chicago, 1986).

28. Above the critical temperature T_c, the potential $V(\vec{\phi})$ is understood to be of the form $V \sim |\vec{\phi}|^2$ so that there exists a single minimum at $\vec{\phi} = 0$. Below T_c, V takes the form of equation (1.8). Consequently the phase transition corresponds to a shift from the old to the new minima of V - each of which are appropriate vacua in the two different temperature ranges about T_c.

29. J. Preskill, Phys. Rev. Lett. 43, 1365 (1979).

30. A.H. Guth and S.H. Tye, Phys. Rev. Lett. 44, 631 (1980).

31. A.H. Guth, Phys. Rev. D23, 347 (1981).

32. E.N. Parker, Astrophys. J. 160, 383 (1970), and also; M.S. Turner, E.N. Parker, and T. Bodgan, Phys. Rev. D26, 1296 (1982).

33. This is roughly the Planck mass which is the mass expected for monopoles in Kaluza-Klein type unification theories.

34. The X boson core of the monopole mediates baryon number nonconservation processes in some theories. See for instance; C.G. Callan in Monopole '83, J. Stone ed. (Plenum, New York, 1984) 169.

35. E.W. Kolb, S.A. Colgate, and J.A. Harvey, Phys. Rev. Lett. 49, 1373 (1982); S. Dimapoulos, J. Preskill, and F. Wilczek, Phys. Lett. 119B, 320 (1982); K. Freese, M.S. Turner, and D.N. Schramm, Phys. Rev. Lett. 51, 1625 (1983).

36. See for example, P. Musset, M. Price and E. Lohrmann, Phys. Lett. 128B, 333 (1983); B. Aubert, P. Musset, M. Price, and J.P. Vialle, Phys. Lett. 120B, 465 (1983).

37. See for example, P.H. Eberhard, R.N. Ross, L.W. Alvarez, and R.D. Watt, Phys. Rev. D4, 3260 (1983).

38. A monopole with a mass of 10^{16} GeV/c^2 passing 10 meters through a 100 kGauss magnetic field at a velocity of 10^{-3} c will be deflected 1 fermi.

39. A very complete description of ionization techniques and experiments is given by T.M. Liss, S. Ahlen, and G. Tarlé, Phys. Rev. D30, 884 (1984).

40. T. Watanabe and T. Ebisu in Monopole '83, J. Stone ed. (Plenum, New York, 1983) 501.

41. B. Price, S.L. Guo, S.P. Ahlen, and R.L. Fleischer, Phys. Rev. Lett. 52, 1265 (1984).

42. See S.M. Errede in Monopole '83, J. Stone ed., (Plenum, New York, 1983) 271.

43. M.J. Shepko and R.C. Webb, proceedings of the DPF meeting at Santa Fe, NM, Oct., 1984.

44. E.N. Alexeyev, M.M. Boliev, A.E. Chudakov, and S.P. Mikheyev, Proc. 19th Int. Cosmic Ray Conf. (LaJolla) 8, 250 (1985).

45. S.P. Ahlen and K. Kinoshita, Phys. Rev. D26, 2347 (1982).

46. D.M. Ritson, SLAC-PUB-2950, 1982 (unpublished).

47. M. Turner in Proc. of the First Aspen Winter Physics Conference, M. Bloch ed., and K. Freese, M.S. Turner and D.N. Schramm, Phys. Rev. lett. 51, 1625 (1983).

48. An indirect calibration using 24 keV neutrons to produce slow recoil protons in plastic scintillator has been done by one group. The energy loss of slow monopoles is expected to differ from that of slow protons by a constant factor only. See, S.P. Ahlen, T.M. Liss, C. Lane, and G. Liu, Phys. Rev. Lett. 55, 181 (1985).

49. M. Faraday, Faraday's Diary, Vol. I, Oct. 17, 1831. T. Martin ed., (G. Bell and Sons, Ltd., 1932).

50. L.W. Alvarez, LBL Physics Note 470, Sept. 3, 1963 (unpublished).

51. L.J. Tassie, Nuovo Cimento 38, 1935 (1965).

52. P.H. Eberhard, R.N. Ross, L.W. Alvarez, and R.D. Watt, Phys. Rev. D4, 3260 (1971).

53. L.W. Alvarez, Proposal to NASA to Search for Magnetic Monopoles in Returned Samples of Moon Surface Material, Jan. 30, 1966.

54. H. Kolm et al., Phys. Rev. D4, 1285 (1971).

55. L.L. Vant-Hull, Phys. Rev. 173, 1412 (1968).

56. These results are stated in an apparently nonsensical way since it is not consistent with quantum mechanics to have magnetic charges smaller than a single Dirac charge. The results should be interpreted to mean that no magnetic charges were observed in samples of 2.5×10^{23} electrons etc. Furthermore, as first pointed out by D. Groom, if all electrons have the same magnetic charge, the effects of this charge in this experiment can be transformed away by a simple unitarity rotation. See reference 66 regarding such a transformation for electric-magnetic charge mixture.

57. B. Cabrera, Phys. Rev. Lett. 48, 1378 (1982).

58. B. Cabrera, M. Taku, R. Gardner, and J. Bourg, Phys. Rev. Lett. 51, 1933 (1983).

59. B. Cabrera, Ph.D. thesis, Stanford University, 1974 (unpublished); B. Cabrera and F. van Kahn, Acta Astronautica 5, 127 (1978).

60. The free energy of a flux line in a superconductor is proportional to its length in the superconductor. See reference 59.

61. Model 30 SQUID; BTI Corporation, 4174 Sorrento Valley Boulevard, San Diego, CA 92121. The operation of rf-SQUIDs is discussed briefly in Appendix B.

62. H. Frisch as discussed by C.C. Tseui in Magnetic Monopoles, R.A. Carrigan Jr. and W.P. Trower eds. (Plenum, New York, 1983) 209.

63. C.D. Tesche et al., Appl. Phys. Lett. 43, 384 (1983).

64. J.G. Park, C.N. Guy; "Inductive Monopole Detectors of Coil-Shield Area Ratio Approximately 1: The Signal Size Distribution," Blackett Lab, UK-preprint (1982); C.N. Guy in Monopole '83, J. Stone ed. (Plenum, New York, 1983) 491.

65. Andre-Marie Ampere, Theorie des Phenomenes Electro-dynamiques, (Mavignon-Marvis, Paris, 1826) 14 and figure 1.

66. See J.D. Jackson, Classical Electrodynamics, (Wiley and Sons, New York, 1975) 42.

67. C.C. Chi et al., Monopole '83, J. Stone ed. (Plenum, New York, 1984) 459.

68. B. Cabrera et al., Monopole '83, J. Stone ed. (Plenum, New York, 1984) 446.

69. Helander Spinning Co., 4108 West Division Street, Chicago, IL 60651.

70. S. Somalwar, H. Frisch, J. Incandela, and M. Kuchnir, Nucl. Instr. and Meth. in Phys., Res., 226, 341 (1984).

71. Stabl-Levl mount SLM-1; Barry Wright Corp., 700 Pleasant St., Watertown, MA 02172.

72. Our first experience with spurious signals came with the Fermilab prototype as discussed in Chapter II. For a study of signals induced by environmental disturbances see; F.R. Fickett, M. Cromar, and A.F. Clark in Monopole '83, J. Stone ed., (Plenum, New York, 1983) 477.

73. Model 8306; Bruel and Kjaer Instruments, 185 Forest St., Marlborough, MA 01752.

74. Model GS-1 DEM; Billings McEachem Inc., Forest City, CA.

75. For simplicity, a conservative 20 seconds was added for timing uncertainty in all channels.

76. This result was published in 1984. See, J. Incandela, M. Campbell, H. Frisch, S. Somalwar, M. Kuchnir, and H.R. Gustafson, Phys. Rev. Lett. 53, 2067 (1984).

77. The contents of this chapter are contained in a recent paper. See J. Incandela et al., "First Results from a 1.1 m Diameter Superconducting Monopole Detector" EFI preprint 85-75. (To be published in Phys. Rev. D).

78. Ostalloy 158, (melts at 158°F), Arconium Corp., 400 Harris Avenue, Providence, RI 02909.

79. Apiezon N; Apiezon Products Ltd., 4 York Road, London S.E. 1, England.

80. Stabl Levl mount SLM-3; Barry Wright Corp., 700 Pleasant Street, Watertown, MA 02172.

81. Model SG-2M; Gulton Industries Inc., 212 Durham Avenue, Methuchen, NJ 08840. We thank M. Cromar for making us aware of these devices.

82. In the absence of a passing monopole there is, of course, no net flux change since the superconducting loop obeys Lenz's law exactly. One gradiometer thus induces a current in response to the $6\phi_o$, or $60\phi_o$ pseudopole flux. In the other gradiometer, the net pseudopole flux is zero and no current is induced.

83. An upper limit for the self-inductance is obtained by summing calculated inductances of the circular loops in the pattern. We therefore anticipated a signal $\gtrsim$ 3.0 mV.

84. For offsets that are smaller than about one-half of the a.c. peak-to-peak noise it is difficult to determine the signal rise time in a visual scan of the chart recorder data for which the SQUIDs were filtered at 1.0 Hz. For this reason fast and slow d.c. offsets cannot be easily distinguished. The exclusion of offsets below the levels mentioned does not alter our determination of spurious monopole signal rates discussed later.

85. We calculate a rate at 90% C.L. using the Poisson distribution:to obtain this rate we divide 3.6 by the exposure time where the number 3.6 is obtained from the Poisson

distribution for n = 1. This yields a larger estimate of the rate of offsets for this circuit than would be obtained by using the inverse of the exposure time alone.

86. A.D. Caplin, M. Hardiman, M. Koratzinos, and J.C. Schouten, Nature 321, 402 (1986).

87. S. Bermon, P. Chaudhari, C.C. Chi, C.D. Tesche, and C.C. Tsuei, Phys. Rev. Lett. 55, 1950 (1985).

88. M.W. Cromar, A.F. Clark, and F.R. Fickett; Phys. Rev. Lett. 56, 2561 (1986).

89. With both detector units operating, the coincident area averaged over solid angle is 0.75 m^2. This would represent an increase in detection area of 3.6, 4.4, 6.4, 7.5 and 15, respectively, compared to the experiments listed.

90. Of course the detector units in the experiment of Chapter V have a larger area (~4 times) and other features which are different from our previous detector so that the reduction in spurious signal rate cannot be guaranteed to occur upon cooling in lower ambient fields.

91. The flux change in the loop is always $4\pi g$ for the passage of a monopole. The current may not however correspond to a flux change of $4\pi g$ as a result of counter-currents induced by the field trapped in the shield. The apparent flux change corresponds to the flux change in the loop that would yield the net observed current.

92. For m = 0 or 1 slightly different formulae are necessary.

93. The discussion of a superconducting ring with a single weak link presented in this section is based largely upon reference 95.

94. B.D. Josephson, Phys. Lett. 1, 251 (1962); and Rev. Mod. Phys. 36, 216 (1964).

95. A.H. Silver and J.E. Zimmerman, Phys. Rev. 157, 317 (1967). The content of this article is presented in its entirety and in perhaps more pedagogical form by L. Solymar in; Superconductive Tunnelling and Applications, (Wiley, New York, 1972) 217.

96. For a clear presentation of superconductor phenomenology as well as the BCS microscope theory of superconductivity, see; A.C. Rose-Innes and E.H. Rhoderick, Introduction to Superconductivity, 2nd edition, (Pergamon, Oxford, 1978).

97. From (B.9) with $R = \rho t/\sigma$, it follows that $\gamma \sim (m/ne^2)(\Delta/e\rho)(1/Li_c)$. Typically rf-SQUIDs use junctions for which $Li_c \sim 10\phi_o$. A typical value of γ for this critical current is $\sim 10^{-16}$.

98. During the transition, the flux in the ring is not quantized although the link is not necessarily in the normal state. The quantization of flux, after all, is the result of the single-valuedness condition on the Cooper pair wave function in a superconducting ring for which a closed contour can be found along which the current density is zero. For a weak link the current density is nowhere zero in its cross-section and so the line integral of the current density will contribute to the change in phase of the wave function. Consequently the phase contributed by the line integral of the vector potential need not be an integer multiple of 2π so long as the line integral of the current density across the junction contributes a change in phase such that the total phase change is an integer multiple of 2π. For $i \ll i_c$ the current density contribution is small so that the flux in the ring is very nearly quantized. for $i = i_c$, (at a transition) the current density contribution to the phase can be large and the flux need not be close to a quantum value.

99. R.P. Giffard, R.A. Webb, and J.C. Wheatley, Journal of Low Temp. Phys. 6, 533 (1972).

100. The superconducting ring with single weak link used in references 95 and 99 is a two-hole type which is topologically closed by superconducting material in order to shield out magnetic field and radiation to reduce noise. As a result, rf fields are used to couple to the SQUID. See, for instance, J. Clarke, IEEE 61, 8 (1973) and references 95 and 99 above.

101. The superconducting ring with single weak link is referred to as the SQUID (Superconducting Quantum Interference Device).

102. For larger critical currents, transitions to the $k \pm 2$ states are favored. See reference 95.

103. During the transition a voltage difference, V, develops across the junction due to the leakage of flux into the ring. The energies of the Cooper pair condensed states on either side of the junction are thus shifted in energy by 2eV relative to one another. Cooper pairs travel from the higher to the lower energy level and are accompanied by the emission of two photons (each of energy $h\nu = eV$) in order to balance the decrease in energy. The voltage difference also induces a current of quasi-particles. These particles behave like normal electrons and so their current is resistive causing some energy to be thermalized.

104. The amplitude V_Δ can be calculated very simply (see reference 99, 543) to be: $V_\Delta = 1/2\ (L\omega_o\phi_o/M)$. The sensitivity of the SQUID as a magnetometer increases with V_Δ, (discussed in a later section) so that a small coupling constant κ between the rf coil and the SQUID is desirable. There is however a lower limit on κ below which V_Δ will decrease. We saw that for $\phi_{dc} = k\phi_o$, the

"step" occurs at $V_B > V_A$. Since the linear rise to the step at V_B has the same finite slope as that to the step at V_A it follows that the step at V_B begins at a higher drive voltage. Triangle patterns with peak-to-peak amplitude V_Δ will only occur over the range of drive voltages where the steps overlap. This is equivalent to the statement that the width of the step at V_A must be larger than the width, in drive voltage, of the riser between the two steps. This leads to the condition that $\kappa^2 Q > \pi/2$ where Q is the quality factor of the tank circuit.

105. In practice the signal coil goes in one hole of the symmetric two-hole SQUID and the rf coil goes in the other. Unlike the rf coil which is weakly coupled to the SQUID, the signal coil is coupled as strongly as possible.

106. The coupling is most efficient when the inductance of the detection loop matches the signal loop inductance; see: J.E. Zimmerman, Sensitivity Enhancement of Superconducting Quantum Interference Devices Through the Use of Fractional Turn Loops, (preprint).

107. When the oscillation is centered on an integral or half-integral number of flux quanta the peak to peak amplitude of the coil voltage with modulating flux is a minimum. Adjusting the system to center the oscillation on one of the flux levels is thus achieved by seeking a minimum amplitude.

108. This notation follows that of A.W. Joshi in, Elements of Group Theory for Physicists, 3rd edition, (Wiley Eastern, New Delhi, 1983).

109. This follows directly from the fact that every subgroup of a cyclic group is also cyclic and also from the fact that the order of every subgroup H of a group G divides the order of G.